

AD_____

Award Number: W81XWH-09-1-0413

TITLE: High Resolution PET Imaging Probe for the Detection, Molecular Characterization and Treatment Monitoring of Prostate Cancer

PRINCIPAL INVESTIGATOR: Neal H. Clinthorne, M.S.

CONTRACTING ORGANIZATION: Regents of the University of Michigan
Ann Arbor, MI 48109-1274

REPORT DATE: July 2012

TYPE OF REPORT: Final

PREPARED FOR: U.S. Army Medical Research and Materiel Command
Fort Detrick, Maryland 21702-5012

DISTRIBUTION STATEMENT: Approved for Public Release;
Distribution Unlimited

The views, opinions and/or findings contained in this report are those of the author(s) and should not be construed as an official Department of the Army position, policy or decision unless so designated by other documentation.

REPORT DOCUMENTATION PAGEForm Approved
OMB No. 0704-0188

Public reporting burden for this collection of information is estimated to average 1 hour per response, including the time for reviewing instructions, searching existing data sources, gathering and maintaining the data needed, and completing and reviewing this collection of information. Send comments regarding this burden estimate or any other aspect of this collection of information, including suggestions for reducing this burden to Department of Defense, Washington Headquarters Services, Directorate for Information Operations and Reports (0704-0188), 1215 Jefferson Davis Highway, Suite 1204, Arlington, VA 22202-4302. Respondents should be aware that notwithstanding any other provision of law, no person shall be subject to any penalty for failing to comply with a collection of information if it does not display a currently valid OMB control number. **PLEASE DO NOT RETURN YOUR FORM TO THE ABOVE ADDRESS.**

1. REPORT DATE (DD-MM-YYYY) July 2012		2. REPORT TYPE Final		3. DATES COVERED (From - To) 1 July 2009 - 30 June 2012	
4. TITLE AND SUBTITLE High-Resolution PET Imaging Probe for the Detection, Molecular Characterization and Treatment of Prostate Cancer				5a. CONTRACT NUMBER .	
				5b. GRANT NUMBER W81XWH-09-1-0413	
				5c. PROGRAM ELEMENT NUMBER	
6. AUTHOR(S) Neal H. Clinthorne, M.S. & Stan Majewski, Ph.D. nclintho@umich.edu				5d. PROJECT NUMBER	
				5e. TASK NUMBER	
				5f. WORK UNIT NUMBER	
7. PERFORMING ORGANIZATION NAME(S) AND ADDRESS(ES) Regents of the University of Michigan 3003 S. State St. Ann Arbor, M 48109-1274				8. PERFORMING ORGANIZATION REPORT NUMBER	
9. SPONSORING / MONITORING AGENCY NAME(S) AND ADDRESS(ES) U.S. Army Medical Research and Material Command Fort Detrick, Maryland 21702-5012				10. SPONSOR/MONITOR'S ACRONYM(S)	
				11. SPONSOR/MONITOR'S REPORT NUMBER(S)	
12. DISTRIBUTION / AVAILABILITY STATEMENT APPROVED FOR PUBLIC RELEASE; DISTRIBUTION UNLIMITED					
13. SUPPLEMENTARY NOTES					
14. ABSTRACT The goal of this work was to improve PET instrumentation used for molecular imaging in prostate cancer with applications to diagnosis, guiding biopsy, planning treatment and monitoring therapy. The goal was achieved by developing the concept of dedicated endorectal PET probes that provide significant improvements in image quality over conventional, external-ring PET alone. Using newly available silicon photomultiplier technology, several "probe" detectors were developed. It was predicted, and subsequently shown, that probes having good position resolution in 3D would be important. Through the use of simulation and phantom imaging studies, these devices demonstrated the potential for obtaining high spatial resolution for prostate imaging. Practical proof-of-concept detectors with good depth-of-interactions resolution have been developed and tested. The most desirable next step will be to integrate these probes with commercial PET/MRI systems for human subjects testing.					
15. SUBJECT TERMS Molecular Imaging, Positron Emission Tomography (PET), Prostate Cancer					
16. SECURITY CLASSIFICATION OF:			17. LIMITATION OF ABSTRACT UU	18. NUMBER OF PAGES 56	19a. NAME OF RESPONSIBLE PERSON USAMRC
a. REPORT U	b. ABSTRACT U	c. THIS PAGE U			19b. TELEPHONE NUMBER (include area code)

Table of Contents

Introduction.....	4
Body.....	4
Agreed Upon Statement of Work	4
Overview.....	6
Summary of progress in Year 1	6
Summary of progress in Year 2	6
Final Technical Report – University of Michigan (UM)	7
Aim 1: Probe requirements, modeling, etc.	7
Refine requirements, develop Monte Carlo simulations and analytic models.....	7
Image reconstruction.....	9
Aim 2: Probe component selection and prototype construction	9
Aim 3: Probe demonstrator construction	9
Aim 4: Phantom studies and performance evaluation	11
Imaging studies -- UM.....	11
Adaptations for human use	13
Final Technical Report – West Virginia University (WVU)	14
1. General.....	14
2. Prototypes of prostate imaging PET systems at WVU – final phase.....	15
3. Development of PET panel modules for the dedicated PET prostate imager.....	18
4. Development of the cooled liquid light guide for the PET panel modules.....	19
5. Spinoff project – imaging of OB GYN cancers.....	20
Key Research Accomplishments.....	20
Reportable Outcomes	21
Publications, abstracts, and presentations	21
Other reportable outcomes.....	22
Conclusions.....	23
So what?.....	23
References.....	23
Appendices.....	23

INTRODUCTION

The scope of the research is the investigation of the concept of the dedicated prostate PET imager composed of an endorectal PET probe and a partial PET imager ring operating in a coincidence. The probe placed close to the prostate is a high resolution element of this system, utilizing the magnification PET imaging concept. The University of Michigan team's responsibility is the design and simulation of the concept, construction of the external partial PET ring, and image reconstruction of the resultant laboratory prototype(s) assembled at the University of Michigan. The WVU partner's primary responsibility is in comparative design, construction and validation of the prostate probe based on Silicon Photomultiplier technology. While this Final Report summarizes progress from all years of the grant, progress in Year 3 is highlighted while progress for Years 1 & 2 is detailed in previous Annual Reports for this project.

BODY

Agreed Upon Statement of Work

The Statement of Work agreed upon among the participating parties and the granting agency is shown below. Tasks required for this project that are substantially complete are shaded in green

<i>Aim / Task</i>	<i>Month (from the start)</i>	<i>Contributing/ <u>Responsible Party</u></i>
Aim 1: Probe requirements and modeling (Michigan)		
Refine probe requirements	1-3	MP/ <u>NC</u>
Develop Monte Carlo simulations	1-6	SH/ <u>NC</u>
Incorporate device measurements from prototypes in Aim 2	6-12	SH/SM/ <u>NC</u>
Develop image reconstruction	1-12	SH/ <u>NC</u>
Predict probe performance & evaluate	3-12	SH/MP/SM/ <u>NC</u>
Refinements of models, image reconstruction, and performance evaluation methods	12-36	SH/MP/SM/ <u>NC</u>
Aim 2: PET probe component selection/validation and prototyping (WVU)		
Technical design selection (options)	2-4	JP/ <u>NC/SM</u>
Selection of SiPM modules	3-4	JP/ <u>SM</u>
Designing and building prototypes	5-8	AS/BK/ <u>SM</u>
Prototype testing	6-9	AS/JP/ <u>SM</u>
Technical design selection (final)	9	JP/ <u>NC/SM</u>
Aim 3: Probe demonstrator construction/Interface to PET (WVU / Michigan)		
Produce electronics boards	10-11	JP/ <u>SM</u>
Assemble SiPMs with electronics	12	JP/ <u>SM</u>
Mechanical assembly with enclosure	10-11	<u>BK</u>
DAQ assembly/DAQ software	6-9	JM, <u>JP</u>
Laboratory performance tests / Intrinsic performance evaluation/Attestation	10-12	AS/JP/ <u>SM</u>
Interface with PET ring at Michigan	12-18	AS/SM/SH/ <u>NC</u>
Performance testing / characterization of probe/ring	18-24	AS/SM/SH/ <u>NC</u>
Aim 4: Phantom Imaging studies and performance evaluation (Michigan / WVU)		
Construct phantoms	12-24	SH/MP/SM/ <u>NC</u>
Conduct phantom imaging studies	18-30	SH/MP/SM/ <u>NC</u>

Compare with performance predictions from Aim 1	18-36	SH/ <u>NC</u>
Summarize Research Results (Michigan / WVU)		
Clinical applicability of prostate probe	30-36	MP/SM/ <u>NC</u>
Device designs for next stage	30-36	MP/NC/ <u>SM</u>
Determine next funding steps (if any)	36	<u>MP/SM/NC</u>

<i>Resource</i>	<i>Abbreviation</i>	<i>Role / Location</i>
Neal Clinthorne	NC	PI, Michigan
Morand Piert, MD	MP	Co-inv, Michigan
Sam Seoung Huh	SH	Graduate Student Research Assistant, Michigan
Stan Majewski	SM	PI, WVU
James Proffitt	JP	WVU
Alexander Stolin	AS	JLab (subcontract)
John McKisson	JM	JLab (subcontract)
Brian Kross	BK	JLab (subcontract)

In the next sections, results for each task in the above Statement of Work are summarized. To aid the flow of the presentation, a detailed technical report follows the description of work performed for each task.

Overview

Summary of progress in Year 1

In the first year of the project, the highest risk elements of the prostate probe were addressed including potential performance improvements over conventional PET and methods for constructing the high performance endorectal detectors necessary to implement such an instrument. Calculations and Monte Carlo studies showed that significant performance improvements were feasible in terms of better spatial resolution for a given level of image noise, and a number of feasible endorectal detector designs based on LYSO arrays and high performance photodetectors were developed and tested. Progress was further detailed in the Annual Report for Year 1.

Summary of progress in Year 2

Year 2 progress continued along the same categories as progress in Year 1. In particular, various image reconstruction methods were evaluated, requirements for allowable size were refined, the performance and applicability of silicon photomultiplier technologies from various vendors were evaluated, and technologies necessary to adapt the probe to human use were investigated. These included potential probe shell designs as well as technologies for tracking the position and orientation of the probe. Integration of two probe technologies with the partial-ring PET system at Michigan began. In a parallel effort, probes were interfaced to an external LYSO panel detector at WVU.

Summary of progress in Year 3

Work in the final year focused on integrating the probes created in this project to various external detector systems, the partial-ring BGO detector at Michigan (Figure 5) and an external panel-based detector at WVU (Figure 10). The ultimate goal of connecting the probe as an add-on to a commercial PET ring (which was *not* part of the funded project), while of interest to the two PET scanner vendors contacted, proved infeasible due to present limitations of their internal resources. Integration of a probe created at WVU with the panel detector demonstrated better spatial resolution than a state-of-the-art commercial PET instrument (although this limited-angle tomography design suffers from poorer resolution in the direction perpendicular to the probe face. Demonstration of resolution capabilities from the two systems are shown in Figs. 9 and 11 below.

Summary of next steps

The funded work successfully demonstrated that endorectal PET probes—made possible by recent advances in new photodetectors and high-resolution detectors—can provide improved images over conventional external-ring PET alone and the immediate next step should be to seek money for building an instrument that can be tested in human subjects. Nevertheless, much of the molecular imaging work in prostate PET is currently being overshadowed by the apparent lack of PET prostate tracers and by advances in magnetic resonance imaging and spectroscopy (MRI/MRS), which makes funding prospects (at least at NIH) uncertain. As noted later in this report, a pre-proposal to fund further development has been submitted to the European Commission. In addition to several European institutions, partners include West Virginia University and the University of Michigan. Also, an SBIR proposal with a US partner is planned for constructing an MRI-compatible, endorectal PET + ultrasound probe.

Progress is described in more detail in the UM and WVU sections of the report that follow.

FINAL TECHNICAL REPORT – UNIVERSITY OF MICHIGAN (UM)Aim 1: Probe requirements, modeling, etc.*Refine requirements, develop Monte Carlo simulations and analytic models*

Based on detailed discussions with urologists during the first two years, allowable external size of the probe was refined and at 32mm in the largest cross-section allowed for more detector material than originally anticipated. This is important because a greater detector volume directly translates to improved probe performance. Geant 4 Monte Carlo simulations using the Zubal anthropomorphic phantom derived from an organ-segmented CT scan discretized into 4mm x 4mm x 4mm voxels were used to calculate the relative sensitivity to point sources of activity placed within the prostate. Figure 1 plots relative sensitivity

against the axial extent of external PET rings up to 15 cm for two probe sizes: the originally proposed 6mm x 10mm x 40mm probe and a larger 10mm x 24mm x 40mm probe. Note the increased sensitivity for the larger probe, which is significantly higher than both the external PET ring alone and the PET ring + smaller probe. Given the size of the necessary photodetectors and support electronics, 24mm is somewhat larger than can be accommodated but sensitivity of a practical instrument will lie midway between the two probe size—still a significant increase over both the smaller probe and a conventional PET scanner.

Another goal of this investigation was to evaluate the effect of the spatial resolution of the probe detector and the external detector—especially the potential need for depth-of-interaction (DOI) resolution in each detector. To this end, an analytic expression describing the intrinsic resolution of the probe/external detector setup was developed that included effects of depth-of-interaction resolution and positron acolinearity. The diagram in Figure 2, in which two general PET detectors are depicted, shows parameters for the following resolution expression:

$$R_D \approx \sqrt{\left((1-\alpha)^2(\sin^2 \theta_1 r_{D1}^2 + \cos^2 \theta_1 r_{C1}^2) + \alpha^2(\sin^2 \theta_2 r_{D2}^2 + \cos^2 \theta_2 r_{C2}^2) + (\alpha(1-\alpha)D \times 0.0088)^2\right)}$$

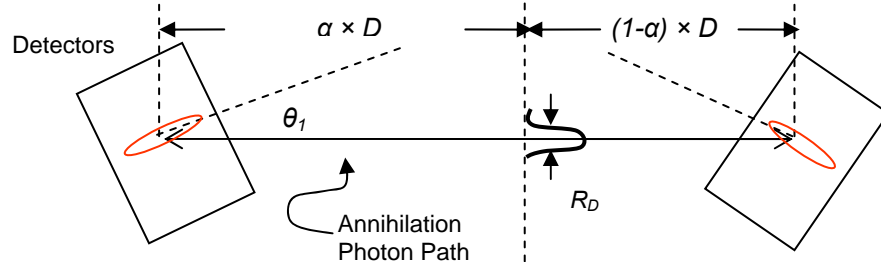


Figure 2. Diagram defining symbols for resolution expression. The parameter α is the fractional distance along the line-of-response between the two detectors. Red ellipses represent position estimation uncertainties (r_{D1} , r_{C1} , r_{D2} , r_{C2}).

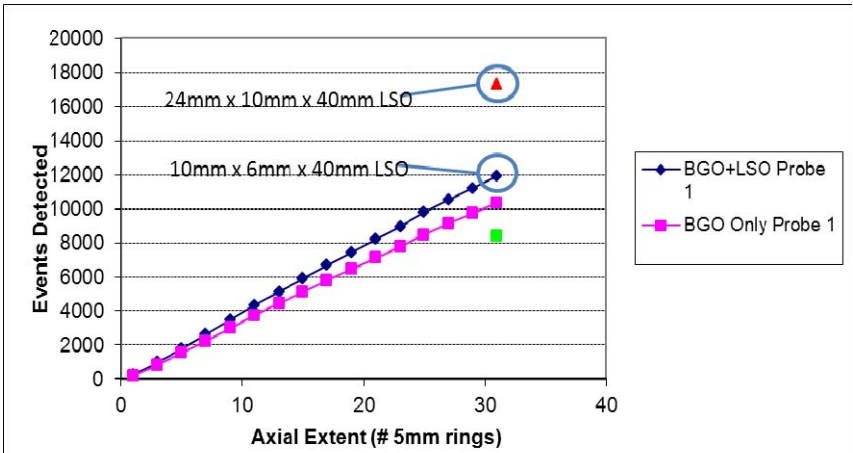


Figure 1. Plot of relative sensitivity vs. axial extent of PET ring for two endorectal probe sizes (sensitivity for the larger probe is shown only for the largest ring). The magenta curve (and green square) show how insertion of each probe *reduces* the number of external ring-ring coincidences from sources located within the prostate.

For the plots in Figure 3, the endorectal probe is assumed to be detector D_1 and the external detector D_2 . Intrinsic resolution as a function of distance from the probe is shown for angles of incidence 0–45° for probes having no additional depth resolution over the 10mm scintillator depth (green curve), 2mm FWHM resolution (blue), and 1mm FWHM resolution (red). From these curves, depth resolution of 2mm FWHM or better is highly desirable for prostate imaging. Probes using double-sided readout developed at WVU consistently demonstrated DOI resolution of 1mm FWHM or better and therefore meet this requirement.

Also from Figure 3, note that the region of high resolution extends a considerable distance from the probe—a phenomenon that is further demonstrated in measurements shown in Figures 9 & 10. This must be tempered with the fact that probe resolution is not isotropic: as the distance from the source to the probe increases, angular coverage decreases resulting in worse resolution along the axis between the probe and source. For a full external ring PET system, the resolution in this direction decreases to the resolution of the external ring scanner as the probe-to-source distance increases. For configurations that use only a partial-coverage external detector (as shown in Figure 10 of this report), blurring along this axis will increase more rapidly with distance.

The need for good spatial resolution was evaluated in a preliminary study in which 3D spherical lesions of uniform, known intensity, known location, and various sizes were embedded in a randomly varying background and viewed with measurements having intrinsic resolutions ranging from 1mm to 10mm FWHM. There was no source of noise other than the random background. The activity within region-of-interest templates derived from both the measurement system and the known size and location of the lesions was integrated and the first- and second-moments of this test statistic were computed from typically 1000 background realizations. The statistics were subsequently used to calculate the area under the receiver operating characteristic curve (AUC) for the task of lesion detection as a function of lesion size and intrinsic resolution. Results are shown in Figure 4 where, clearly, good spatial resolution is important for separating the lesion from the random distribution of background activity (such as non-specific uptake that may vary among patients). The caveat is that the random activity distribution likely does not accurately reflect background statistics in patients but it nevertheless makes a case for the need for good spatial resolution.

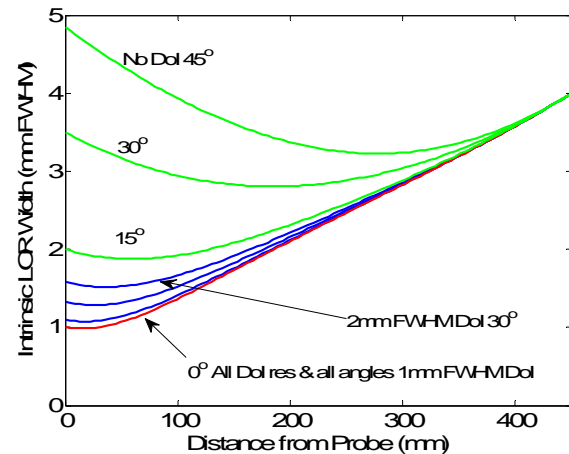


Figure 3. Plots of intrinsic spatial resolution vs. distance from the probe detector for probes having 1mm FWHM depth resolution (red), 2mm FWHM depth resolution (blue), and no depth resolution other than due to the 10mm thick scintillator. Results are shown for several angles-of-incidence.

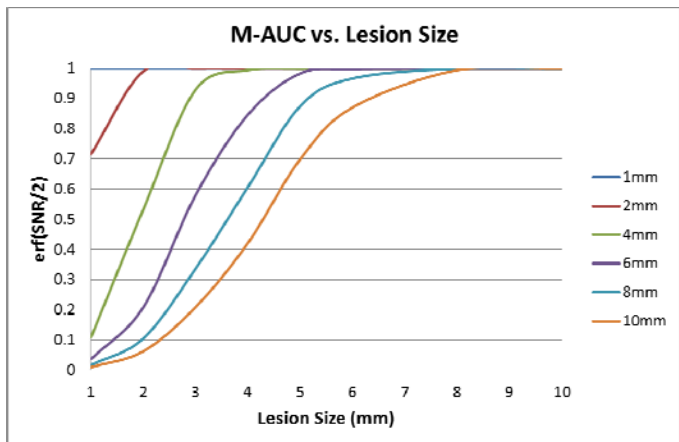


Figure 4. AUC-0.5 for the task of lesion detection plotted against lesion size for measurement systems having intrinsic Gaussian resolutions ranging from 1mm to 10mm. The maximum, and most desirable, value is unity; zero reflects no detection ability. Note the rapid decrease in performance when the lesion size is near to or smaller than the system resolution.

Image reconstruction

While statistically motivated reconstruction for PET is a well established technology, reconstructions that combine datasets having differing measurement uncertainties or that combine limited-angle high-resolution data with that from a conventional PET ring remains a fruitful research area. Over the course of this project, we developed several techniques for reconstructing the multi-resolution data. In year 1, we reported on a sliding-window list-mode maximum likelihood reconstruction that can be used to form images in real time. This may well be useful for probe positioning; however, it is highly desirable to use the measurements in a manner that extracts as much information as possible about the underlying radiotracer distribution in the prostate. In years 2 and 3 of the project, additional multi-resolution reconstruction methods were developed: a 2D post-smoothed, penalized maximum likelihood algorithm for testing predictions of high-resolution PET performance and a full 3D volume PET algorithm based on a list-mode maximum likelihood formulation. A feature of the 2D formulation is that it can asymptotically achieve the limiting noise level at any reconstructed spatial resolution (although “asymptotic” means that *enough* coincidence events must be collected and is a topic of current research). The present implementation of the list-mode 3D reconstruction is fairly computationally intensive because of the need to model the spatial resolution for each type of coincidence event (probe-ring and ring-ring in this case); moreover, the response of probe-ring coincidences is spatially varying. Development work continues under different funding, and the penalty function and post-smoothing features will be added to the 3D list-mode algorithm as resources permit. The 2D and 3D algorithms were used to reconstruct images shown in Figures 8 and 9.

The WVU group also developed “laminographic” and maximum likelihood methods for the limited-angle data acquired using the prototype prostate probes in coincidence with an LYSO-based panel detector. Results are shown in the WVU section of this report.

Aim 2: Probe component selection and prototype construction

During the project, several versions of the probe were constructed using scintillator arrays with dimensions as small as 0.8mm x 0.8mm x 10mm read out by arrays of sensL or Hamamatsu silicon photomultipliers (SiPMs). Two versions of these were delivered to UM, as noted in the next section. Over the course of the investigation, silicon photomultiplier technology has progressed significantly and prototype development work continues at WVU although the technology is already at a point where it is feasible to construct high-resolution endorectal probes for human use.

Aim 3: Probe demonstrator construction

For the demonstration studies conducted at UM to validate the theoretical concepts of Aim 1, a partial-ring benchtop PET system constructed from BGO block detectors scavenged from a CTI 931 PET scanner was expanded from 16 to 24 detector blocks (covering an angle of 67.5°). An advantage of the device, which was originally developed to study dual-ring magnifying PET systems for small animal imaging, is that it can be easily reconfigured. A VME based FPGA card concentrates all trigger and status signals and generates the control signals for event coordination and detector readout. The easily reprogrammed unit has been used to set up a number of high resolution PET experiments including the dual-ring small field-of-view configuration shown at left in Figure 5. The benchtop system also has an object turntable in order to emulate a full-ring PET instrument. Two prototype probes with associated signal amplifiers and power supplies were developed at WVU and delivered to UM—one with single-sided readout and one with double-sided readout for depth-of-interaction estimation. Both configurations are shown in Figure 6. Printed circuit boards and connections add considerable inactive bulk to the units but as shown in Figure 13, the issue has been addressed in newer designs. Figure 7 shows position, depth-of-interaction, and energy resolutions for the double-sided unit measured at WVU. Importantly, depth resolution is ~1mm

and similar to spatial resolution in the transverse directions so one should expect a negligible angle-of-incidence effect as shown in Figure 3.

The original intent was to interface these SiPM-based probes to benchtop system for phantom measurements. This was indeed accomplished but the event digitization electronics developed at UM for these probes suffered from excessive noise. Both charge-integrating and peak-sensing ADCs were tested but the position and energy resolution achieved was worse than that obtained at WVU. The readout scheme for the probes is presently being redesigned under internal funding to use sampling ADCs, which will avoid use of long delay lines on the position signals and problems associated with peak-sensing ADCs.

As an alternative to the WVU probes for validating predictions, high-resolution silicon pad detectors were instead used to emulate the probes. A detector assembly comprising two silicon detectors having 26×40 arrays of $1\text{mm} \times 1\text{mm} \times 1\text{mm}$ detector elements is shown at right in Figure 5. Detectors used for probe experiments shown in the next section used 16×32 arrays of $1.4\text{mm} \times 1.4\text{mm} \times 1\text{mm}$ pads. As the event digitizing electronics at UM are refined, the WVU probes will be substituted for the silicon detectors in the benchtop PET system. For completeness, note that new-generation WVU probes *were* tested in conjunction with LYSO panel detectors to validate the prostate PET concept and to compare performance to that obtained from a current-generation PET/CT scanner in studies described on page 15 of this report.

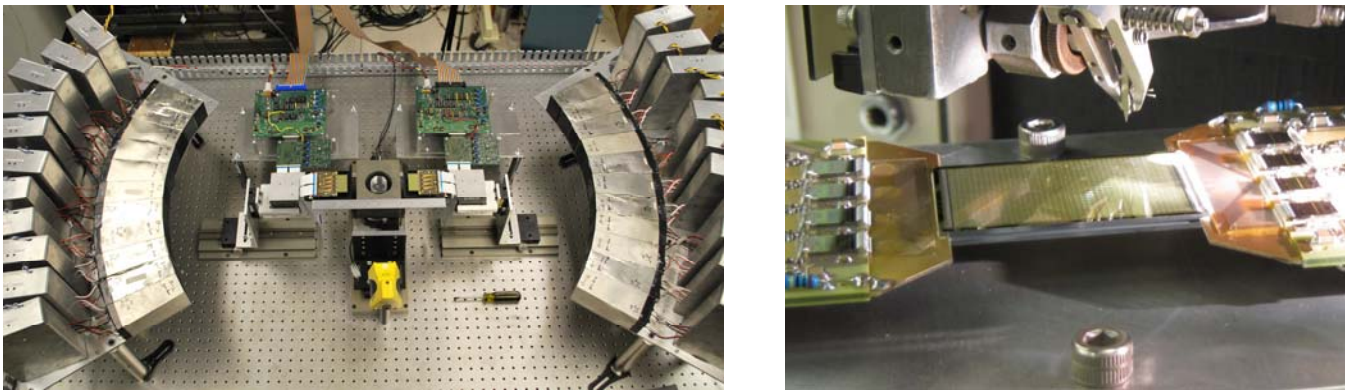


Figure 5. Right: Construction phase of the partial ring PET system at Michigan showing 22 of 24 BGO detector blocks at 500mm radius. Left: a high resolution silicon “probe” detector under construction.

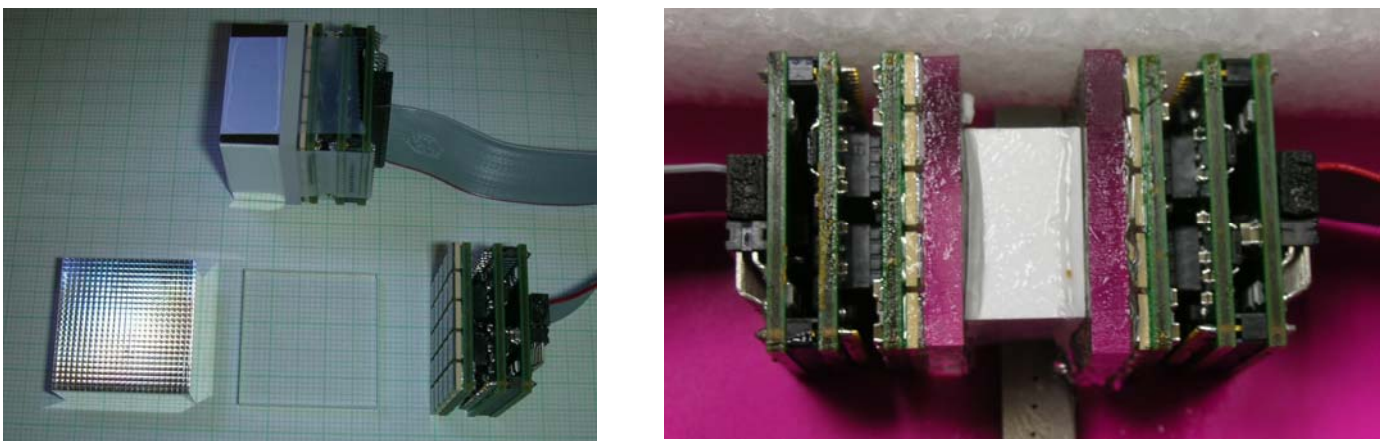


Figure 6. Two prostate probe prototypes developed at WVU and delivered to UM for evaluation. Left: single-sided, non-DoI readout probe. Individual components including the scintillator array, the light-guide, and SiPM array are shown below an assembled probe. Right: double-sided readout with $\sim 1\text{mm}$ FWHM DoI resolution.

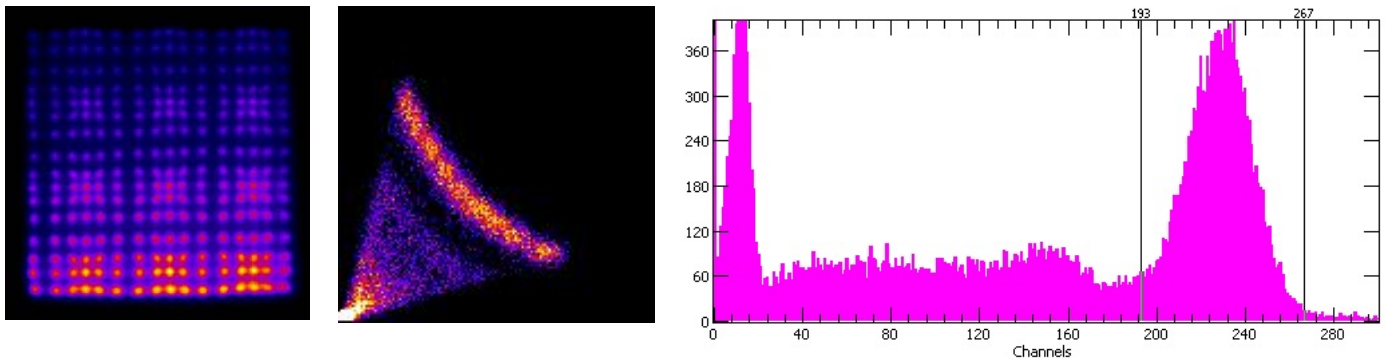


Figure 7: Performance of double-sided detector (measured at WVU). Left: crystal response with array irradiated from bottom of image; note the expected exponential decrease in intensity and the ability to separate each crystal in the array. Center: sum of front-side SiPM array vs. same for back-side for Na-22 needle source positions varying by steps of 1mm in depth demonstrating good DoI resolution. Right: typical energy histogram showing 12.7% FWHM energy resolution at 511 keV.

Aim 4: Phantom studies and performance evaluation

Imaging studies -- UM

Using the benchtop PET system described above in conjunction with silicon detectors to emulate the high-resolution probes, a number of 2D and volume PET studies were conducted. Typical results from the 2D investigation are shown in Figure 8 where the imaging geometry is shown to the left. The “probe” having a Gaussian equivalent resolution of ~ 1 mm FWHM is located 66.6mm from the center of a 45mm diameter resolution phantom filled with ^{18}F -FDG. The radius of the external PET ring is 500mm and the resolution of the external detectors is nominally 6mm in the circumferential direction and 12mm in the axial direction. Reconstructions of the phantom from the ring data alone are shown to the left in Figure 8 while reconstructions from the complete ring data augmented with high-resolution probe data are shown as the rightmost image. The spatial resolution is significantly improved in the vertical direction and, as expected, is not significantly improved in the horizontal direction due to the limited view-angle nature of high-resolution information. In practice, images would be displayed by slicing the reconstructed PET volume parallel to the face of the probe (vertically in this 2D reconstruction) such that high and isotropic resolution would be seen in each 2D slice.

Figure 9 shows reconstructed images reconstructed from PET data acquired using a volume PET (3D) probe configuration using only probe-ring coincidences. Three Na-22 point sources were located approximately 15mm from the probe. The minimum distance between sources is 1.5mm. Using the list-mode volume PET reconstruction, data were reconstructed into a 3D array of 0.2mm x 0.2mm x 0.2mm voxels. Projections through the reconstruction volume along the x-, y-, and z-axes are shown left to right in the top row. The typical orientation that probe images might be viewed is the leftmost image in Figure 9. Even though the external detector only has 6mm x 12mm spatial resolution, reconstructed images still clearly separate even the sources separated by 1.5mm, which demonstrates the high resolution performance of the probe geometry. Projections through the image volume along the y- and z-directions demonstrate the non-isotropic resolution due to the limited view-angle of this geometry. Resolution along the limited-angle direction (the x-axis in this case) becomes worse as the distance from the probe to the source increases.

The bottom row of Figure 9 shows plots of the width of the reconstructed PSF as a function of distance from the probe (red squares). As expected, resolution decreases as the source-to-detector distance increases. For reference, the solid line shows the predicted resolution. Resolution is slightly different in the y- and z-directions due to the non-isotropic resolution of the external ring (6mm for y vs. 12mm for z). Even at distances of 10cm from the probe, resolution is still 2mm in y and 2.5mm in z. This provides high confidence that a practical high-resolution endorectal probe will demonstrate significant improvements over conventional, external-ring PET.

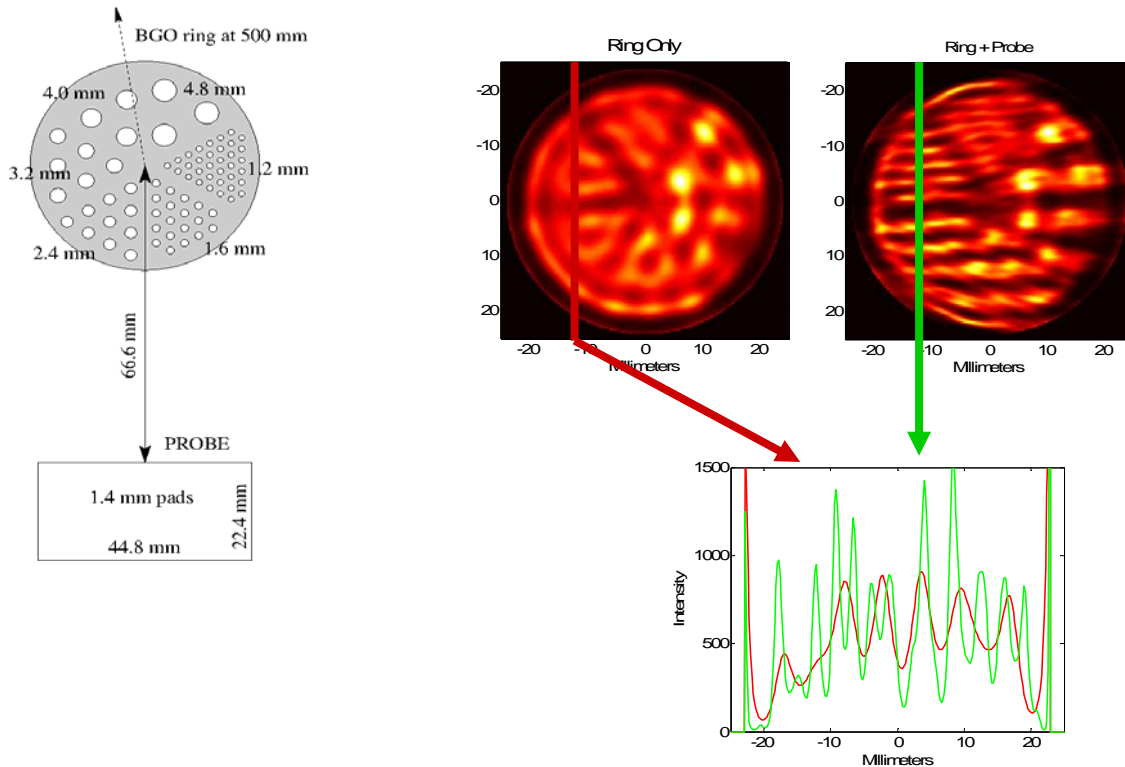


Figure 8. Left: imaging geometry and phantom dimensions (diameter: ~ 45 mm). Measurements were performed using the partial BGO ring shown in Figure 5 in a single-slice geometry with high-resolution silicon sensor (probe) located at ~ 4 cm from the edge of the resolution phantom. Probe resolution is equivalent to ~ 1 mm FWHM. External detector resolution was nominally 6mm FWHM. Right: Images reconstructed from complete external ring data only (left) and the same data augmented with measurements from the emulated probe (right). Images shown are rotated 90° clockwise and then flipped top-to-bottom from diagram at left. The plots in the right panel show profiles through both reconstructed images showing the increased resolution resulting from use of the probe. While the probe provides improved resolution along the vertical direction in this case (which would also extend perpendicular to the page for a 3D PET acquisition), resolution in the direction of the “66.6 mm” axis shown on the left decreases to that of the external-ring PET instrument due to the limited view-angle information intrinsic to the measurement geometry.

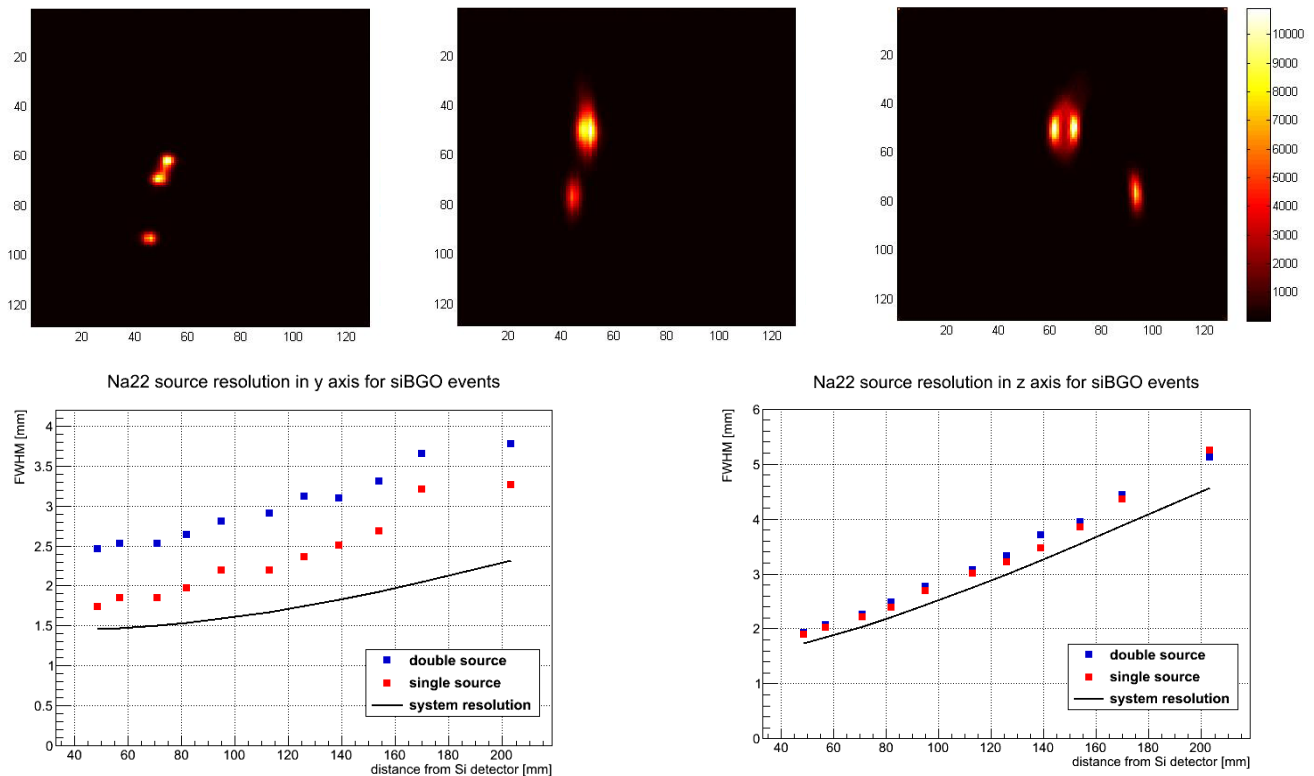


Figure 9. Top row: Reconstructions of three Na-22 point sources separated by 1.5mm and 6mm measured with a limited-angle 3D PET probe geometry using silicon “probe” located ~15mm from the sources and partial-ring BGO system shown in Figure 5. Left: image projection of reconstructed image volume along x-axis showing high-resolution capability of probe. This is the typical orientation in which images from the probe would be viewed in prostate imaging---more-or-less “coronal” to the prostate. Center: projection along y-axis. Anisotropic resolution due to limited high-resolution view-angle is evident. Right: projection of reconstruction along z-axis. Bottom row: width of reconstructed PSF as a function of distance from the probe is shown with the predicted resolution (solid curve) along y-axis (left) and z-axis (right). The “single source” resolution (red squares) is most relevant to performance. Resolution varies between y and z because the external detector has ~6mm FWHM resolution in y and ~12mm in z. As expected, the region of high-resolution extends a significant distance from the probe detector. Images were reconstructed into a volume of 0.2mm x 0.2mm x 0.2mm voxels.

Adaptations for human use

Design studies for packaging the probe electronics and tracking were conducted in year 2 of the project with the aid of students from a Biomedical Engineering design course at UM. Probe shell materials, allowable size, and position-tracking hardware were evaluated. Conclusions of this investigation were that black Delrin demonstrated the appropriate strength, sterilizability, and light-shielding properties for the probe shell. Studies of tracking hardware demonstrated that a pulsed DC tracking system from Ascension Technology Corporation had acceptable error over the small tracking volume needed for the probe as long as the larger (8mm) sensors were used. In this analysis, two sensors were attached to the probe to provide redundant information. Experience at WVU using a similar tracking system has shown less favorable results and a mechanical alternative (Microscribe MX– www.3d-microscribe.com) provided acceptably low tracking error. More detail on probe mechanics was provided in the year 2 annual report.

FINAL TECHNICAL REPORT – WEST VIRGINIA UNIVERSITY (WVU)**1. General.**

The purpose of this project was to validate in phantom studies the theoretical concept of the resolution magnifying endorectal prostate PET probe used in conjunction with an accompanying medium-to-high resolution PET imager, in order to visualize the fine detail in the PET imaging agent uptake in the prostate cancer and in the immediate vicinity of the organ.

During the duration of the project we have constructed and tested several prostate PET probe designs and prototypes with increasing level of performance. Initially our probes were PET only, then we have designed and preliminary tested probes operating in a hybrid system with the TRUS probe, also of an elastography type. In the final stretch of the project (still continuing) we have also designed and tested elements of an MRI-compatible system that could operate together with MRI. The last variant was a recent add-on based on the feedback we received from the NIH Bethesda molecular imaging group of Dr Peter Choyke, as well as from Dr Martin Pomper from JHU, who developed new improved prostate PET imaging agents. Both groups are interested in assisting us with preparation of a dual modality PET/MRI prostate imaging system, as well as in validation of the system in pilot clinical trials.

We have also expanded on our initial plan of combining the WVU-made probes with the partial PET ring detector at UM, and have indeed tested few other variants of probe+PET systems, including single panel and dual-panel PET detectors, providing simplified mobile system mounted on a rotating gantry. This substantial project extension was possible due to additional matching funds provided by the in-house WVU funds. The amount of WVU funds was about double ($> \$200k$) of the WVU portion of the UM/WVU DOD grant.

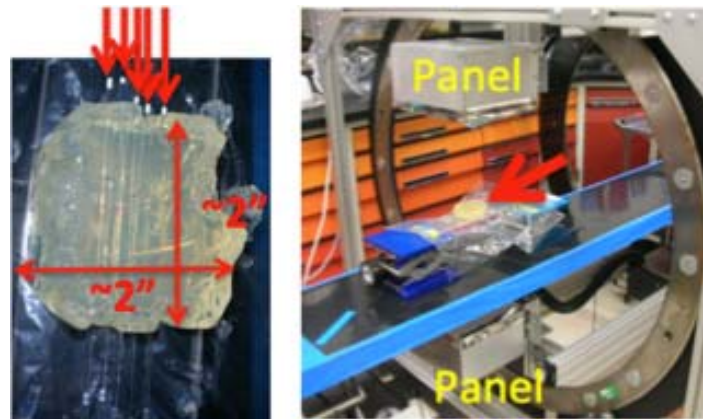


Figure 10. During the imaging study, the five-capillary/gelatin phantom (picture shown at left with arrows showing the positions of the five capillaries; the phantom position marked with the red arrow in the right picture) was placed on a support plate in ~ the central plane between the two panel PET modules mounted on the rotating gantry. During PET Probe + PET Panel study, the probe was placed under the phantom to simulate the geometry of the endorectal PET probe operating with a single (top) PET Panel module. Distances were as follows: panel-to panel: ~50cm, probe to phantom: ~1cm, probe to top panel: ~18 cm. The Panel-Panel PET scan was 13 positions, 15 degree apart.

2. Prototypes of prostate imaging PET systems at WVU – final phase.

Our yearly reports documented the variety of the concepts and several of the tested system variants. Most of the tested systems used PET modules without the Depth of Interaction (DOI) correction.

We first include our best non-DOI system results showing the advantage of the dedicated PET system with a high resolution PET probe. The system (Figure 10) had two panel modules of 20x15 cm FOV each with 2mm intrinsic spatial resolution, and the developed probes were used in a coincidence system with the panels. Three-way comparison was performed between the Siemens mCT PET/CT scanner, the high resolution PET Panel+Panel mobile scanner and the Probe+PET Panel system by imaging the resolution phantom and demonstration capillary/gelatin phantom. The selection of the second phantom was dictated not by the resemblance of the prostate-imaging situation, but by ease of controlling conditions to demonstrate the potential advantages of the higher resolution system in a highly limited tomographic geometry of the Probe+Panel configuration. The Panel+Panel and the Probe+Panel data sets were reconstructed with 20 iterations of the MLEM algorithm. Reconstructed voxel sizes were isotropic 0.35 mm and 1 mm for probe+panel and panel+panel detector systems, with reconstruction volume sizes of 286 by 286 by 286 and 150 by 150 by 150 voxels respectively. No post-processing has been applied to the images shown in Figure 11. Modulation ratios (signal – background / signal in percent) for each distinguishable peak in the projection plots were calculated and results are presented in Table I.

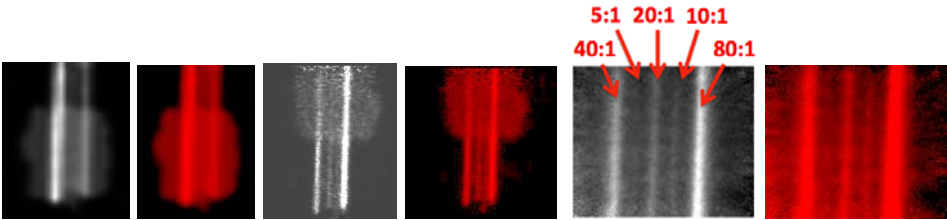


Figure 11. Images of the capillary/gelatin obtained from (left to right): mCT PET/CT (second image with the logarithmic intensity scale to emphasize smaller features), panel+panel PET (shown in linear and log scales), and 1mm probe+PET panel (linear and log scale). While the PET/CT scanner was able to detect the two capillaries with the highest concentrations (80:1 and 40:1), the panel+panel PET also identified the 20:1 capillary, the probe+panel system also visualized the 20:1 and 10:1 capillaries, even with a slight hint of the 5:1 capillary.

Concentration ratios	Probe + panel (%)	Panel + panel (%)	Clinical PET-CT (%)
5 to 1	Not visible	Not visible	Not visible
10 to 1	10	Not visible	Not visible
20 to 1	23	20	Not visible
40 to 1	41	47	35
80 to 1	54	67	64

Table 1. Peak modulation ratios for the three scanner systems.

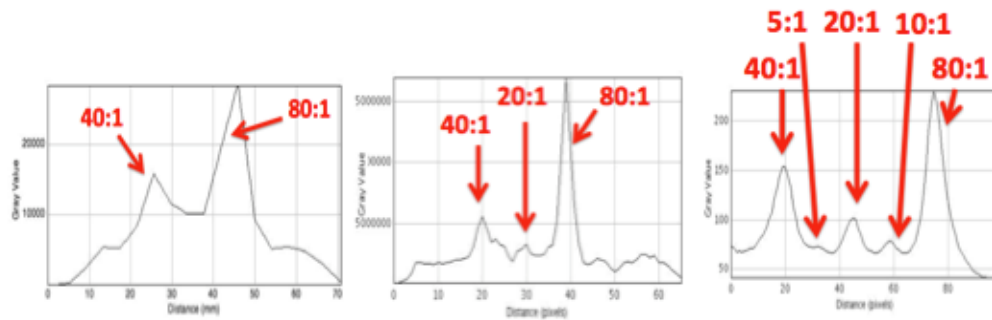


Figure 12. Profiles through the PET/CT scanner, Panel+Panel and Probe+Panel images, shown in the Fig. above.

The final **PET probe** (*designed to be MRI-compatible*) is based on the monolithic variant of SiPMs manufactured by Hamamatsu. The building block - Multi-Pixel Photon Counter (MPPC) model S10943-3344MF-050 monolithic array measures about $\frac{1}{2}$ " by $\frac{1}{2}$ " and consists of an array of 4 x 4 (16) ~ 3 mm x 3 mm active imaging elements (pads).

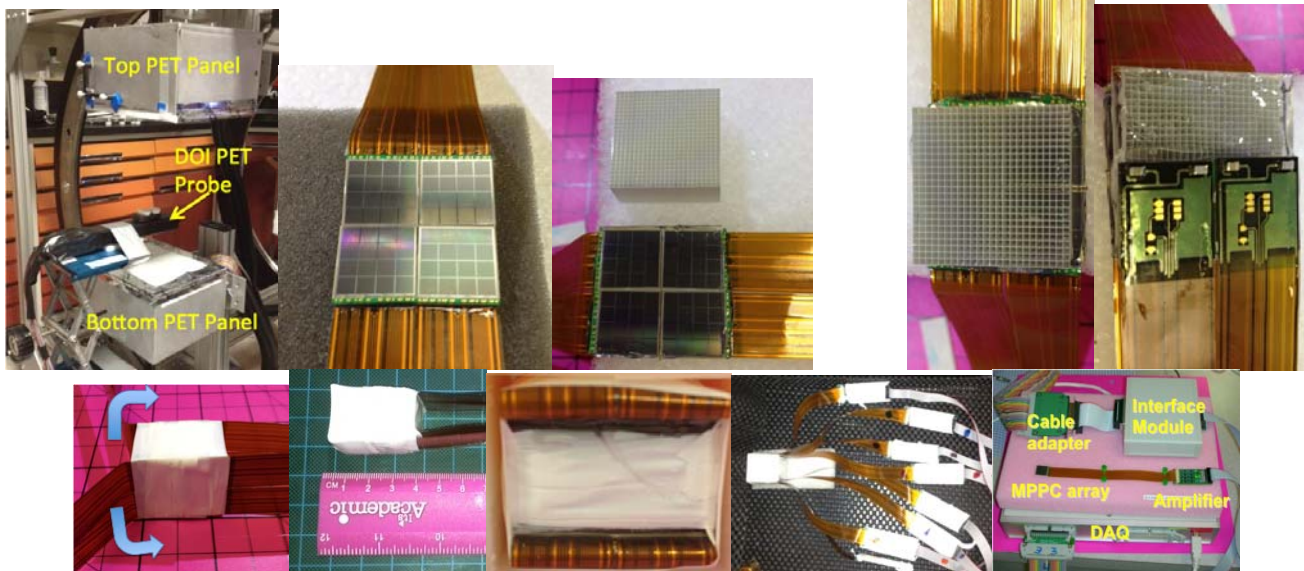


Figure 13. Final DOI PET probe prototype. Top Left: The experimental setup used in the series of measurements, composed of two high resolution (2mm) panel detectors used in conjunction with several PET probes. From top left to bottom right: the preferred DOI capable PET probe during stages of production. The probe was made using eight monolithic MPPC modules arranged in two 2x2 butted configurations and coupled at both ends of a 10mm thick LYSO 24x24 array of 1mm pitch pixels to form a 24mm x 24mm transversal coverage PET probe. The four cables from the front MPPC modules were tightly bent by 180 deg to exit in the same direction as the other four cables. The custom-made (AiT Instruments) amplifier boards were attached at the ends of ~ 20 cm long low profile flat cables that can be arranged to fit into a handle of the probe. In this way, there was no active electronics in the vicinity of the RF coil and the organ to be imaged. However, this design is not appropriate for TOF operation. Bottom: Each monolithic MPPC array is equipped with an amplifier board, interface module, and cable adaptor produced by AiT Instruments. The 32 ADC channel data acquisition (DAQ) box, also from AiT Instruments, is digitizing the $8 \times 4 = 32$ output channels from the probe.

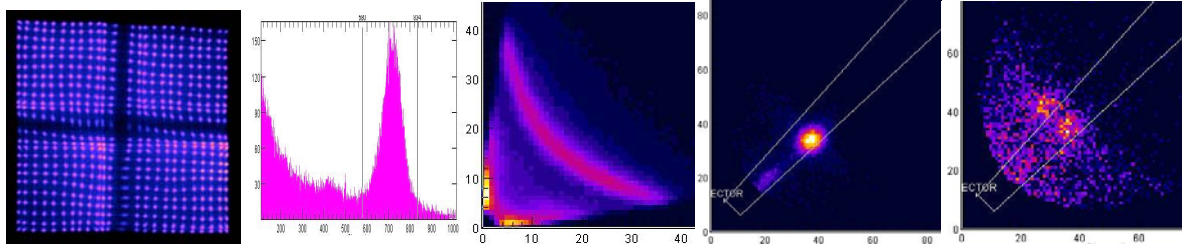


Figure 14. Left: All 24x24 1mm LYSO pixels are separated in this raw image from one of the sides of the 1" DOI module, including the region of the joints between the MPPC modules region, where only 25% signal decrease in signal amplitude is observed. Example of the summed energy spectrum from two sides for one of the 1x1x10mm LYSO pixels is shown as second from left. Energy resolution in the range from 13% to 15% @ 511 keV was measured across the whole surface. Center: Plot of the two signal outputs from the two ends measured for one of the LYSO pixels in the case of a broad 511 keV beam. Using electronically collimated 511 keV beam from a single point (~1mm) Na22 source gives a well-defined (~1mm FWHM) point is obtained in the same plot. Finally, two 0.5mm inner diameter capillaries placed at 1.25mm center-to-center can be seen well separated at right, attesting to the sub-mm DOI spatial resolution of the probe.

In a series of studies, we have demonstrated that temperature correction can be implemented and that one can operate from room temperature to over 110°F with no visible impact on performance, except the requirement to correct (increase) bias voltage at higher temperatures. Temperature sensor is placed on each monolithic module and calibration curves can be obtained for all monolithic MPPC modules. Voltage bias will be adjusted, as necessary, from the software controlled power supplies.

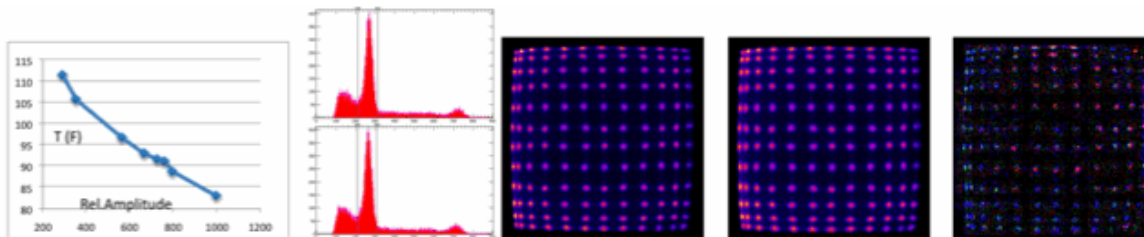


Figure 15. Left: Monolithic array temperature tests with the Proteus LYSO array with 1mm step, 10mm thick. Dry coupling via 3mm thick glass window. Left: Gain change with bias voltage kept constant @ 74.4V. Examples of Na22 energy spectra obtained from individual 1mm LYSO pixels. Top: @87.7F & 73.4V; 14.4% FWHM @511 keV, bottom: @111.1F & 74.4V; 14.8% FWHM @ 511 keV. Center/Right: Examples of raw images obtained at 87.7F & 73.4V (left image) and at 111.1F & 74.4V (center image). Right image of the three is the subtracted image, demonstrating that the pixel positions did not visibly shift between the two operational points, and they stay well

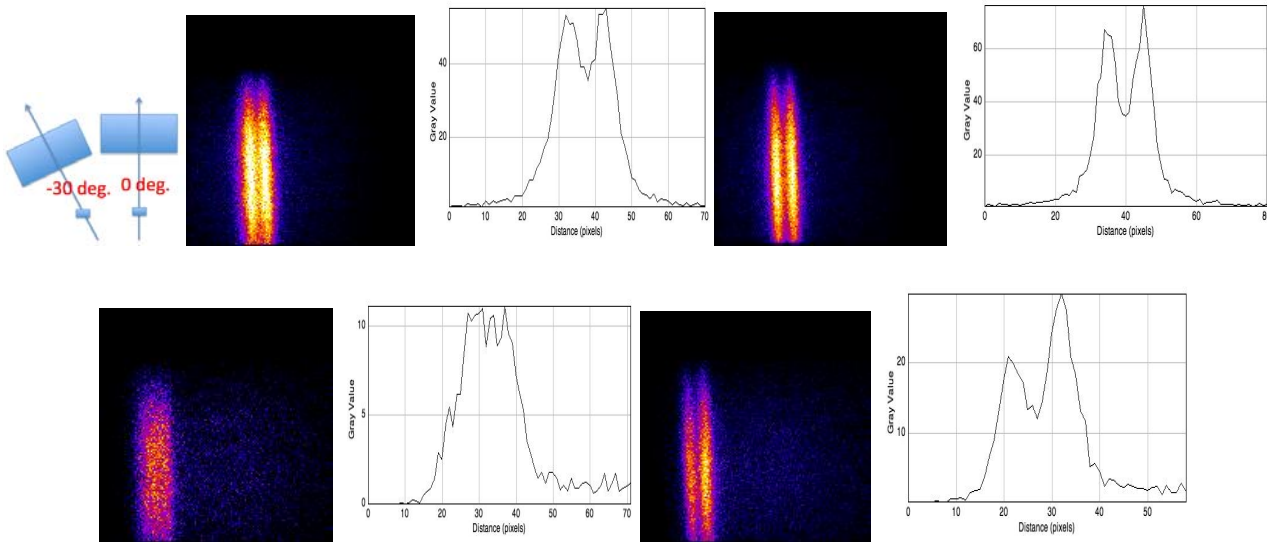


Figure 16. Pilot studies of the impact of the DOI effect on reconstruction in the single panel – PET probe geometry. Back projection laminography algorithm used. The top panel PET detector (see setup picture in the corresponding previous figure) was set at a stereotactic angle of 0 deg. (top results) and -30 deg. (bottom results) in the measurements with the two-capillary phantom, composed of 0.5mm inner diameter capillaries spaced at 2.5mm center-to-center. The images were obtained without (left) and with (right) the DOI correction. The event depth position in the 10mm thick scintillator was estimated from the DOI parameter (Output 1 divided by the sum of Output 1 and Output 2) to about 1mm accuracy. The improvement in reconstructed spatial resolution due to correction for the depth of interaction is obvious.

3. Development of PET panel modules for the dedicated PET prostate imager.

We have also designed the next generation PET panel modules to operate with the PET probe. Four **panel PET imagers** (*designed to be MRI-compatible*) will be based on the Hamamatsu MPPC technology, packaged in 1" modules of 5x5 3 mm MPPCs placed at a 5 mm center-to-center pitch. The MPPC arrays will be arranged in sets of 2x2 to form ~5 cm active modules with 100 MPPCs. Each PET panel will be built with twelve of these modules arranged in a 4 by 3 matrix. Each module will be coupled to a 34 by 34 array of 1.5 (pitch) x 1.5 (pitch) x 15 mm LYSO scintillators from Proteus, covering a 51 mm x 51 mm area. All 12 scintillation arrays will be coupled to the twelve SiPM modules via one larger cooled window covering the 20x15cm field of view.

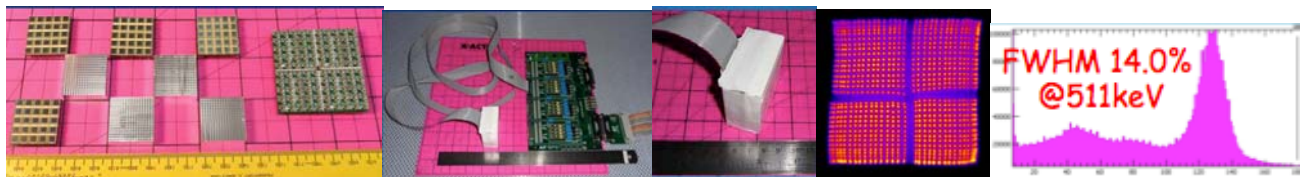


Figure 17. Left: Assembly of ~5 cm square compact modules built with four 25 MPPC arrays assembled on one resistive readout base from AiT Instruments with 4ch per 100 MPPC module. Four 1.5 mm step 10 mm thick LYSO arrays from Proteus coupled to form one compact 32x32 pixel module. In this implementation, intended for MRI-compatible WVU PET ring imager, there are no amplifiers or other active components, except MPPCs, on board the detector modules, but in the distant electronics board (at the other end of the 2 m long cables). There are 4 output channels per module. Example of the raw image @ 511 keV and of the energy spectrum from the whole 5 cm module after energy calibration. Despite large gaps between individual 3 mm MPPCs very good and uniform performance is attained.

4. Development of the cooled liquid light guide for the PET panel modules

Full size prototype of the cooled optical spreader window for the panel PET modules will be developed, as the means to ***lower and stabilize*** the temperature of the SiPM arrays, using the optical liquid cooling and re-circulation system. We will evaluate its performance and long-term operational stability with the prototype PET panel module. This novel (submitted for a patent) concept is a high risk/high benefit technical element of the proposal, requiring development in Phase I of a reliable recirculating cooling system. Preliminary demonstration studies at WVU confirmed that it is possible to lower the temperature of a small SiPM module by flowing cooled silicone optical liquid inside a thin (<5mm) optical window placed between the scintillator array and the SiPM array. For the PET panels we propose that each 20x15cm panel module has a matching size cooled window. This technique, if mastered, guarantees the uniform delivery of the cooling power ***directly to the sensitive element*** – the SiPM. Other techniques, such as blowing cool air and/or cooling electronics from the back of the board stacks result in inefficient cooling and temperature gradients, and are also much more bulky.

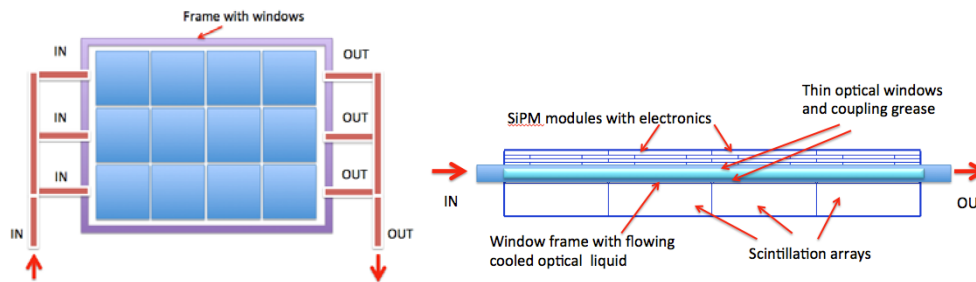


Figure 18. Schematic of a large liquid cooled window variant proposed for application in the PET panel modules. A tight array of 4x3 SiPM modules, each of

approximately ~5cm x 5cm active field of view (FOV), covers the useful total FOV of about 20 x 15cm in a panel PET module implementation. Left: view through the window looking into the SiPM array. Right: side view with the optical cooled liquid window shown inserted between the scintillator array and the SiPM modules.



Figure 19. Early stage demonstration experiment with a simple low-power cooling system using portable thermoelectric coolers. Pictures at left show first the light guide window alone and the temperature map during cooling operation, obtained with the infrared camera – thermometer. One of the windows of the light guide (top) was 1mm thick glass, and the other ~200 micron thick Mylar foil. Both windows were glued to small profile Al frame with two inlet and two outlet small diameter tubes. Flexible plastic tubing was used for liquid circulation. The circulating liquid in the pilot test was Poly-Sil-Silicone Fluid 50CS. In the center is shown a single array of 2x2x15mm LYSO crystals placed under the liquid light guide with a SensL ArraySL-4P9 SiPM array on top. The SiPM module is equipped with the low power 4ch readout from AiT Instruments. The temperature of the light guide in this mechanical test went down to about 50 F, with the surrounding laboratory room temperature at 73 F. Right: demonstration that the liquid light guide operates as the optical spreader window and that cooling of the SiPMs can be achieved, and that, as expected, it improves the performance of the imager. A new variant of the light guide of about 3mm thick liquid volume enclosed between two Mylar windows was inserted between the ArraySL-4P9 SiPM module and a 2x2x15mm LYSO array. Coupling grease was used between the SiPM module and the Mylar, as well as between the scintillator array and the second Mylar window. Left is an image at ~75F (no cooling of the liquid) and at right the one obtained at about (est.) ~55F (with cooling on). It can be seen that the pixel separation, especially at the corners, is substantially improved with the cooling on. In addition, the amplitude of the signal increased by ~45% when the SiPM module was cooled, at the set bias voltage of 29.9 V.

5. Spinoff project – imaging of OB GYN cancers.

As a result of the PET system development for prostate imaging, it was proposed that a modification of such a system could be used in imaging OB GYN cancers. There are already plans for submitting proposals, one via the European Union funding channel with both University of Michigan and WVU as research partners, and the second through the SBIR NIH channel with a US company partner.

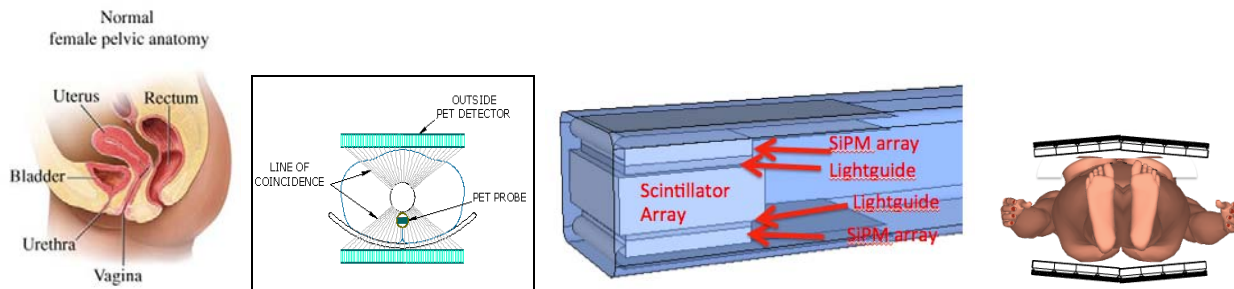


Figure 19. Relevant anatomic details and schematic drawings of a compact high resolution (~1mm FWHM) abdominal PET imager with an inserted intravaginal or endorectal PET probe. Minimal but fully functional PET system is composed of two panel detectors, each built with 16 individual ~5cm in size MRI-compatible PET modules (second from left. Each of the modules is made from a matrix of pixellated LYSO crystals coupled to an array of solid-state Silicon Photo-Multipliers (SiPM). In addition to the external panels, an insertable sub-mm resolution endorectal and/or intravaginal PET probe is also employed. The placement of the probe depends on the organ and its part to be imaged. For uterus imaging the endorectal variant is more appropriate. The schematic of the Depth of Interaction (DOI) PET probe is shown at second from right. The scintillator array is read from both sides by monolithic SiPM arrays. The probe has a profile of less than 3.75cm in any dimension. At right is shown the optimal variant of the scanner with four panel modules providing a better angular coverage of the patient. The probe is also included. In both variants all the PET components are MRI compatible. (The optical component of the system is not shown in these sketches.)

KEY RESEARCH ACCOMPLISHMENTS

- The concept of PET using a high-resolution endorectal probe was demonstrated.
- Probes are anticipated to have 1–2mm x (the external PET ring intrinsic resolution). Resolution improvement is anisotropic due to limited tomographic view-angle (<180°) of the high-resolution data. For the situation in which an incomplete external detector is used, spatial resolution decreases as distance to the probe increases because of the decreasing angular view. Nevertheless, for sources in the prostate, resolution can still be good as demonstrated in Figures 9 & 11.
- Technologies necessary to construct a probe practical for testing in human subjects have been developed. These are based on advances in photodetectors and in particular, silicon photomultiplier arrays. An important aspect of this work is that probes having excellent 3D position resolution (i.e., with depth-of-interaction estimation) were developed. Good depth resolution was predicted to be as well as shown to be important to achieving good performance for prostate imaging.
- Prototype external shell designs, materials, and tracking hardware necessary to translate this work to human use were developed and were reported in the Year 2 Annual Report.

REPORTABLE OUTCOMESPublications, abstracts, and presentations

1. Clinthorne NH, Majewski S: High resolution PET probe for prostate imaging, Symposium on Intraoperative Imaging, Gargano-Mattinata, Italy, Aug. 28–30, 2009 (Invited)
2. Huh SS, Han L, Rogers WL, Clinthorne NH: Real time image reconstruction using GPUs for a surgical PET imaging probe system. *2009 Nuclear Science Symposium Conference Record*. p. 4148–4153.
3. Studen A, Burdette D, Chesi E, Cindro V, Clinthorne NH, Cochran E, Grosicar B, Honscheid K, Kagan H, Lacasta C, Llosa G, Linhart V, Mikuz M, Stankova V, Weilhammer P, Zontar D: Performance of the MADEIRA PET probe prototype. *2009 Nuclear Science Symposium Conference Record*. p. 3111–3115, 2009.
4. Cochran E, Clinthorne NH, Chesi E, Honscheid K, Huh S, Kagan H, Lacasta C, Mikuz M, Rackers J, Smith S, Studen A, Weilhammer P: High resolution PET using concentric silicon and scintillator rings. *Presented at SORMA XII, May 24 – 28, 2010, Ann Arbor, MI USA*.
5. Garibaldi F, et al, TOPEM: a PET TOF endorectal probe, compatible with MRI and MRS for diagnosis and follow up of prostate cancer, *Accepted for presentation at the World Molecular Imaging Conference (WMIC), September 11–15, 2010 Kyoto, Japan*.
6. Delfino E, Majewski S, Raylman R, Stolin A: Towards 1mm PET Resolution Using DOI Modules Based on Double-Sided SiPM Readout, *IEEE Nuclear Science Symposium Conference Record* p. 3442–3449, 2010.
7. Studen A, Chesi E, Cindro V, Clinthorne NH, Cochran E, Grosicar B, Honscheid K, Kagan H, Lacasta C, Llosa G, Linhart V, Mikuz M, Stankova V, Weilhammer P, Zontar D: A silicon PET probe. *Nucl. Ins. Meth. Phys. Res. A*, 648:S255–S258, 2011.
8. Garibaldi F, De Leo R, Ranieri A, Loddo F, Floresta M, Tamma C, Gabrielli A, Giorgi F, Cusanno f, Musico P, Perrino R, Finocchiario P, Cosentino, L, Pappalardo A, Meddi F, Maraviglia B, Giove F, Gili T, Capuani S, Turisini M, Clinthorne N, Huh S, Majewski S, Lucentini M, Gricia M, Giuliani F, Monno E: TOPEM: a multimodality probe (PET TOF, MRI and MRS) for diagnosis and follow up of prostate cancer. *IEEE Nuclear Science Symposium Conference Record*, p. 2442–2444, 2010.
9. Huh SS, Cochran E, Honscheid H, Kagan H, Smith S, Rogers WL, Clinthorne NH: The first generation prototype of a surgical PET imaging probe system. *IEEE Nuclear Science Symposium Conference Record*, p. 3197–3204, 2010.
10. Studen A, Chesi E, Cindro V, Clinthorne NH, Cochran E, Grosicar B, Honscheid K, Huh SS, Kagan H, Lacasta C, Llosa G, Linhart V, Mikuz M, Stankova V, Weilhammer P, Zontar D: Report on the MADEIRA PET probe. *IEEE Nuclear Science Symposium Conference Record*, p. 1755–1758, 2010.
11. Lacasta C, Clinthorne NH, Llosa G: The PET Magnifier Probe (Chapter 11), in *Radiation Physics for Nuclear Medicine*, Cantone MC, Hoeschen C (eds), Springer, 2011
12. Garibaldi F, et al, TOPEM: a PET TOF endorectal probe, compatible with MRI and MRS for diagnosis and follow up of prostate cancer, *Presented at the World Molecular Imaging Conference (WMIC), September 11–15, 2010 Kyoto, Japan*.
13. Cochran E, Chesi E, Clinthorne NH, Honscheid H, Huh S, Kagan H, Lacasta C, Mikuz M, Rackers J, Smith S, Studen A, Weilhammer P, Wolf E: High resolution PET using concentric silicon and scintillator rings. *Presented at the 2010 IEEE Nuclear Science Symposium, Oct. 25–31, 2010, Knoxville, TN USA*.

14. Clinthorne NH, Majewski S, Brzezinski K, Huh SS, Carr J, Chen Z, Salomonsson E, Yande A: High resolution PET instruments for prostate imaging. *Presented at the 2011 IMPaCT Conference, March 9–12, 2011, Orlando, FL.*
15. Huh SS: Preliminary study of an intraoperative PET probe imaging system. *PhD dissertation, Department of Biomedical Engineering, University of Michigan, 2011.*
16. Clinthorne NH, Cochran E, Kagan H, Huh SS, Lacasta C, Linhart V, Mikuz M, Smith D, Studen A, Weilhammer P: Recent results from a “dual-ring” high resolution PET demonstrator. *Presented at the 2011 Annual Meeting of the Society of Nuclear Medicine, June 3-8, 2011, San Antonio, TX.*
17. Clinthorne N, Cochran E, Chesi E, Grosicar B, Honscheid K, Huh S, Kagan H, Lacasta C, Brzezinski K, Linhart V, Mikuz M, Smith DS, Stankova V, Studen A, Weilhammer P, Zontar D: A high-resolution PET demonstrator using a silicon “magnifying glass.” *Physics Procedia*, 37:1488–1496, 2012.
18. Clinthorne N, Brzezinski K, Chesi E, Cochran E, Grkovski M, Grosicar B, Honscheid K, Huh S, Kagan H, Lacasta C, Linhart V, Mikuz M, Smith DS, Stankova V, Studen A, Weilhammer P, Zontar D: Silicon as an unconventional detector in positron emission tomography. *Nucl. Ins. Meth. Phys. Res. A*, 699:216–220, 2013.
19. Clinthorne N, Majewski S, Stolin A, Raylman RR, Carr J, Chen Z, Salomonsson E, Yande A, Huh SS, Kagan H, Smith S, Brzezinski K, Studen A: Progress in development of a high-resolution PET prostate imaging probe. *Presented at the 2011 IEEE Nuclear Science Symposium, October 23-29, 2011, Valencia, Spain.*
20. Majewski S, Stolin A, Delfino E, Martone P, Proffitt J: High resolution fast stereotactic PET imager for prostate biopsy. *IEEE Nuclear Science Symposium Conference Record*, p. 3406–3409, 2011.
21. Majewski S, Proffitt J, Stolin A: Development of a mini gamma camera for prostate imaging, *IEEE Nuclear Science Symposium Conference Record*, p. 4024–4029, 2011.
22. Studen A, Brzezinski K, Chesi E, Cindro V, Clinthorne NH, Cochran E, Grosicar B, Grkovski M, Honscheid K, Kagan H, Lacasta C, Llosa G, Mikuz M, Stankova V, Weilhammer P, Zontar D: Silicon detectors for combined MR-PET and MR-SPECT imaging, *Nucl. Ins. Meth. Phys. Res. A*. In press.
23. Clinthorne N: Prostate imaging technology (Invited). *SNMMI Categorical Seminar: Application Specific Medical Imaging*. Presented at the 2012 Annual Meeting of the Society of Nuclear Medicine and Molecular Imaging, June 9, 2012, Miami Beach, FL.
24. Stolin AV, Majewski S, Jaliparthi G, Raylman RR: Construction and testing of a prototype high-resolution, silicon photomultiplier-based tandem positron emission tomography system, *Submitted to IEEE Trans. Nucl. Sci.* 2012.
25. Clinthorne N, Brzezinski K, Chesi E, Grkovski M, Grosicar B, Kagan H, Lacasta C, Mikuz M, Smith S, Stankova V, Studen A, Weilhammer P, Zontar D: Advantage of augmenting standard PET data with high resolution information, *Presented at the 2012 IEEE Nuclear Science Symposium, October 26 – November 3, 2012, Anaheim, CA.*

Other reportable outcomes

26. A preproposal aimed at further development of high-resolution imaging technology relevant to prostate for both PET and SPECT in combination with MRI has been submitted to the European Commission Framework Programme 7 (October 5, 2012).

CONCLUSIONS

During the course of the project several investigations were conducted to validate the concept of a high-resolution endorectal probe for prostate imaging. To this end, the project was successful in that high-resolution probes based on the magnifying PET concept were both predicted and shown to achieve 1–2mm spatial resolution in a field-of-view appropriate for prostate imaging. Moreover, the *technologies necessary to construct such devices were developed, tested, and shown to perform better than initial expectations*. In particular, PET camera modules having intrinsic resolution of 1mm or less in all three spatial dimensions (i.e., modules with depth-of-interaction resolution) were developed as shown in this report. These two results provide high confidence that an external PET ring enhanced with a high-resolution endorectal PET probe will provide significant spatial resolution improvements in prostate imaging over external-ring PET alone. Additionally, a PET instrument using an internal probe and external panel detector—even though it is only capable of limited-angle tomography—may find use as part of a prostate biopsy instrument guided by molecular imaging. These techniques are also applicable for high-resolution PET imaging of other organ systems and pathologies as noted in the body of this report.

Although prostate imaging performance of the instrument will almost surely be superior to present external-ring PET instruments, there are several issues that cloud the next step. Chief among these is the role that PET may play in prostate imaging given the increasing performance of MRI/MRS and the apparent dearth of “suitable” PET tracers. One possible avenue is to create a multimodality PET/MRI instrument augmented with the high resolution probe although this is a relatively expensive option considering that the next—and much lower cost—step in reducing risk is most logically a PET-only endorectal probe to demonstrate that clinically useful high-resolution PET images can be obtained in human subjects. Another important issue encountered during the project was shrinking discretionary resources that PET manufacturers have to devote to such projects. Again, the most logical choice would be to design the high-resolution probe as a straightforward add-on to conventional external-ring PET scanners much as different coils can be added to an MRI machine. And although at least one major PET manufacturer showed interest, that interest was not backed up with a successful joint grant application to further development.

So what?

The project was successful in demonstrating that technologies for high-resolution molecular imaging (PET) of the prostate exist. If implemented, they will certainly provide better PET images than currently available (perhaps as good as **1mm x 1mm x 4–5mm** resolution rather than **5mm x 5mm x 5mm** resolution typical for external-ring PET). Such improved resolution may well change the view of limitations of current PET prostate imaging agents although an instrument capable of being tested in human subjects must first be constructed. Given the present directions of imaging technology and prostate imaging, it seems that the most reasonable next step will be to create an endorectal probe that can be used as an add-on to a commercial PET/MRI scanner; although as noted, this will have to wait for an appropriate expression of interest from PET/MRI scanner manufacturers.

REFERENCES

APPENDICES



Contents lists available at SciVerse ScienceDirect

Nuclear Instruments and Methods in Physics Research A

journal homepage: www.elsevier.com/locate/nima

Silicon as an unconventional detector in positron emission tomography[☆]

Neal Clinthorne^{a,*}, Karol Brzezinski^d, Enrico Chesi^e, Eric Cochran^b, Milan Grkovski^c, Borut Grošičar^c, Klaus Honscheid^b, Sam Huh^a, Harris Kagan^b, Carlos Lacasta^d, Vladimir Linhart^d, Marko Mikuž^c, D. Shane Smith^b, Vera Stankova^d, Andrej Studen^c, Peter Weilhammer^e, Dejan Žontar^c

^a Department of Radiology, University of Michigan, Ann Arbor, MI 48109-5610, USA

^b Department of Physics, Ohio State University, Columbus, OH, USA

^c Jožef Stefan Institute, Ljubljana, Slovenia

^d IFIC/CSIC University of Valencia, Valencia, Spain

^e CERN, Geneva, Switzerland

ARTICLE INFO

Keywords:

PET

Silicon detectors

Multiresolution imaging

Magnifying PET

ABSTRACT

Positron emission tomography (PET) is a widely used technique in medical imaging and in studying small animal models of human disease. In the conventional approach, the 511 keV annihilation photons emitted from a patient or small animal are detected by a ring of scintillators such as LYSO read out by arrays of photodetectors. Although this has been successful in achieving ~ 5 mm FWHM spatial resolution in human studies and ~ 1 mm resolution in dedicated small animal instruments, there is interest in significantly improving these figures. Silicon, although its stopping power is modest for 511 keV photons, offers a number of potential advantages over more conventional approaches including the potential for high intrinsic spatial resolution in 3D. To evaluate silicon in a variety of PET “magnifying glass” configurations, an instrument was constructed that consists of an outer partial-ring of PET scintillation detectors into which various arrangements of silicon detectors are inserted to emulate dual-ring or imaging probe geometries. Measurements using the test instrument demonstrated the capability of clearly resolving point sources of ^{22}Na having a 1.5 mm center-to-center spacing as well as the 1.2 mm rods of a ^{18}F -filled resolution phantom. Although many challenges remain, silicon has potential to become the PET detector of choice when spatial resolution is the primary consideration.

© 2012 Elsevier B.V. All rights reserved.

1. Introduction

As use of positron emission tomography increases in medicine, there is increasing demand for higher spatial resolution for imaging mouse and rat models of human disease as well as for improved detection of small tumors in many cancers [1,2]. The conventional approach to achieving higher resolution is to scale down crystal dimensions in scintillation detector configurations currently used in PET instruments. Although this has been successful in improving spatial resolution to 1–1.5 mm FWHM for small animal imaging, and arrays of new silicon photomultipliers have recently buoyed this effort, it remains challenging to achieve spatial resolution in the submillimeter regime at high detection efficiencies.

We have been investigating an alternative approach to achieving high spatial resolution: use of silicon as a detector for 511 keV annihilation photons rather than a high-Z scintillator such as LYSO [3]. In a separate effort, silicon has been considered for PET by Di Domenico et al. [4]. Although detection efficiency is significantly less than for dense scintillators (attenuation length 1.1 cm for LYSO vs. 5.0 cm for Si) and the photoelectric interaction efficiency is well below 1% at 511 keV, Compton interactions can be localized to high precision, which can result in instruments whose resolution is limited only by the range of the positron in tissue before annihilation and acolinearity of the annihilation radiation [5]. Moreover, it appears possible to achieve reasonable system efficiencies using a combined silicon/scintillator PET scanner [6]. In the past, we have applied this technology to single-slice demonstrators and devices compatible with nuclear magnetic resonance imaging (MRI) to evaluate the effect of strong magnetic fields on positron-range [7]. In the present study, we examine the use of silicon as the inner detector in a dual-ring, magnifying PET geometry. We focus here on the ability to achieve high spatial resolution in a field-of-view (FOV) appropriate for

[☆] This work was supported with funding from the US DHHS NIH Grant R01 EB430, the US Army CDMRP Grant W81XWH-09-1-0413, and the European Commission under FP7 EURATOM-FISSION Grant 212100 (MADEIRA).

* Corresponding author.

E-mail address: nclintho@umich.edu (N. Clinthorne).

imaging small animals such as mice and rats; nevertheless, the basic ideas can be extended to other magnifying geometries such as PET imaging probes that can be used to obtain high-resolution images in pre-specified regions-of-interest in human subjects [8].

2. High resolution PET

Shown at left in Fig. 1 is the dual-ring, magnifying geometry. An inner detector ring, in this case comprising high-resolution silicon detectors, surrounds a small FOV and is in turn surrounded by a conventional position-sensitive scintillation detector used in PET. Note that three significant coincidence events can occur, which we denote as Si-Si, Si-BGO, and BGO-BGO. Si-Si and BGO-BGO events clearly support the highest and lowest spatial resolution, respectively. Resolution for mixed Si-BGO coincidences, however, varies with the fractional position along the line-of-response (LOR) connecting the two detectors.

For two PET detectors D_1 and D_2 separated by distance D (millimeters), the resolution R_D transverse to a line-of-response (LOR) at distance $\alpha \times D$ from D_1 is given by

$$R_D \approx \left[(1-\alpha)^2 (r_{C1}^2 \cos^2 \theta_1 + r_{D1}^2 \sin^2 \theta_1) + \alpha^2 (r_{C2}^2 \cos^2 \theta_2 + r_{D2}^2 \sin^2 \theta_2) + (\alpha(1-\alpha)D\delta)^2 \right]^{1/2} \quad (1)$$

where $0 \leq \alpha \leq 1$ is the fractional distance along the LOR starting at D_1 , θ_i is the angle-of-incidence of the LOR on each detector, and $\delta = 0.0088$ rad is the FWHM angular uncertainty due to acollinearity of the annihilation radiation in water. Intrinsic resolution

(FWHM) for each detector in the transverse (circumferential) and depth directions is denoted as r_{Ci} and r_{Di} , respectively.

Eq. (1) shows that resolution along the LOR is dominated by the detector closest to the source. Detectors having high resolution, such as achievable with silicon, can thus provide excellent resolution in the magnifying geometry of Fig. 1. At right in Fig. 1 is the intrinsic resolution plotted against distance from the silicon detector for three pad sizes (0.5 mm, 1.0 mm, and 1.4 mm square) in coincidence with detector located at distance 570 mm having 6 mm FWHM intrinsic resolution. Even though the external detector has relatively poor circumferential resolution and no explicit depth-of-interaction estimation, spatial resolution within a FOV appropriate for pre-clinical imaging of small animals can be significantly better than 1 mm FWHM.

3. Demonstration Instrument

To demonstrate the principles of the magnifying geometry and the use of silicon for PET, the device shown in Fig. 2 was constructed atop a $1.2 \text{ m} \times 1.8 \text{ m}$ optical table. A partial ring of conventional PET BGO block detectors at 500 mm radius surrounds a partial “ring” consisting of four silicon-pad detectors located at a nominal radius of 70 mm from the center of the 45 mm diameter field-of-view. In order to acquire PET data over the angular range of 180° required for reconstruction, objects are typically rotated in 6° increments during data collection. To reduce the single-event rates in both silicon and BGO detectors (high rates lead to a large random coincidence rate and increase deadtime), sources are shielded with lead and collimated to a

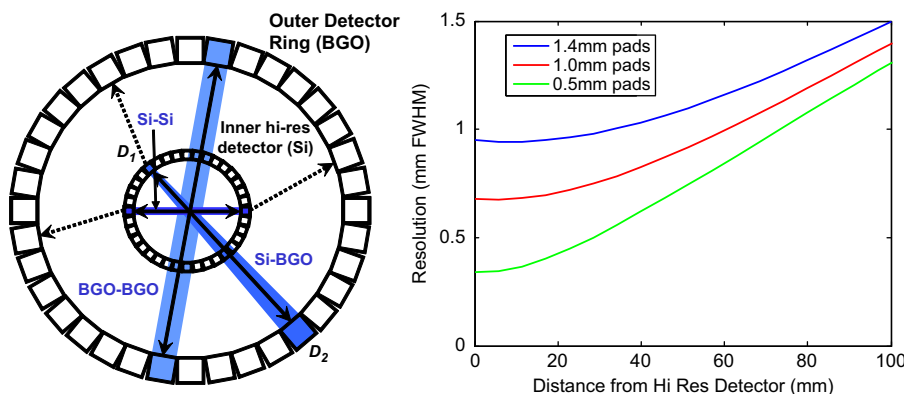


Fig. 1. Left: drawing of magnifying PET geometry showing three major coincidence types. Right: plot of resolution vs. distance from the silicon detector for Si-BGO coincidences for Si detectors having 0.5 mm, 1.0 mm, and 1.4 mm square pads in coincidence with a detector at distance 570 mm having 6 mm FWHM resolution.

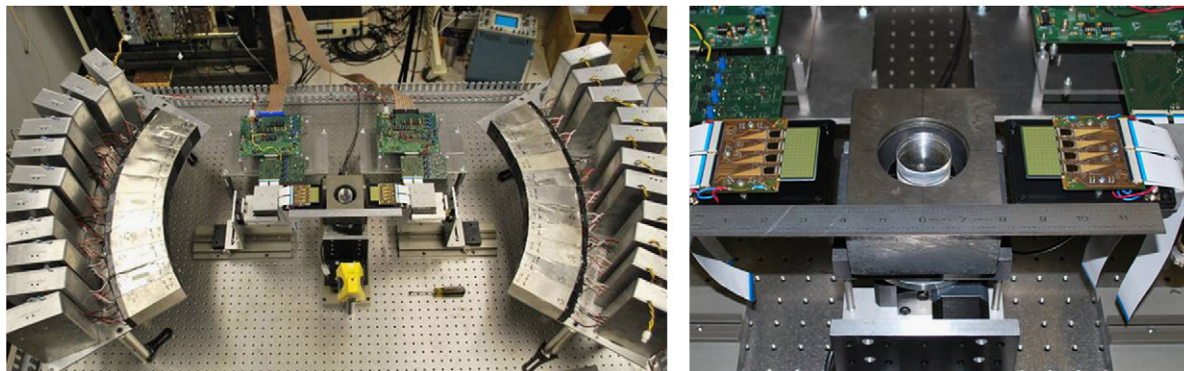


Fig. 2. Left: full test-bed showing partial-ring of BGO block detectors at 500 mm radius, inner “ring” of silicon detectors, slice collimation and object turntable. Right: closeup view of silicon detectors set up for the single-slice arrangement. Detectors are easily rearranged to emulate other geometries such as volume PET and imaging probes.

1 mm thick slice using tungsten (which is removed for volume PET data collection as described below). Trigger and position information from each detector in the setup is routed to a VME based data acquisition system that includes a programmable FPGA module (CAEN v1495) that controls types of coincidence events accepted as well as read out of position and energy information from all detectors. All information for each coincidence is stored in an event list, which is then post-processed (e.g. energy and timing windows can be altered post-acquisition) to generate data for image reconstruction.

3.1. Silicon detectors

The silicon detector technology used in this instrument is described by Meier et al. [10]. In the configuration shown in Fig. 2, a stack of two 512-pad, 1 mm thick silicon detectors flank each side of the field-of-view. The 1.4 mm \times 1.4 mm pads are arranged in a 32 \times 16 array and each is read out by four 128-channel VATA GP7 ASICs (Gamma-Medica Ideas, Northridge, CA, USA). Each channel of the ASIC has a fast (150 ns) shaper and leading-edge threshold trigger for coincidence timing and a slow (500 ns) shaper for pulse-height. Detectors are controlled and read out using a VME-bus based system of custom boards.

Although not important for this application, energy resolution is nominally 2.4 keV FWHM for the 59.5 keV peak of ^{241}Am and position resolution is outstanding being primarily determined by the pad size rather than by the range of the Compton recoil electron [5]. Timing resolution, which is important for PET, is relatively modest. There are two issues: time-walk and jitter. The large range of pulse-heights associated with Compton interactions when combined with the leading-edge trigger and shaped signal (150 ns peaking time) leads to a large time-walk (up to 150 ns). Jitter results from electronic noise and from the fact that the shape of the detector signal used for timing can vary considerably depending on the random 3D interaction position of photons as well as the direction of the Compton recoil electron in the detector [11].

3.2. Scintillation detectors

The BGO partial ring consists of 24 block detectors scavenged from a CTI 931 clinical PET scanner (vintage 1985). Each block has an eight (circumferential) \times four (axial) array of 6 mm \times 12 mm \times 30 mm BGO crystals. Interaction locations of annihilation photons are estimated by light-sharing among a 2 \times 2 array of photomultipliers. Original PET electronics were replaced with a simpler setup consisting of a fast channel and constant-fraction discriminator for coincidence timing and individual RC-CR shaping amplifiers for each PMT. Shaped signals for all blocks are routed to peak-sensing ADCs (CAEN v785) for position and energy estimation while timing signals are routed to the FPGA-based coincidence unit.

Performance of these older detector modules is far from the current state-of-the-art in PET. Position resolution is somewhat worse than 6 mm FWHM in the circumferential direction and 12 mm FWHM in the axial direction, energy resolution is $\sim 20\%$ FWHM, and timing resolution 12–20 ns FWHM at 511 keV. Nevertheless, as shown in the next section, these detectors provide a compelling demonstration of the resolution insensitivity predicted by Eq. (1) when detectors having poor resolution are located far from the field-of-view in a magnifying geometry.

4. PET imaging results

4.1. Single slice configuration

Reconstructed images from a resolution phantom for the single-slice setup are shown in Fig. 3. To collect approximately 10^7 Si–Si events in this low-efficiency configuration, the resolution phantom was repeatedly filled with 185 MBq of ^{18}F and imaged in 5 h sessions (2.7 half-lives). Rod diameters are 4.8 mm, 4.0 mm, 3.2 mm, 2.4 mm, 1.6 mm and 1.2 mm. Data collected in list-mode were processed into sinograms having 0.2 mm bins in radius and 0.9° steps in angle over 180° for all event classes. Images were reconstructed using a maximum likelihood expectation-maximization (ML-EM) algorithm that incorporated a system model accounting for the measurement resolution of each event class [9].

As expected, reconstructions using only BGO–BGO events exhibit the poorest spatial resolution—somewhat worse than 3 mm FWHM due to mispositioning errors in the first-generation PET block detectors. Reconstructions from the Si–BGO events, on the other hand, are significantly better and demonstrate the magnifying PET concept. Even the 1.2 mm rods can be resolved in this reconstruction. The Si–Si reconstructions show the best resolution and also lower noise than images reconstructed using only Si–BGO events.

An appropriate reconstruction method can combine all classes of events to obtain a single reconstruction (a maximum likelihood method was described by Clinthorne et al. [9]). Correctly done, using all events can improve the quality of the reconstruction over that obtainable from the highest resolution data alone and at worst will not result in a poorer quality image. In the present situation, where the Si–Si data comprise a large fraction of the total, we might not expect to see significant benefits from adding the lower resolution events. The left and right images in the bottom row of Fig. 3 are reconstructions that combine the Si–Si and Si–BGO events and then all events, respectively. As predicted, there is little to be gained by adding the lower resolution events in this case; however, when there are many fewer Si–Si events or when the desired reconstructed point spread function is broader, the lower resolution data may significantly reduce image noise.

4.2. Volume PET configuration

One of the advantages of the PET demonstrator is that it can be easily reconfigured to emulate different geometries. For the reconstructed images shown in Fig. 4, a *volume PET* imaging configuration was used in which the slice collimation was removed and the silicon detectors were rotated 90° such that the plane of each detector was perpendicular to optical table creating a 45 mm diameter \times 22 mm axial field-of-view. For initial studies, three ^{22}Na point sources were combined as shown at left in Fig. 4. Data were again collected in list-mode over a 5 h acquisition and the image volume was reconstructed directly from this data using a 3D list-mode maximum likelihood reconstruction. The top row of images in Fig. 4 shows three orthogonal planes through reconstructions of the Si–BGO events (the colored lines corresponding to the plane of each image outlined by the same color). While the sources separated by 6 mm are easily distinguished, those separated by 1.5 mm are not. Reconstructions from the Si–Si events for a similar set of orthogonal planes are shown in the bottom row. All three points are clearly separated.

5. Discussion and conclusion

Although silicon has a lower detection efficiency for a given volume than LYSO, it is a promising PET detector when high spatial

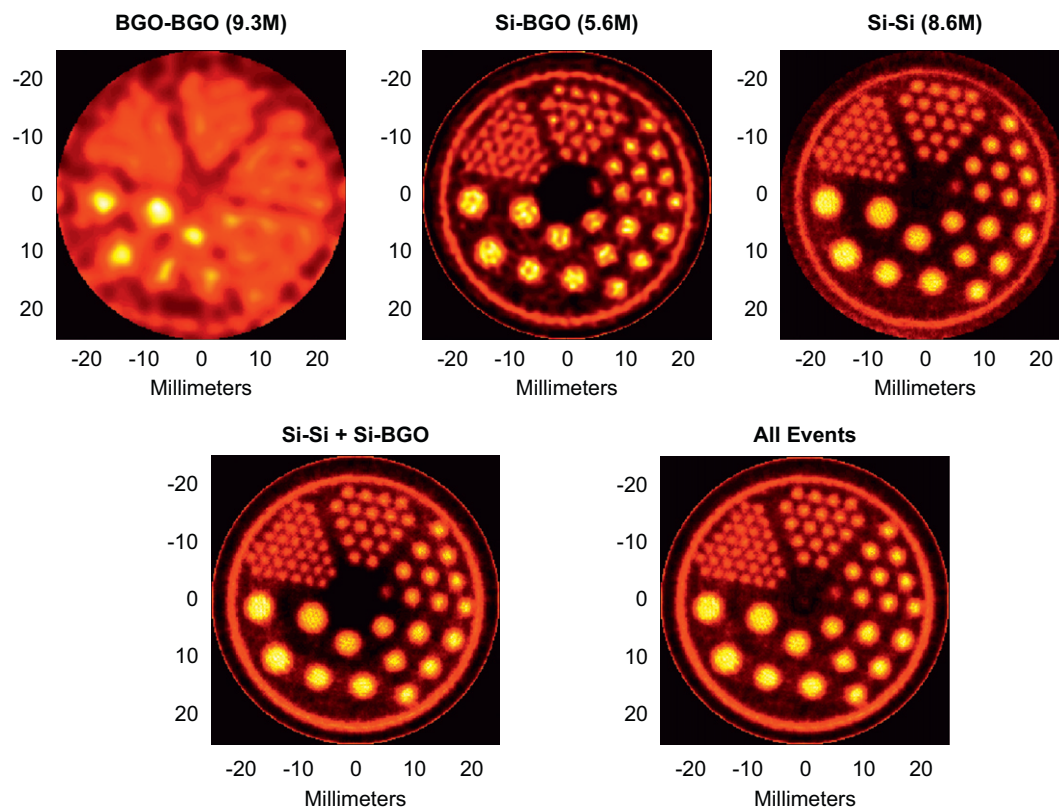


Fig. 3. Single-slice reconstructions. Top row: reconstructions from BGO–BGO, Si–BGO, and Si–Si coincidences alone (reconstructed using 1000, 400, and 100 iterations, respectively, using the ML-EM method noted in the text). Bottom row: reconstructions from combined Si–Si and Si–BGO events (left, 400 iterations) and all events (right, 1000 iterations).

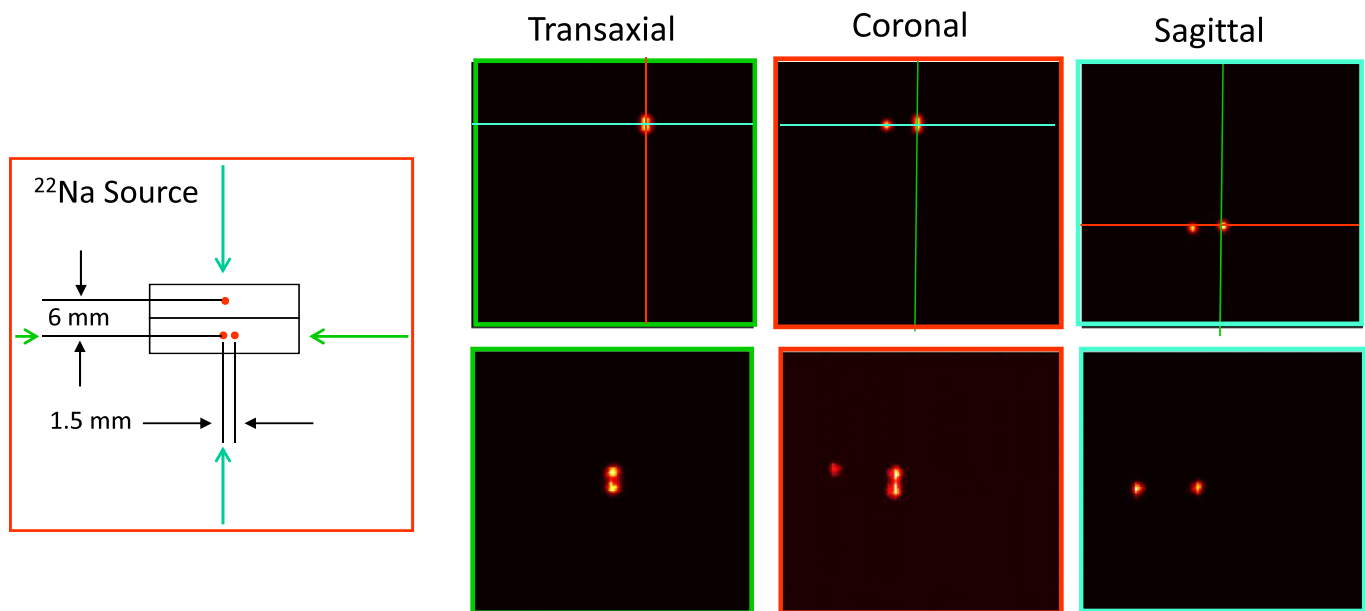


Fig. 4. Left: drawing of ^{22}Na source used for images at right with locations of transaxial (green), coronal (red), and sagittal (blue) planes shown. Right, top row: transaxial, coronal and sagittal planes from volume reconstruction of Si–BGO events. Sources separated by 6 mm are clearly resolved while those separated by 1.5 mm are not. Bottom row: reconstructions in similar orthogonal planes from Si–Si events. As expected, all sources are resolved. Field-of-view size is 5 cm (top row) and 2.5 cm (bottom row). (For interpretation of the references to color in this figure caption, the reader is referred to the web version of this article.)

resolution is a primary goal. In this context, it may find use in high-resolution preclinical PET for studying mechanisms of human disease with small animal models or in high-resolution imaging probes that can be used to augment conventional PET for human

subjects. To test these concepts, we developed a reconfigurable “dual-ring” instrument consisting of a partial outer ring of conventional PET detectors at large radius supplemented by a partial inner ring of silicon. Both single-slice and volume PET geometries were

evaluated as well as the ability of the image reconstruction to combine the three classes of “interesting” coincidences.

While silicon warrants further investigation for high resolution PET, there are numerous challenges. The most significant at this point appear to be (1) dense packaging, (2) reading out high granularity detectors, and (3) coincidence timing. As an example, a tomograph with good efficiency can be constructed by locating $\sim 150 \text{ cm}^3$ of silicon around a 4 cm diameter \times 4 cm long FOV. Reading out the silicon at a granularity of 1 mm^3 requires 150 K separate positions (each associated with one channel of electronics in the current configuration). Moreover, at typical PET event rates, the desired timing resolution should be on the order of 10 ns FWHM or less to keep random coincidences low; however, present implementations are far from that figure. It is likely that these issues can be eventually resolved but significant work remains.

References

- [1] A. Del Guerra, N. Belcari, Nuclear Instruments and Methods in Physics Research in Section A 583 (2007) 119.
- [2] C.S. Levin, H. Zaidi, PET Clinics 2 (2007) 125.
- [3] S. Park, W.L. Rogers, S. Huh, H. Kagan, K. Honscheid, D. Burdette, E. Chesi, C. Lacasta, G. Llosá, M. Mikuž, A. Studen, P. Weilhammer, N.H. Clinthorne, Nuclear Instruments and Methods in Physics Research in Section A 570 (2007) 543.
- [4] G. Di Domenico, G. Zavattini, N. Cesca, N. Auricchio, R. Andritschke, F. Schopper, G. Kanbach, Nuclear Instruments and Methods in Physics Research in Section A 571 (2007) 22.
- [5] S. Park, W.L. Rogers, N.H. Clinthorne, IEEE Transactions on Nuclear Science NS-54 (5) (2007) 1543.
- [6] S. Park, W.L. Rogers, N.H. Clinthorne, Physics in Medicine and Biology 52 (2007) 4653.
- [7] D. Burdette, D. Albani, E. Chesi, N.H. Clinthorne, E. Cochran, K. Honscheid, S.S. Huh, H. Kagan, M. Knopp, C. Lacasta, M. Mikuž, P. Schmallbrock, A. Studen, P. Weilhammer, Nuclear Instruments and Methods in Physics Research in Section A 609 (2009) 263.
- [8] A. Studen, E. Chesi, V. Cindro, N.H. Clinthorne, E. Cochran, B. Grošičar, K. Honscheid, H. Kagan, C. Lacasta, G. Llosá, V. Linhart, M. Mikuž, V. Stankova, P. Weilhammer, D. Žontar, Nuclear Instruments and Methods in Physics Research in Section A 648 (2011) S255.
- [9] N.H. Clinthorne, S. Park, W.L. Rogers, P. Chiao, in: IEEE Nuclear Science Symposium Conference Record, 2003, pp. 1997–2001.
- [10] D. Meier, A. Czermak, P. Jalocha, B. Sowicki, M. Kowal, W. Dulinski, G. Mæhlum, E. Nygård, K. Yoshioka, J. Fuster, C. Lacasta, M. Mikuž, S. Roe, P. Weilhammer, C. Hua, S. Park, S.J. Wilderman, L. Zhang, N.H. Clinthorne, W.L. Rogers, IEEE Transactions on Nuclear Science NS-49 (3) (2002) 812.
- [11] A. Studen, D. Burdette, E. Chesi, V. Cindro, N.H. Clinthorne, E. Cochran, B. Grošičar, H. Kagan, C. Lacasta, V. Linhart, M. Mikuž, V. Stankova, P. Weilhammer, D. Žontar, Radiation Protection Dosimetry 139 (1–3) (2010) 199.

TIPP 2011 – Technology and Instrumentation in Particle Physics 2011

A high-resolution PET demonstrator using a silicon “magnifying glass”

Neal Clinthorne^{a*}, Eric Cochran^b, Enrico Chesi^c, Milan Grkovski^d, Borut Grošičar^d, Klaus Honscheid^b, Sam S. Huh^a, Harris Kagan^b, Carlos Lacasta^e, Karol Brzezinski^e, Vladimir Linhart^e, Marko Mikuž^d, D. Shane Smith^b, Vera Stankova^e, Andrej Studen^d, Peter Weilhammer^e, Dejan Žontar^d

^a*Nuclear Medicine and Molecular Imaging, University of Michigan, Ann Arbor, MI 48109-5610 USA*

^b*Department of Physics, Ohio State University, Columbus, OH USA,*

^c*CERN, Geneva, Switzerland*

^d*Jozef Stefan Institute, Ljubljana, Slovenia*

^e*IFIC / CSIC University of Valencia, Valencia, Spain*

Abstract

To assist ongoing investigations of the limits of the tradeoff between spatial resolution and noise in PET imaging, several PET instruments based on silicon-pad detectors have been developed. The latest is a segment of a dual-ring device to demonstrate that excellent reconstructed image resolution can be achieved with a scanner that uses high-resolution detectors placed close to the object of interest or surrounding a small field-of-view in combination with detectors having modest resolution at larger radius. The outer ring of our demonstrator comprises conventional BGO block detectors scavenged from a clinical PET scanner and located at a 500mm radius around a 50mm diameter field-of-view. The inner detector—in contrast to the high-Z scintillator typically used in PET—is based on silicon-pad detectors located at 70mm nominal radius. Each silicon detector has 512 1.4mm x 1.4mm x 1mm detector elements in a 16 x 32 array and is read out using VATA GP7 ASICs (Gamma Medica-Ideas, Northridge, CA). Even though virtually all interactions of 511 keV annihilation photons in silicon are Compton-scatter, both high spatial resolution and reasonable sensitivity appears possible. The system has demonstrated resolution of ~0.7mm FWHM with Na-22 for coincidences having the highest intrinsic resolution (silicon-silicon) and 5–6mm FWHM for the lowest resolution BGO-BGO coincidences. Spatial resolution for images reconstructed from the mixed silicon-BGO coincidences is ~1.5mm FWHM demonstrating the “magnifying-glass” concept.

© 2012 Published by Elsevier B.V. Selection and/or peer review under responsibility of the organizing committee for TIPP 11.

Keywords: PET; silicon detectors; high-resolution imaging; magnifying PET

* Corresponding author. Tel.: +1 734 764-4289; fax: +1 734 764-0288.

E-mail address: nclintho@umich.edu.

1. Introduction

Positron emission tomography or PET is a widely employed imaging method in medicine and biomedical research [1]. Briefly, the subject is injected with a radiolabeled tracer that localizes according to specific metabolic pathways. Upon decay, the radionuclide emits a positron that annihilates with a nearby electron releasing two 511 keV photons traveling in nearly opposite directions. Detection of these photons in time-coincidence localizes the annihilation to a line-of-response (LOR) and from a collection of $10^7 - 10^8$ such events, the 3D distribution of radiotracer can be reconstructed.

Magnifying PET geometries—where a detector having high spatial resolution located close to a region of interest works in coincidence with a conventional PET detector having more modest resolution—have been investigated in a number of studies spanning the past decade. Clinthorne and Park proposed instruments for small animal and patient imaging based on high-resolution detectors used in conjunction with standard PET detectors [2–5]. Tai and co-workers have referred to the concept as “virtual pinhole PET” and have developed several demonstration instruments [6–8]. Huh, et al, have evaluated the concept of an endorectal insert for high resolution prostate imaging and are presently developing a LYSO/silicon photomultiplier based instrument [9]. The goal of the MADEIRA project is to develop a high-resolution add-on probe for clinical PET [10]. More recently, Zhou and co-workers have termed the concept “zoom-in” PET and have investigated the advantage of augmenting conventionally acquired PET data with information from a higher resolution detector [11,12].

To explore potential performance advantages of magnifying geometries for PET applications ranging from small animal imaging to organ-specific high resolution imaging probes for human subjects, we have constructed a demonstration instrument consisting of a partial outer ring of conventional PET detectors supplemented by a partial inner ring of high-resolution silicon detectors. This paper describes the basic principles, construction, and initial images obtained from the device.

2. Principles and Design

2.1. Magnifying PET geometry

The principles of a magnifying geometry are discussed by Park, et al. [5]. We restrict the following discussion to geometries in which a full ring of high resolution detectors (or emulation thereof) surrounds a small field-of-view. This high resolution detector ring is itself inserted into the larger diameter bore of a conventional PET instrument. Since the inner detector may not have high detection efficiency for 511 keV photons, there are three significant classes of PET coincidence events that can be reconstructed: (1) those in which both annihilation photons interact in the high resolution detector ring (referred to as Si-Si here); (2) those in which both photons are detected in the outer, low-resolution ring (BGO-BGO); (3) and hybrid events (Si-BGO) where one event interacts in the high resolution ring and the other in the low

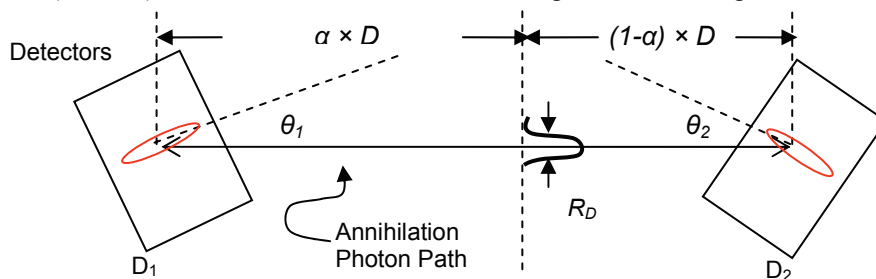


Fig. 1. Diagram illustrating detector geometry and parameters used for approximating intrinsic resolution in Equation (1).

resolution ring. That the Si-Si and BGO-BGO events result in the highest and lowest resolution data, respectively, is clear. The spatial uncertainty of the Si-BGO events, however, varies significantly along the coincidence LOR between the high- and low-resolution detectors as described next.

2.2. Intrinsic spatial resolution in a magnifying geometry

Intrinsic resolution is dominated by the detector (either high- or low-resolution) to which the positron source is physically closest. Thus, resolution in a small FOV surrounded by high-resolution detectors will be dominated by the performance of that detector as shown through the following expression:

$$R_D \approx 2.35 \sqrt{\left((1-\alpha)^2 (\sin^2 \theta_1 \sigma_{D1}^2 + \cos^2 \theta_1 \sigma_{C1}^2) + \alpha^2 (\sin^2 \theta_2 \sigma_{D2}^2 + \cos^2 \theta_2 \sigma_{C2}^2) \right)} \quad (1)$$

where σ_C and σ_D are the standard deviations in estimating position in each detector in the circumferential or transverse and depth directions, respectively, α is the fractional distance of the source along a coincidence LOR intersecting the two detectors at the angles of incidence shown in Fig. 1. Note that the expression conveniently accounts for depth-of-interaction uncertainty that often degrades resolution at large angles of incidence. Eq. (1) is derived by calculating the covariance of a point along the mean LOR at distance $\alpha \times D$ from D_1 given the position variance in the LOR endpoints. Element (1,1) of this matrix quantifies the variation transverse to the LOR at that location. To obtain the combined resolution, uncertainty due to acolinearity of the annihilation radiation, which can be quantified as $0.0088 \times (\alpha - \alpha^2) \times D$ millimeters (where D is also in millimeters), adds in quadrature to the resolution in eq. (1).

As an example, assuming normal incidence on both detectors, the intrinsic resolution for a source 3cm from a detector having 1mm FWHM resolution and 40cm from a detector having 6mm FWHM resolution would be 1.1mm FWHM including the effects of acolinearity of the annihilation radiation in soft-tissue. At 10cm from the higher resolution detector, this decreases to 1.7mm FWHM.

2.3. Tradeoff between reconstructed resolution and noise

Although intrinsic measurement uncertainty plays a significant role in overall system performance, spatial resolution in the reconstructed image can actually be better than that suggested by the intrinsic resolution if the system aperture function is appropriately modeled in the reconstruction process [1]. Such *resolution recovery*, however, increases the noise level or variance in reconstructed images. This increase is highly non-linear as a function of reconstructed resolution as shown in Fig. 2(a) where the

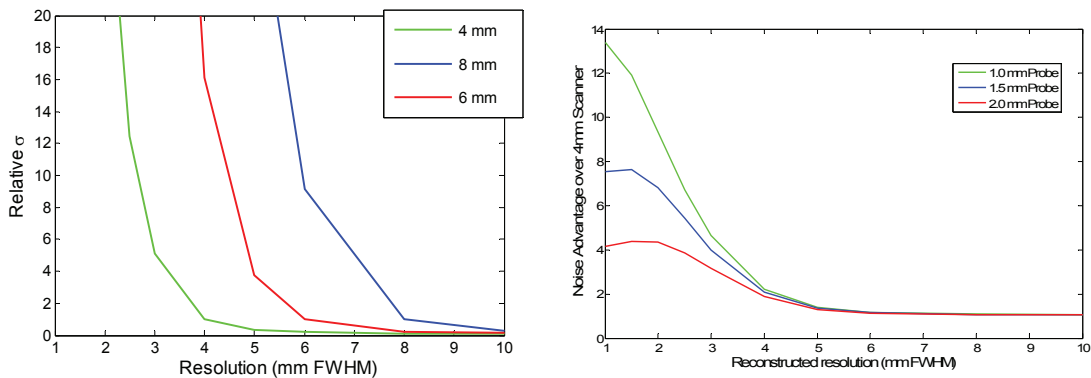


Fig. 2. (a) Standard deviation vs. reconstructed image resolution for detectors supporting intrinsic resolution of 4mm, 6mm, and 8mm FWHM. Standard deviation has been normalized to unity for reconstructed resolution equal to the intrinsic resolution. (b) Noise advantage as a function of reconstructed image resolution for an additional 12% of data having intrinsic resolutions of 1.0mm, 1.5mm, and 2.0mm FWHM added to 4mm FWHM data.

approximate standard deviation at the center of a uniformly emitting disk source occupying the full FOV is plotted against desired spatial resolution in reconstructed images for simulated PET systems having Gaussian resolutions of 4mm, 6mm, and 8mm FWHM (curves were calculated using the modified uniform Cramér-Rao bound, which is applicable to SPECT and PET imaging systems [13, 16]). Each curve has been normalized to unity at the intrinsic resolution of the simulated scanner. Note how quickly noise increases as one attempts to operate at points better than the intrinsic resolution. As an example, operating the 4mm system at 3mm FWHM reconstructed resolution increases the standard deviation by a factor of 10. To achieve the same noise level as a reconstruction with 4mm FWHM resolution, 100× the number of events would need to be collected.

Fig. 2(b) demonstrates the effect of adding a small amount (12%) of additional data having resolutions of 1mm, 1.5mm, and 2mm FWHM to PET data from a system having 4mm intrinsic resolution. Curves shown are the standard deviation of reconstructions from the combined datasets divided by that of the 4mm dataset alone and are plotted against desired reconstructed resolution. At operating points above 4mm FWHM, there is little advantage to including information from a high resolution detector while there is a considerable performance improvement at operating points *better* than 4mm FWHM. And as expected, the advantage increases for detectors having higher resolution.

2.4. Silicon as an unconventional PET detector

The previous section demonstrates that adding a modest amount of data having high intrinsic resolution to lower resolution data can have a significant impact on performance. In a conventional PET scanner, detectors typically comprise high-density scintillators such as BGO or LYSO read out by photodetectors. It remains challenging to achieve submillimeter spatial resolution with this approach as well as appropriate depth of interaction resolution (i.e., 3D position resolution). Solid-state detectors based on silicon, however, can readily achieve submillimeter performance in 3D. Even though attenuation length of silicon for 511 keV photons is 5cm as opposed to 1cm for BGO and 1.1cm for LYSO, information in the previous section demonstrates that silicon may well outperform the more conventional scintillation detectors when the goal is resolution in the neighborhood of 1mm FWHM.

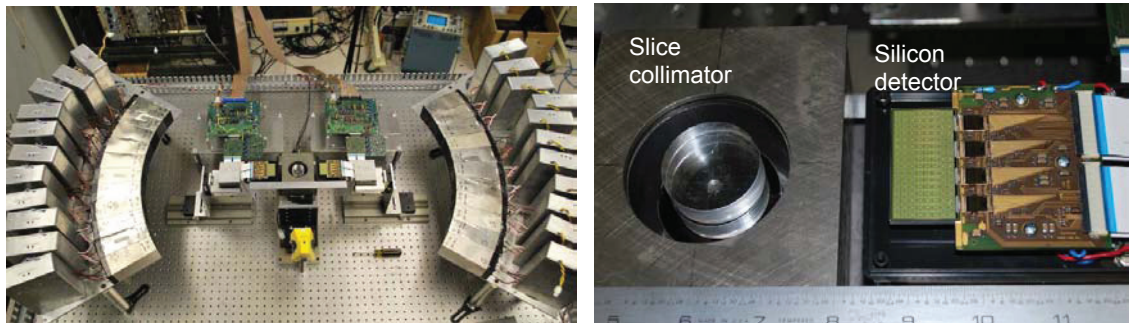


Fig. 3. (a) Dual partial-ring PET demonstrator showing BGO block detectors at 500mm radius and silicon pad detectors at ~70 mm radius surrounding 45mm diameter field-of-view. Full PET dataset is acquired by rotating object. (b) Close-up showing edgewise positioning of 1mm thick silicon pad detector, object turntable and tungsten slice collimator.

3. Demonstrator Design

To evaluate the use of silicon as a PET detector for the primary purpose of rodent imaging within a 50mm FOV, we have assembled the demonstration instrument shown in Fig. 3(a). The instrument consists of a partial ring of 24 BGO detectors at 500mm radius within which a partial “ring” of silicon pad detectors at nominal radius 70mm has been inserted. To reduce the overall event rate on the detectors, the source has been collimated to a 1mm thick slice using tungsten plates and the silicon detectors have been located on edge as shown in Fig. 3(b) to achieve high detection efficiency for the slice. A full set of PET data is acquired by rotating the object in 6° steps and recording Si-Si, Si-BGO, and BGO-BGO coincidences. Raw coincidence information is recorded in a structured list containing position and energy as well as a time-stamp for each trigger, which allows acquired data to be post-processed to change energy thresholds or timing window widths, for example.

3.1. BGO block detectors

The 24 BGO block detectors were scavenged from a CTI 931 (ca. 1985) PET scanner and each comprises a 4x8 BGO crystal array of 6mm x 12mm crystals read out by a 2 x 2 array of 25mm square PMTs. The detectors are oriented such that the 6mm width is along the circumference of the ring. PMT outputs are routed to a simple CR-RC shaping amplifier and then to a peak-sensing ADC. Timing resolution for BGO-BGO coincidences is ~12 ns FWHM while typical energy resolution for the 511 keV peak is 20% FWHM. Although the performance of these detectors is inferior to modern LYSO (or LSO) based devices, they provide an excellent demonstration of the magnifying PET concept using Si-BGO coincidences.

3.2. Silicon pad detectors

The silicon detectors currently used in this instrument are 1mm thick and each have 512 1.4mm x 1.4mm pads arranged in a 16 x 32 array [14]. Each detector is read out by four VATAGP-7 ASICs developed for this application by Gamma Medica-Ideas [15] and a VME bus based interface. Since virtually all interactions of 511 keV photons will be Compton scattering, the triggering threshold for PET measurements was set to nominally 30 keV but varied by channel depending on inherent offset. While the ASIC has trim-DACs for each channel to allow triggering at the same energy, these were not calibrated for the measurements presented below. Energy resolution with this setup is approximately 2 keV FWHM (although this does not directly impact PET performance of the instrument). Timing resolution is relatively poor due to both time-walk of the leading-edge trigger in the ASIC, which can be corrected off-line, and variations due to 3D interaction location in the detector and uncertainty in the Compton recoil electron path. Coincidence resolution between two silicon detectors operated at 136 V bias is ~50ns FWHM. Increasing the bias and correcting the pulse-height dependent time-walk improves timing performance but was not done since the random coincidence rate was sufficiently low in the single-slice geometry.

4. Imaging Performance

4.1. Reconstructions from simulated data

To understand what to expect from reconstructions of a resolution phantom and to explore the advantages of simultaneously reconstructing a single image from all three types of coincidence events, single-slice Monte Carlo data was generated by projecting a simulated resolution phantom through the system response and then adding Poisson noise. Measurement sensitivities, detector normalizations, and intrinsic resolutions were consistent with those of the demonstrator. Specifically, 50 million total detected events were used (3% Si-Si, 14% Si-BGO, and 83% BGO-BGO) with Si-Si resolution of 0.7mm FWHM, Si-BGO resolution of 1.2mm FWHM and BGO-BGO resolution of 3.2 mm FWHM (all Gaussian shaped and based on the approximation in Section 2.2). These figures correspond to an idealized version of the demonstrator and performance of the actual system is expected to be significantly worse due primarily to significant mis-positioning in the BGO detectors and to a lesser extent inaccuracies in modeling the response of the real device.

Reconstructions from the simulated data using a regularized maximum likelihood (ML) reconstruction [16] are shown in Fig. 4 for a resolution phantom consisting of 4.8mm, 4.0mm, 3.2mm, 2.4mm, 1.6mm and 1.2mm diameter rods separated by two rod diameters center-to-center. The top row shows images reconstructed from the individual coincidence events (Si-Si–100 iterations, Si-BGO–500 iterations, and BGO-BGO–1000 iterations). Performance is as expected with the Si-Si events demonstrating the best resolution (and spot-shape fidelity) but also the highest noise. BGO-BGO resolution is the worst and the reconstruction also shows aliasing for the wedges containing the three smallest diameter spots due to undersampling. Reconstructions from the Si-BGO events greatly improve upon this with resolution closer to that of the Si-Si reconstruction. Note, however, that the smaller spots in the Si-BGO and BGO-

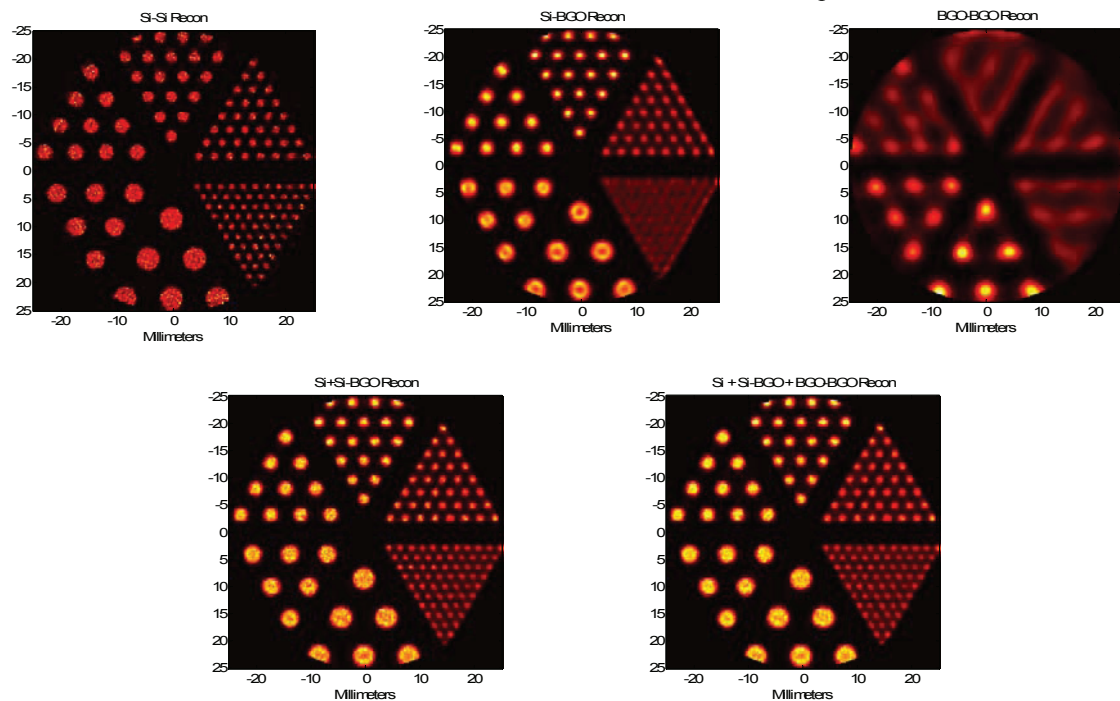


Fig. 4. Top row left-to-right: Si-Si reconstruction from simulated data, Si-BGO reconstruction, BGO-BGO reconstruction. Note noise in Si-Si reconstruction as well as distortion of spot shapes in Si-BGO and BGO-BGO reconstructions. Bottom row: composite reconstructions using Si-Si and Si-BGO data (left) and all events (right).

BGO reconstructions tend to be overly sharp with diameters smaller than actual and that the larger spots in the Si-BGO reconstructions suffer from edge overshoot.

The image at the bottom left in Fig. 4 combines both Si-Si and Si-BGO events (500 iterations). Resolution is improved over the reconstruction from Si-BGO events alone and noise is reduced over using only Si-Si events. Moreover, the spot shape has better fidelity. As predicted in [16], adding the lowest resolution BGO-BGO events adds little, if anything, to overall performance and slows convergence of the iterative ML reconstruction (1000 iterations).

4.2. Reconstructions from demonstrator measurements

For data acquisition using the demonstrator, the silicon threshold was set to ~ 30 keV, the BGO energy window from 300–700 keV, and the Si-Si, Si-BGO, and BGO-BGO timing windows to 425ns, 230ns, and 25ns, respectively. Since virtually all interactions of 511 keV photons are Compton scatter in the silicon, the energy of a valid event ranges from the 30 keV threshold through ~ 340 keV. Due to both the small FOV and the single-slice geometry, the rate of detected events resulting from Compton-scatter in the object is low although this warrants additional investigation for geometries lacking such collimation. Presently, wide timing windows are needed to accommodate time-walk associated with the large range of silicon pulse-heights. In a system capable of operating at counting rates necessary for small animal imaging, the wide windows will lead to an unacceptable random coincidence rate. Improved time resolution for silicon, however, is under active investigation in our laboratory. Typical random

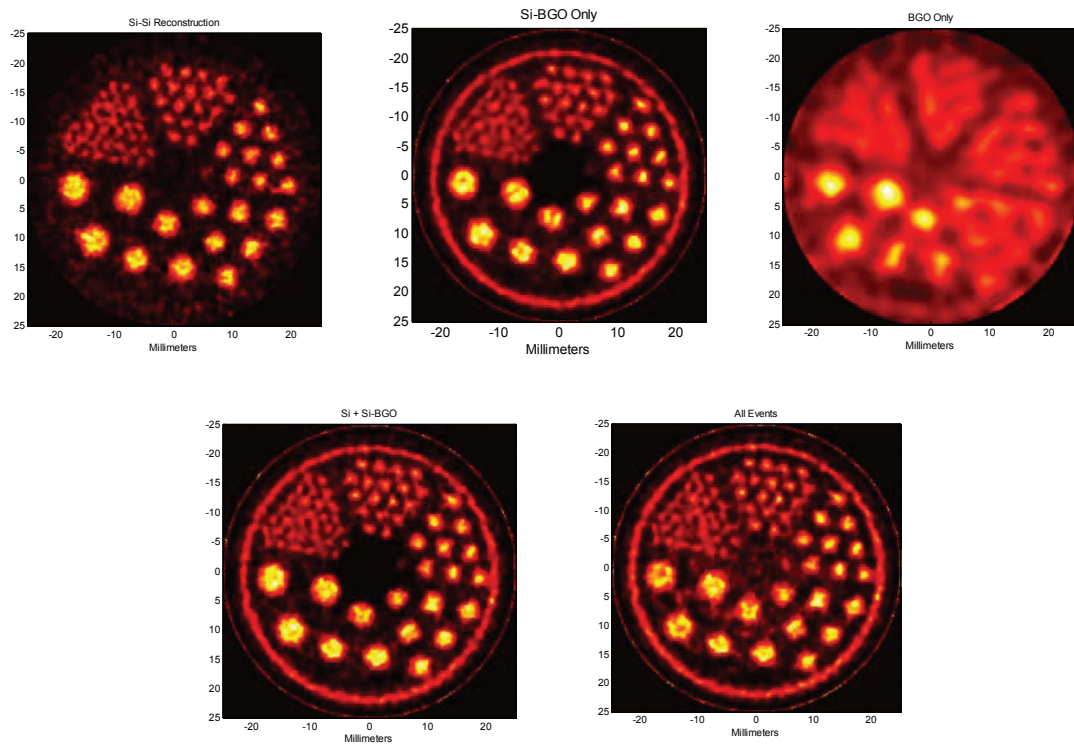


Fig. 5. Reconstructions from data measured with the demonstrator shown in Fig. 3. Top row left-to-right: reconstructions of a micro-Jaszczak resolution phantom from Si-Si, Si-BGO, and BGO-BGO events alone. Bottom row left: reconstruction from Si-Si and Si-BGO events. Bottom right: reconstruction using all events.

coincidences in this geometry for Si-Si events were <5% of the total for the resolution phantom studies. Detector normalization factors were calculated using both measurements and modeling for each coincidence event class. Calculated object attenuation was included in the normalization.

Fig. 5 shows images reconstructed from micro-Jaszczak resolution phantom measurements acquired using the demonstration instrument using ~185 MBq of ^{18}F -fluorodeoxyglucose (FDG) over an interval of 5 hours. Rod sizes in the resolution phantom are the same as for the simulation in the previous section (4.8mm, 4.0mm, 3.2mm, 2.4mm, 1.6mm, and 1.2mm) and the order is the same as for the reconstructions shown in Fig. 4 (Si-Si–40 iterations, Si-BGO–200 iterations, BGO-BGO–1000 iterations). In this case, Si-Si events comprise 3.4%, Si-BGO 20.5%, and BGO-BGO 76.1% of the 1.2×10^7 collected coincidences. For reconstruction, the same system model for reconstructing the simulated data in Fig. 5 was used (responses of 0.7mm, 1.2mm, and 3.2mm FWHM for Si-Si, Si-BGO, and BGO-BGO events, respectively). The hot ring around the resolution phantom is real and not visualized in the Si-Si reconstruction due to the slightly smaller FOV size (45 mm vs. 50mm diameter). Trends in these reconstructions correspond to those in Fig. 4 with the exception that the Si-Si reconstruction is significantly noisier due to fewer coincidence events. Composite reconstructions are shown in the bottom row using 200 iterations for Si-Si+Si-BGO (left image) and 1000 iterations for all events (right). While reconstruction from Si-Si and Si-BGO events is perhaps slightly better than either reconstruction alone (the outer ring is correctly reconstructed and the blurring slightly less for the smallest diameter spots), reconstruction from all events reduces performance somewhat. This is due both to a significantly slower convergence rate for the combined data and to inaccuracies in modeling the actual response of the BGO-BGO events. If modeling is consistent, there is no reason that including the lowest resolution events should decrease performance. Nevertheless, when the desired operating point is at a resolution much higher than the intrinsic resolution of the BGO-BGO events, one will lose little performance by disregarding them as shown in Fig. 4.

5. Conclusions

To assist in our ongoing investigation of high resolution PET in magnifying geometries we have constructed a demonstration instrument consisting of low resolution BGO detectors and high resolution silicon pad detectors. Preliminary reconstructions of resolution phantom data acquired using the device were presented and performance qualitatively agreed with Monte Carlo simulations from an idealized system. In the coming months, this instrument will be used to evaluate a number of high-resolution PET imaging configurations including those applicable to small animals as well as probes for prostate and head-and-neck imaging in human subjects.

Acknowledgement

We acknowledge support from the US Department of Health and Human Services under NIH grant R01 EB430-37, the US Army Congressionally Directed Medical Research Program under grant W81XWH-09-1-0413, and the European Commission under Framework Programme 7 EURATOM-FISSION grant 212100 (Acronym: MADEIRA).

References

- [1] Wernick M, Aarsvold J (eds). *Emission tomography: the fundamentals of PET and SPECT*. New York: Elsevier Academic Press; 2004.
- [2] Clinthorne NH, Meier D, Hua C, et al. Very high resolution animal PET (abs). *J Nucl Med Supp* 2000; **41**:20P.
- [3] Park SJ, Rogers WL, Wilderman SJ, et al. Design of a very high resolution animal PET (abs). *J Nucl Med Supp* 2001; **42**:55P.
- [4] Clinthorne NH, Park SJ, Wilderman SJ, et al. High resolution PET detector (abs). *J Nucl Med Supp* 2001; **42**:102P.
- [5] Park SJ, Rogers WL, Clinthorne NH: Design of a very high resolution small animal PET scanner using a silicon scatter detector insert. *Phys Med Biol* 2007; **52**:4653–77.
- [6] Tai YC, Wu H, Pal D, et al. Virtual pinhole PET. *J Nucl Med* 2008; **49**:471–9.
- [7] Wu H, Pal D, Song TY, et al. Micro Insert: A Prototype Full-Ring PET Device for Improving the Image Resolution of a Small-Animal PET Scanner. *J Nucl Med* 2008; **49**:1668–76.
- [8] Wu, H, Pal D, O'Sullivan, et al. A Feasibility Study of a Prototype PET Insert Device to Convert a General-Purpose Animal PET Scanner to Higher Resolution. *J Nucl Med* 2008; **49**:79–87.
- [9] Huh SS, Clinthorne NH, Rogers WL: Investigation of an internal PET probe for prostate imaging. *Nucl Ins Met Phys Res A* 2006; **579**:339–343.
- [10] Studen A, Chesi E, Cindro V, et al. Report on the MADEIRA PET probe. *Nuclear Science Symposium Conference Record, 2010 IEEE*. 2010; p. 1755–8.
- [11] Zhou J, Qi J. Theoretical analysis and simulation study of a high-resolution zoom-in PET system. *Phys Med Biol* 2009; **54**:5193–208.
- [12] Zhou J, Qi J. Adaptive imaging for lesion detection using a zoom-in PET system. *IEEE Trans Med Imag* 2011; **30**:119–130.
- [13] Meng LJ, Clinthorne NH. A modified uniform Cramer-Rao bound for multiple pinhole aperture design. *IEEE Trans Med Imag* 2004; **23**:896–902.
- [14] Meier D, Czermak A, Jalocha P, et al. Silicon detector for a Compton camera in nuclear medical imaging. *IEEE Trans Nucl Sci* 2002; **49**:812–16.
- [15] Linhart V, Burdette D, Chessi E, et al. Spectroscopy study of imaging devices based on silicon pixel array detector coupled to VATAGP7 readout chips. *J Inst* 2011, doi:10.1088/1748-0221/6/01/C01092.
- [16] Clinthorne NH, Park SJ, Rogers WL, et al. Multi-resolution image reconstruction for a high-resolution small animal PET device. *Nuclear Science Symposium Conference Record, 2003 IEEE*. 2003; p. 1997–2001.

High Resolution Fast Stereotactic PET Imager for Prostate Biopsy

S. Majewski, A. Stolin, E. Delfino, P. Martone, Center for Advanced Imaging, West Virginia University, Morgantown, WV
J. Proffitt, AiT Instruments, Newport News, VA

We are developing a dedicated high resolution (sub-mm), high efficiency, and very fast (with live reconstruction) prostate PET imager composed of an endorectal PET probe and two PET panel modules placed close to the patient on the opposite side of the prostate, and operating in coincidence with the probe. The immediate live image feedback will be primarily useful in biopsy guidance. PET images will be co-registered with the images from the Transrectal Ultrasound (TRUS) probe that will provide the usual structural 2D or 3D information, while the PET imager will provide the metabolic information related to the biological state of the prostate. We are reporting on preliminary data acquired with the prototype imager. The major highlight is that we are achieving ~1mm FWHM DOI resolution with the PET probe, using new monolithic MPPC arrays from Hamamatsu. But even with a non-DOI probe, we obtained good performance in this limited angle tomography problem.

I. INTRODUCTION

In order to image molecular activity in the prostate associated with prostate cancer, especially at the early stages of the disease, one needs: (1) imaging agents specific for prostate cancer, (2) better molecular imaging tools offering higher specificity, resolution and sensitivity.

Standard Positron Emission Tomography (PET) scanners (used in combination with X-Ray Computed Tomography - CT) have spatial resolutions (~6-8mm) not adapted to imaging small (~1mm) suspicious lesions in the prostate. We are developing prostate-specific high spatial resolution (~1mm) PET systems allowing for early detection, visualization, and biopsy guidance of the cancerous lesions. We are also working on hybrid combinations of these PET systems with ultrasound probes, including the tissue-differentiating variants, using elastography and other new approaches. The key element for all these systems is the high resolution compact PET probe inserted endorectally with or without the ultrasound probe (TRUS or other variants).

One of the systems that we are developing is a high resolution (sub-mm), high efficiency, and very fast (with live reconstruction) prostate PET imager composed of an endorectal PET probe placed close to the prostate and two PET panel modules placed stereotactically and close to the patient body. The panels are positioned on the opposite sides of the prostate, and operate in coincidence with the PET probe. The live image feedback will be primarily useful in biopsy guidance. PET images will be co-registered with the images from the Transrectal Ultrasound (TRUS) probe

that will provide the usual structural 2D or 3D information, while the PET imager will provide the metabolic information related to the biological state of the prostate.

II. METHODS

Conceptual design of stereotactical prostate scanner is shown in Fig.1.

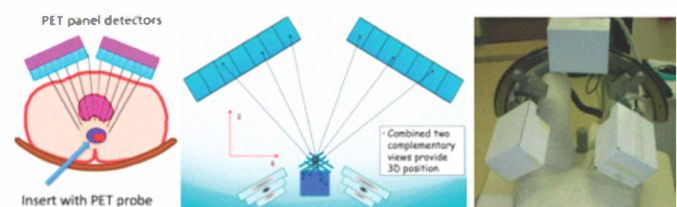
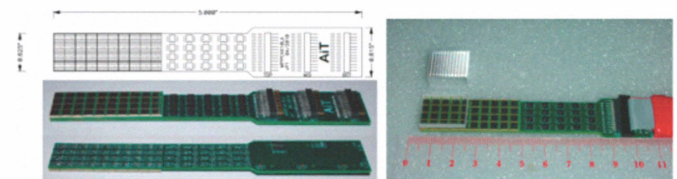


Fig.1. Concept of the dedicated PET prostate imager composed of the endorectal PET probe and two PET panel imaging modules providing two instant reconstruction (laminography) and simultaneous stereotactic views of the region of the prostate. For the range of impinging angles expected in the prostate probe the net effect of limited DOI resolution should be kept under 1mm. The prototype WVU system shown at right with two 10cm FOV panel modules mounted on a gantry.

There were two variants of endorectal prepared for the system, Fig.2 and 3. First prototype of non-DOI detector was constructed by arranging individual 3 mm MPPCs into a 4 by 10 array. This array was coupled to a 1.5 x 1.5 mm LYSO pixel matrix. Detector electronics was placed in the region close to the imaging array. The detector assembly was packaged into a light-tight enclosure.



The non-DOI Compact low-profile prostate PET probe built by AiT Instruments, based on an array of 4x10 MPPC 3mm SiPMs from Hamamatsu, with ~ 15mm x 45mm active FOV.

Resulting detector underwent characterization tests in order to determine its basic imaging properties. Pixel separation, energy resolution and uniformity of response were of most interest.

Another variant of the probe was based on 4 x 4 monolithic MPPC array from Hamamatsu. Each MPPC is a 3 mm square for a total detector size of 12.5 mm. Custom made LYSO crystal array with two open

surfaces and rough treatment of the crystal edges was used. Array had a pixel pitch of 0.7 mm with crystal length of 10 mm. Data from both sides of the array was combined for both crystal identification and DOI calculations. Tests similar to those of the previous probe were performed.

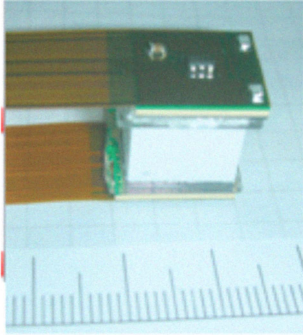


Fig.3. Photograph of DOI-capable high-resolution PET probe. The sub-mm DOI PET probe. Left: 0.7mm step x 10mm thick 18x18 pixel LYSO DOI array from Proteus with double sided output and S10943-3344MF-050 MPPC array from Hamamatsu. The LYSO array was optimized for the DOI operation.

A prototype of a ~10 cm FOV panel detector equipped with a 1.5mm pitch and 10mm thick LYSO array, see Fig.4.

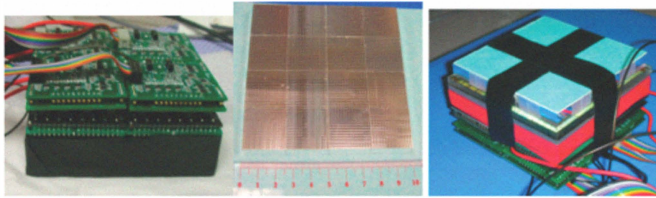


Fig.4. Photograph of panel detector prototype during various stages of assembly.

The LYSO array was built from 16 LYSO tiles, each with 24 mm x 24 mm active FOV. Scintillator array was coupled to a 2x2 array of flat panel H8500 PMTs to form detector surface with overall coverage of 96 mm x 96 mm. Between the scintillator array and the PMTs a 4.5 mm thick acrylic plate was inserted to provide better scintillation light spreading between the 6mm PMT anode pads. Optical coupling (two component Sylgard 3-6636 Silicone) was used between all optical surfaces. Raw image shows structure due to the structure of the scintillation array made of 16 tiles. Scintillation light from all 64x64 LYSO pixels was recorded in the PMT array, resulting in a continuous 96mm x96 mm FOV with no gaps.

The novel high resolution PET module based on a H8500 PMT, and a tapered custom-made compact (5.3 mm thick) light guide that connects the 57.3 mm square Proteus/Agile LYSO array of 1.51 mm x 1.51 mm x 15 mm pixels to a 48 mm x 48 mm active surface of the PMT. This permits tight assembly of 2x2 such modules to form extended and uniform high-resolution 10cm FOV detector surface, without dead regions. Each

PSPMT will be equipped with a gain-equalization resistor matrix and a read-out board that houses preamplifiers and 4-channel multiplexed analog signals [1][2][3]. A total of $4 \times 4 = 16$ ADC channels [4][5] will be required per each panel imager, and a total of 32 channels for the two panel modules. Analog data was digitized using in-house FPGA-based data acquisition system and analyzed using Kmax scientific software package.

During the final phase of scanner construction the panels will be mounted on articulated arms attached to the bed rails. A very important part of our dedicated PET system is a motion-tracking apparatus. We are testing MicroBird EM tracking system, from Ascension Technology Corp. Three such sensors will be used for independent spatial localization of the PET probe and each PET panel. Transmitters (two) will be attached to the dedicated non-metallic patient bed produced by Agile specifically for our imaging system and will remain stationary for the entire imaging session. We have measured the spatial accuracy of MicroBird sensors within a volume of 2" x 2" x 2" (sufficient for prostate imaging and obtained accuracy (measured as deviation from the linear relationship between the real position and the measured position) in the 0.30 - 0.45 mm FWHM range. Positioning information will be time-stamped with a computer clock and supplied to the reconstruction module of the software. Prior-developed PET reconstruction methodology [6][7] will be upgraded to include motion tracking. The reconstruction module will combine annihilation gamma interaction information with the tracking system data to obtain a set of lines-of-response.

III. RESULTS

Results of basic characterization tests of both variants of endorectal imaging probes are presented in Fig. 5 through 8. First detector was equipped with both 1.5 and 1 mm pixel pitch scintillation arrays. 1 mm pitch array covered the light detector surface only partially, but nevertheless high performance of the detector was confirmed.

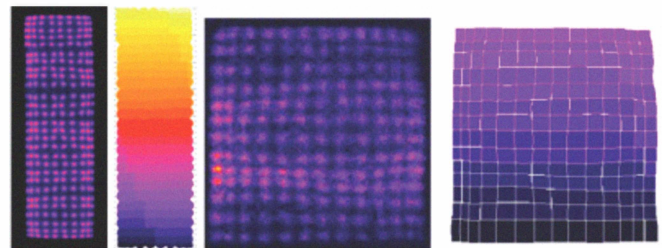


Fig.5. Raw image and the crystal map for the 14x14 1mm LYSO probe array. No MPPC gain corrections applied to images. Normalized energy resolution was measured as 20.2% @ 511 keV.

Two butted arrangements of four (2 x 2) such arrays will be used in the full size prostate PET probe. Demonstration of close placement of MPPC arrays to form a continuous detector was performed, Fig.6.

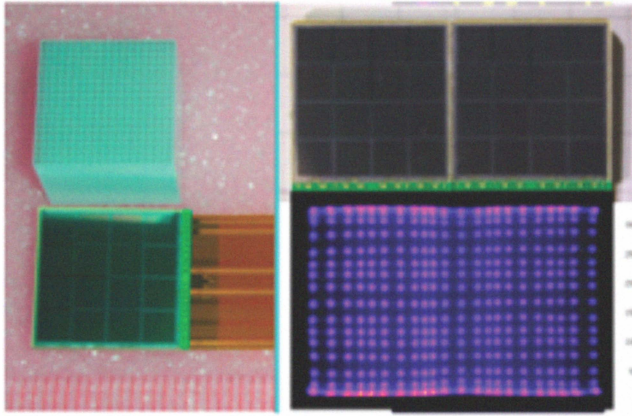


Fig.6. Test of the side-to-side butting. Raw image at left bottom shows only a small response perturbation in the junction region. Energy dropped by 15% and energy resolution changed from 11.8% to 12.1% @511 keV. Proteus LYSO array of 24x24 1.0mm x 1.0mm pitch by 10mm long pixels, optimized for one-sided output operation, and coupled to the butted MPPC array assembly using 1mm thick glass window and coupling grease. This test confirmed that signal performance deteriorates only a little in the region of the joint.

Study of temperature variation of detector gain and uniformity was performed. Results are presented in Fig.7

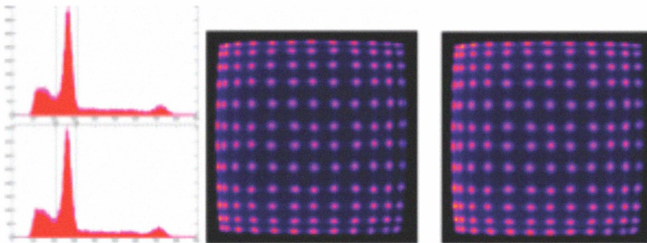


Fig.7. Gain change with voltage @ 74.4V. Examples of Na22 energy spectra obtained from individual 1mm pixels from 10cm thick array. Left: @87.7F & 73.4V; 14.4% FWHM @511 keV, right: @111.1F & 74.4V; 14.8% FWHM @ 511 keV. Examples of raw images obtained at 87.7F & 73.4V (left) and at 111.1F & 74.4V (center) obtained with 1mm LYSO array and ^{22}Na source.

DOI detector performance was characterized using comparison between detector responses under wide irradiation beam and collimated source conditions. Fig. 8 also exhibits detector line response function in the dimension perpendicular to MPPCs plane. Full width at half maximum of the LSF is taken as detector DOI resolution. It is shown to be less than 1 mm.

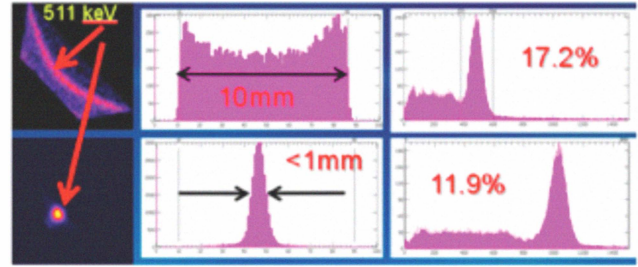


Fig.8. On the left, the 2D plots display the signal relationship between top and bottom MPPC array outputs for the broad beam (top) and narrow collimated beam (produced with electronic collimation of a 1mm ^{22}Na button source) (bottom). Single LYSO pixel selected. These pilot DOI results show < 1mm FWHM DOI resolution. The center histograms show the ratio of the signal from the top MPPC module by the sum of the signals from both modules, for a broad 511 KeV gamma beam (top), and the narrow collimated beam (bottom), respectively. At right the energy spectra for the same selected LYSO pixel and the narrow beam case are shown, for the top MPPC array (17.2% FWHM @511 keV, top spectrum) and for the sum of the two MPPC array signals (11.9% FWHM @511 keV, bottom histogram).

Imaging performance of the prototype flat panel detector is presented in Fig.9. Despite sub-optimal configuration of LYSO crystal assembly, all the pixels are clearly separated except at the edges due to non-uniformities of PMTs.

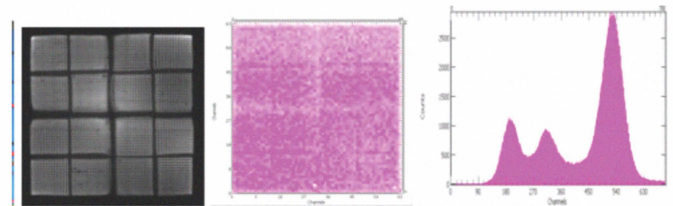


Fig.9. On the left, raw image shows structure due to the structure of the scintillation array made of 16 tiles. Scintillation light from all 64x64 LYSO pixels was recorded in the PMT array, resulting in a continuous 96mm x96 mm FOV with no gaps. Spatially and energy corrected flood image is seen in the center. Energy resolution of 13.7% @ 511 keV is measured from the normalized energy spectrum shown at right.

As described in the methods section, an improved design of flat panel detector was implemented. Raw image and a single axis projection are presented in Fig.10. As can be viewed, smudginess of the edge pixels has been eliminated with the help of fiber-optical tapered light-guide. Some local disturbance in the linearity of pixel matrix is due to small local defect in the light-guide construction. This defect does not affect overall performance, since it can be calibrated in a crystal look-up table.

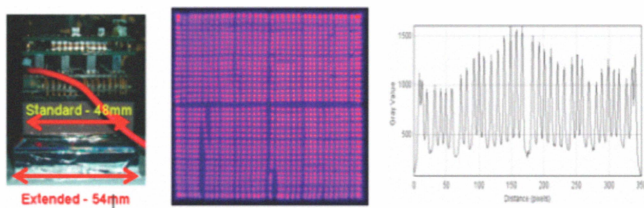


Fig.10. Photograph of an improved design of flat panel detector module is shown on the right. Resulting raw image is in the center. Projection of the image onto an X-axis is displayed on the left.

In order to demonstrate utility of the scanner several imaging experiments were performed using simple phantoms. For the first of those tests we used three narrow bore glass capillary tubes filled with ^{18}F FDG solution. Capillaries were arranged parallel to each other and placed approximately 1 cm away from the probe. Reconstructed slice is shown in Fig. 11 along with the projection.

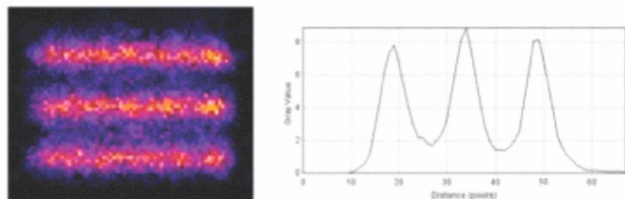


Fig.11. Left: Images obtained with a 3-capillary phantom placed $\sim 1.0\text{cm}$ from the probe. Outer/inner capillary diameter 1.25mm/0.5mm. Center-to-center spacing 3.75 mm. Right: projection taken through the image. Spatial resolution is $\sim 1.4\text{mm}$ FWHM.

Two Na-22 button sources were stacked one on top of the other as shown in Fig.12. Such a phantom was used to demonstrate an ability of stereotactic scanner to distinguish overlaying structures much like a regular full-coverage PET scanner would do.



Fig.12. Two 1mm ^{22}Na sources imbedded in the plastic shields - buttons were used to simulate the two hot spots/lesions placed close to the PET probe (at $\sim 4\text{mm}$ and $\sim 10\text{mm}$ from the probe's surface). Vertically spaced by 6.7mm, in the horizontal plane by 1.80mm. Right: Two stereotactic $\pm 15^\circ$ views of the phantom. The left view from the left panel and the probe shows only one hot spot. Both sources were (intentionally) lined up in that line of view. But the right view separates the two ^{22}Na sources. The separation of the sources in this view is about 3.5mm. The 3D spatial resolution when using both stereotactic views is better than 2mm FWHM. Some of the image blurring is due to the DOI effect in the probe. The probe used in this demonstration had only one-sided readout.

IV. CONCLUSIONS

We have successfully demonstrated prototype scanner for PET imaging of a prostate. Utility of stereotactic arrangement has been demonstrated with a simple phantom study. Most important feature of the proposed system is that the imaging feedback is received in real time, thus permitting performing biopsy using the same apparatus. Next most important item to add to the scanner will be tracking system that should be able to constantly monitor positions of flat panel detectors and the probe.

REFERENCES

- [1] V. Popov, S. Majewski, B. L. Welch, "A Novel Readout Concept for Multianode Photomultiplier Tubes with Pad Matrix Anode Layout", Nuclear Instruments and Methods in Physics Research A 567 (2006) 319-322.
- [2] V. Popov, "Matrix output device readout system", US Patent 6,747,263, 2004.
- [3] R.R. Raylman, S. Majewski, B. Kross, V. Popov, J. Proffitt, M.F. Smith, A.G. Weisenberger, R. Wojcik, "Development of a Dedicated Positron Emission Tomography System for the Detection and Biopsy of Breast Cancer", Nuclear Instruments and Methods in Physics Research, A569 (2006), 291-295.
- [4] Proffitt, J.; Hammond, W.; Majewski, S.; Popov, V.; Raylman, R.R.; Weisenberger, A.G.; Wojcik, R. "A flexible high-rate USB2 data acquisition system for PET and SPECT imaging", 2005 IEEE Nuclear Science Symposium Conference Record, Puerto Rico, October 23-29, 2005, pp. 2971-2975.
- [5] Proffitt, J., Hammond, W., Majewski, S.; Popov, V., Raylman, R.R., Weisenberger, A.G. "Implementation of a High-Rate USB Data Acquisition System for PET and SPECT Imaging", 2006 IEEE Nuclear Science Symposium Conference Record, San Diego, California, October 29 - November 1, 2006, pp. 3063 - 3067.
- [6] M. F. Smith, S. Majewski, A. G. Weisenberger, D. A. Kieper, R. R. Raylman, and T. G. Turkington, "Analysis of factors affecting positron emission mammography (PEM) image formation", IEEE Trans. Nucl. Sci., vol. 50, pp. 53-59, 2003.
- [7] M. F. Smith and R. R. Raylman, "PEM-PET image reconstruction in a clinically-relevant time frame", IEEE 2006 Nuclear Science Symposium Conference Record, pp. 1792-1796.

Development of a Mini Gamma Camera for Prostate Imaging

S. Majewski¹, J. Proffitt², A. Stolin¹

¹Center for Advanced Imaging, Department of Radiology West Virginia University, Morgantown, WV, USA

²AiT Instruments, Newport News VA, USA

Abstract– We have tested a concept of a mini gamma camera based on monolithic arrays of MPPCs from Hamamatsu. CsI(Tl), and Cs(Na) arrays and a thin scintillation GSO plate were tested with 122 keV gammas from ⁶⁰Co sources. The planned application requires placement of this mini-camera in an endorectal probe and thus needs to be very compact and possess high spatial resolution. The high sensitivity and high granularity collimator and gamma shield made out composite material (tungsten powder with epoxy) completes the detector package. We are developing the dual modality (hybrid) imaging prostate probe combining in one compact device a high resolution and high efficiency single gamma imager with an Ultrasound (US) sensor. The US component will typically provide not only the usual structural 3D information, as the standard TransRectal Ultrasound (TRUS) probe, but also the tissue differentiating information through proper US signal analysis, such as elastography. The mini gamma probe will provide the direct metabolic information related to the biological state of the prostate and specifically about the presence of any cancerous structures exhibiting increased metabolic activity, when used with the single gamma labeled dedicated imaging agents for prostate cancer. In addition to cancer diagnosis, the dual-modality Gamma/US prostate probe can be used in biopsy and in surgical guidance.

I. INTRODUCTION

Hybridyne Imaging Technologies [1] is introducing to the market (FDA approval was obtained in Spring of 2010) a prostate mini gamma probe ProxiScanTM based on Cadmium Zinc Telluride (CZT) technology developed at Brookhaven National Laboratory [2]. However, the way the probe is implemented with the associated electronics, there is no room for the addition of an US sensor in the same package. On the other hand, the SiPM/scintillator technology allows for more flexibility in choosing and modifying the detector structure. Figure 1 shows the “tile-able” arrangement of four Hamamatsu monolithic MPPC arrays, proposed for the new probe. After redirecting by 180 degrees the two cables from

the structure in the picture, as shown schematically at top right, and adding a scintillator and a collimator, a ~1” detection module is obtained. Two of these modules can be stacked one behind the other to form a larger ~1” x 2” module, but with a small gap and step in between. An external gamma shield needs to be added to prevent gamma radiation to bypass the collimator and enter the scintillator from the sides and the back of the probe.

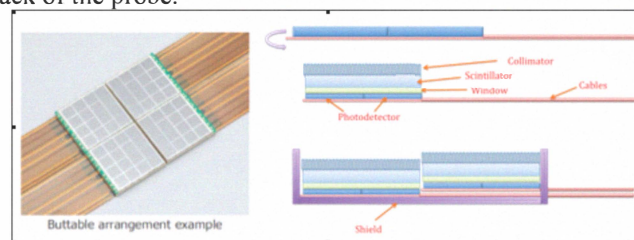


Figure 1. Concept of the prostate gamma probe based on a 2x2 array of monolithic ~1/2 inch 16ch MPPC arrays from Hamamatsu. The design requires that the two flat cables from the front (left) monolithic arrays can be bent by 180 deg under the sensors. The active obtained in this way field of view (FOV) is about 1” by 1”. Two modules can be in principle stacked to form a larger FOV device, as shown at right. No US sensor is added in this example. External gamma shield will be added to prevent gamma radiation from bypassing the collimator and entering the scintillator from the sides and the back of the probe. The gamma shielding is omitted in this sketch.

In Figure 2 a variant of the probe is shown with ultrasound (standard transrectal ultrasound –TRUS- or/and elastography or other tissue differentiating option) sensor included in the same probe enclosure with gamma sensor. In a serial implementation of the dual modality package the US sensor will be placed preferentially in front of the package, with the gamma part at the back. Positioning sensor will keep a track of the probe position and enable fusion of the images obtained from the two modalities.

Manuscript received December 2, 2011. This work was supported in part by the U.S. Department of Defense, contract number award W81XWH-09-1-0420.

S. Majewski and A. Stolin are with the Department of Radiology, West Virginia University, Morgantown, WV (telephone: 304-293-1878, e-mail: smajewski@hsc.wvu.edu). James Proffitt is with AiT Instruments, Newport News, VA).

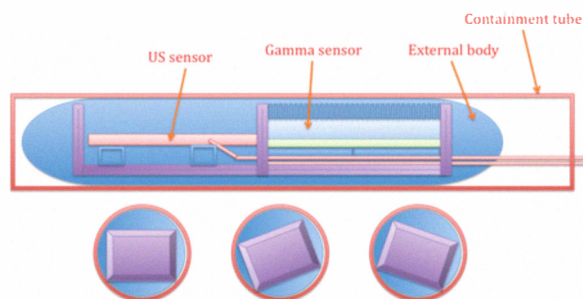


Figure 2. Dual modality prostate probe concept with US sensor in front and PET sensor behind. The probe can be angled/tilted to view different regions of the prostate and surrounding tissue. The slightly larger containment tube assures that the prostate is minimally disturbed during probe insertion and operation, shifts, rotations, etc. The shielding is not shown.

In yet another variant, schematically shown in use in Figure 3, a sketch of a hypothetical protocol is shown with the hybrid probe placed in two different positions for the two separate measurement sessions for the two modalities. In this case an especially good control of the probe position relative to the prostate is necessary.

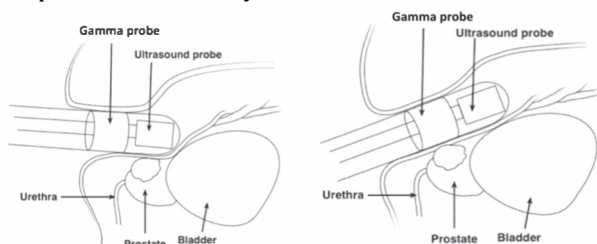


Figure 3. This drawing shows the rough sketch of the dual-modality probe with separate locations for the two sensors, placed in two positions: during the US imaging phase (left), and then during the gamma imaging phase (right). The probe is maneuvered into position first with the US sensor close to the prostate, and then with the gamma sensor close to the prostate, respectively. No containment tube, shown in Figure 2, is used in this example, to assure maximum flexibility in the probe positioning.

The key mechanical issue is controlling and recording the position of the probe. Optical based systems cannot be applied in this case. After extensive trials with the Ascension microBird and miniBird probes [3] and many discussions with the experts-practitioners, we abandoned the idea of magnetic based on-board sensors, due to the often-present interference of the metal surfaces with the operation of these probes in the practical environment. Our tested in the laboratory solution, and also demonstrated to and approved by the WVU oncologist/surgeon is the mechanical arm from with on-board positioners (MicroScibe G2X from GoMeasure3D [4] will keep a track of the probe position and orientation (Figure 4) and enable fusion of the images obtained from the two modalities. To stabilize prostate during

imaging, the hybrid probe can be inserted inside a thin-shell UV-compatible containment tube that would stay in place during the procedure, secured by an arm mounted to the patient's table, while the Gamma/US probe will be moved along the tube or even rotated to achieve better viewing of different parts of prostate.

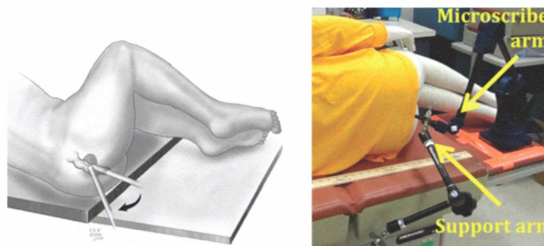


Figure 4. The Microscribe arm will provide the precise positioning of the probe with sub-mm accuracy, relative to the patient bed. The thin stylus of the Microscribe will be imbedded in the probe, and with the probe will be supported by another accompanying arm, mounted to the rails on the patient bed, as it has no mechanical locking mechanisms itself. The physician will adjust the position of the probe and lock the mechanisms on the support arm.

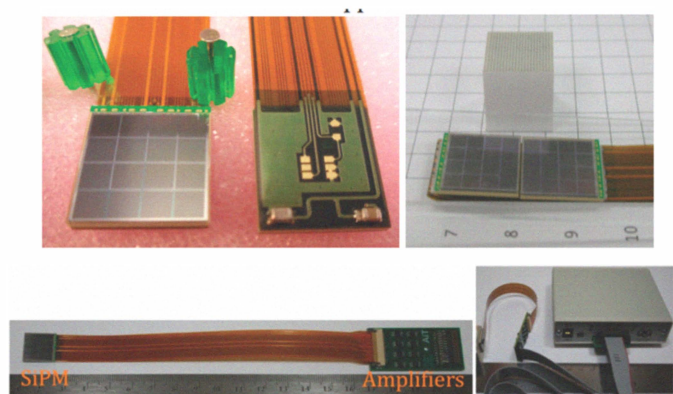


Figure 5. Two monolithic 4x4 MPPC arrays of 3mm MPPCs, model number S11829-3344MB(X), are shown at top left, can be tightly butted together in the proposed probe by a 180 degree bend of the cable from the front array placed in the front of the probe (the one at left in the top right picture). The readout also includes amplifier board at the end of the short flat cable (provided by Hamamatsu with the MPPC array) and the power supply/breakout interface box shown at bottom right, both from AiT Instruments.

The leading solution for the SiPM sensor is shown in Figure 5. There are no active electronic components (except MPPCs) on the Hamamatsu SMD MPPC array chip, and even the temperature sensor can be removed – as shown at top left in the figure (this assures maximum compatibility with MRI). The signals from the array to the amplifier card (from AiT Instruments [5]) are transferred in a flexible printed circuit cable. The amplifier cards will fit into the handle of the probe. The full system includes also one interface box per each 16 pad SiPM module (with low

voltage and bias voltage, and bias adjustment circuitry on board). The low profile cable between the amplifier card and the box can be as long as 15 ft, so the interface boxes can be stored in the electronics cabinet. The sixteen amplified output signals (from the individual 3x3mm SiPM pixels) from the boxes are delivered via standard 34-pin ribbon cables (not shown) to the 16-channel ADC module. Each 3mm MPPC pad was read separately by one channel in the integrating ADC.

II. APPARATUS AND EXPERIMENTAL METHODS

Several CsI pixellated scintillator samples were tested in the initial pilot phase. In addition, a continuous GSO plate was also used as another scintillator option. A special case of a CsI(Tl) scintillator imbedded in tungsten composite collimator based on the technology from Mikro Systems [6] is shown in Figure 6. High granularity of the produced structures

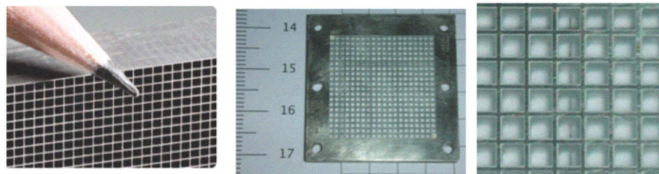


Figure 6. CsI(Tl) scintillator array from Mikro Systems [6] with 1.2mm pixel step imbedded in the composite tungsten collimator.

matches well with the high resolution of the scintillation sensor. In this scintillation/collimator package, the scintillator elements (CsI(Tl) or CsI(Na)) are imbedded in the collimator structure. Collimator septa also function in this case as separating walls of the individual scintillator pixels. To optimize the scintillation light transmission and collection, the surface of the septa is covered with reflective white material/paint. This design permits the most compact (in vertical dimension) structure of the collimator/scintillator package. Mikro Systems is one of the several companies custom-making such structures.

In our initial studies all the scintillation samples were coupled to the monolithic MPPC array, Model MPPC-MA1-1(X) (new model number is S11827-3344MG), the pre-model to the buttable variant of the 16ch MPPC monolithic array, via optical spreader window to increase scintillation signal sharing between the individual ~3mm MPPC sensors.

In majority of the tests wet optical coupling was used using coupling grease (Visilox V-788) between all coupled optical surfaces.

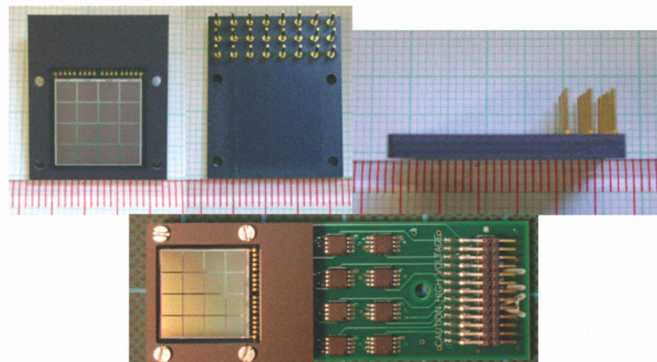


Figure 7. 16ch monolithic MPPC array MPPC-MA1-1(X) from Hamamatsu (new model number is S11827-3344MG), used in the initial demonstrations. The pad step is ~3mm. Except the frame packaging, this array is identical to the arrays from Figure 5 above.

We used our standard solution for the data acquisition system: the FPGA-based USB data acquisition system initially designed at Jlab [7, 8] and now available from AiT Instruments. This system has a modular, extensible architecture with up to 64 channels of simultaneous-sampling ADCs per unit and a sustained trigger rate of over 150 kHz for all 64 channels. DAQ unit sends time-stamped raw event data over high-speed USB to the acquisition computer. Using Kmax based software [9], the acquisition computer performs then centroid and energy calculations on the incoming data, as well as display and provides analysis tools for the collected images and histograms [10]. The images are typically promptly exported to public ImageJ imaging software for further processing.

III. RESULTS

We have performed initial laboratory validation of the gamma probe sensor of the new design. First, the monolithic Hamamatsu SiPM module, Model MPPC-MA1-1(X) (new model number is S11827-3344MG), was coupled through a 2mm thick light spreader window to a 1mm step 3mm thick CsI(Tl) array from Hilger Crystals [11]. Then, we tested the 1.2mm step CsI(Tl) array imbedded in the collimator, as seen in the Figure 6 above, also coupled through a 2mm window, and using optical grease between all optical surfaces. Finally, a 1mm thick 20mm x 20mm GSO plate from Hitachi [12] was also tested. The advantage of the latter design using plate GSO is that the whole structure becomes very compact, benefiting from high stopping power of GSO.

Results obtained with the 1mm step 3mm thick CsI(Tl) scintillation array from Hilger tested with the Co57 source (122 keV gammas) with dry and wet coupling are shown in Figure 8. The array was coupled to the monolithic MPPC array via a 2mm spreader window. Raw images and profiles demonstrate sub-mm intrinsic spatial resolution. The energy spectra from one of the 1x1x3mm CsI(Tl) pixels at right show scattered radiation peaks at left and photopeak at right with energy resolution 19.5% FWHM (dry coupling) and 18.6% (wet coupling) @ 122 keV.

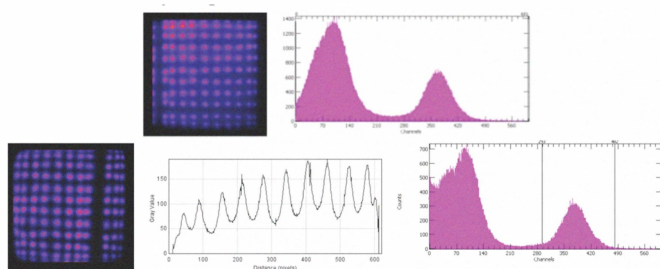


Figure 8. Results with 1.0 mm pitch 3mm thick CsI(Tl) Hilger scintillation array tested with the Co57 source (122 keV gammas). Top: dry coupling. Bottom: wet coupling (using coupling grease). In the wet coupling case also a vertical profile through one of the pixel columns in the center of the array is included. The array is made out of several joined sections that produce the observed discontinuities in the images. Energy resolution @122 keV.

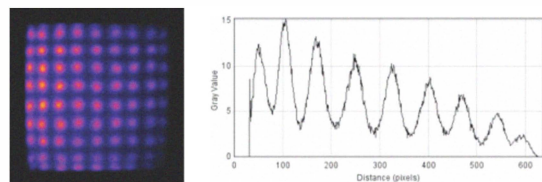


Figure 9. Results with 1.2mm pitch 3mm thick CsI(Na) scintillation array tested with the Co57 source (122 keV gammas). 2mm spreader window and wet coupling (optical grease) were used.

Figure 9 shows the results with the 1.2mm step 3mm thick CsI(Na) scintillation array tested with the Co57 source. The array was coupled to the monolithic MPPC array via a 2mm spreader window. Wet (optical grease) coupling was used. Raw image at left and profile through one of the pixel rows in the center, again demonstrate sub-mm intrinsic spatial resolution.

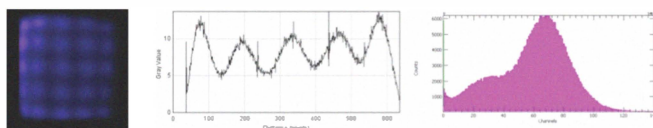


Figure 10. Results with the GSO 0.9mm thick plate and the lead mask. 2mm glass spreader window.

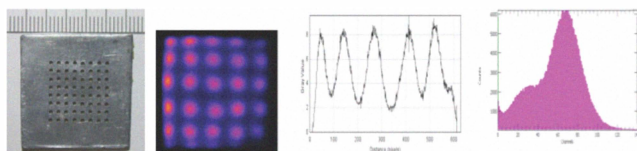


Figure 11. Results with the GSO 0.9mm thick plate and the lead mask (shown at left). 1mm thick glass spreader window was used in this case.

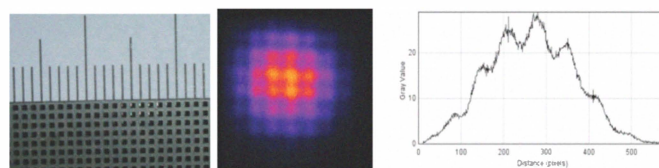


Figure 12. Results obtained with the 1mm thick GSO scintillator plate and a Co57 point source. The plate was coupled to the monolithic MPPC array via a 1mm thick light spreader window. Wet coupling (optical grease) and white diffusing paper on top of the scintillator plate were used. Raw image in the center is the image obtained with a 4mm thick composite Tungsten collimator having an array of square 0.6mm holes, spaced at 1mm center-to-center (picture shown at left). Vertical profile through one of the hole rows is shown at right.

Finally, Figures 10-12 show results obtained with the 0.9mm thick GSO scintillator plate from Hitachi [12] tested with the Co57 source. Wet coupling (optical grease) and white diffusing paper on top of the scintillator plate were used. Raw images in Figures 10 and 11 were obtained with a 1mm thick lead mask having an array of 1mm diameter holes, spaced at 2mm center-to-center. Vertical profiles through one of the columns, shown in the center, are demonstrating sub-mm intrinsic resolution of this mini-imager. Energy resolution of 36% @122 keV was measured.

As we plan to use our MPPC based compact probes (PET and gamma) without cooling circuitry, the crucial aspect of their use is the control of the MPPC gain, which is known to vary strongly with temperature and we confirmed that too (Figure 13). In the series of experiments geared towards PET application, but with the results applicable to the present single gamma case, we have shown that it is possible to correct the gain of the MPPC arrays in a very effective manner by adjusting the bias voltage (Figure 14). This requires that the gain is constantly monitored and that the bias voltage is automatically adjusted accordingly to the measured on-board temperature of the sensor. The miniature temperature sensors would therefore be included in the probe package and read continuously by the data collecting software. Hamamatsu gives as an option the digital temperature sensor placed on the back of the monolithic arrays, but we will use a separate temperature sensor with its analog signal read by our DAQ system.

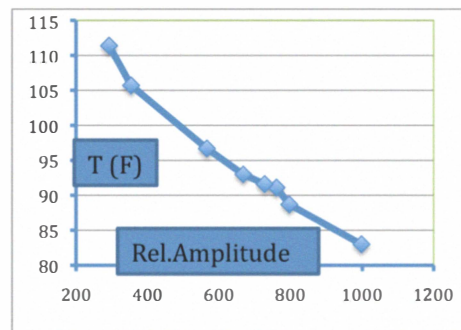


Figure 13. MPPC signal change with constant bias voltage @ 74.4V, covering the expected temperature range in application in the prostate imaging.

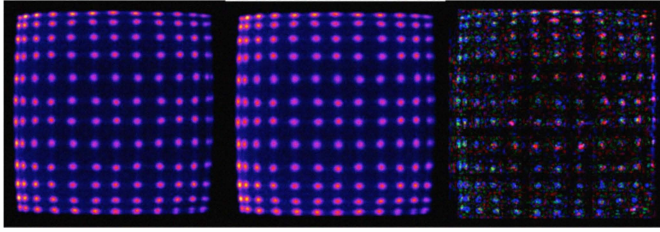


Figure 14. Study of the correction of the temperature effect. Examples of raw images at 87.7F & 73.4V (left) and at 111.1F & 74.4V (center) obtained with 1mm LYSO array and 511 keV gammas from a Na22 source. At right is the subtracted image (in ImageJ), demonstrating that the pixel positions did not visibly shift between the two operational points, and they stay well inside the separating them geometrical boundaries. The conclusion is that changing the bias voltage compensates for the gain change.

Finally, the potential challenge of the hybrid probe solution is the possible interference between the two sensors: PET and ultrasound (US). We performed a multitude of studies with separate US (elastography) and PET SiPM based probes placed close to each other, but not in the same enclosure. No additional shields, electrical or otherwise were used in these pilot tests. No noise or background pickup from the other sensor was observed in these parallel tests. The US probe produced standard images with the active unshielded PET probe placed next to it, and the output from the PET probe measured starting at the analog signal outputs and ending with the recorded 511 keV images, showed no noise component from the operation of the US sensor during US image acquisition. Figure 15 shows one example of one of the tested configurations. In addition, we also tested if the Microscribe position probe has impact on the operation of the US probe. None was observed.



Figure 15. Interference tests performed with the commercial in vitro 3D elastography probe, model Ultrasonix 4DEC9-5/10. Left and center: One of the many tests, here with the small PET probe variant based on a 16ch Hamamatsu MPPC array taped to the US probe. At right is the probe positioning during the test of the interference on US operation from the active Microscribe probe (during position data collection by the position probe). Both probes are placed on top of the commercial elastography prostate phantom [13]. No interference was detected.

IV. DISCUSSION AND CONCLUSIONS

The above pilot results demonstrate that compact gamma imaging probes based on SiPMs and scintillators for prostate imaging applications with 1mm intrinsic resolution are

feasible, while the overall spatial resolution (and sensitivity) will be defined by the collimator design and geometry (the distance to lesion). Additional work on improving energy resolution will be performed next. For example one of the new high-density gadolinium scintillators to be evaluated next as the candidate for this application is GAGG from Furukawa [14].

In summary:

- New compact variants of MPPC modules from Hamamatsu have highly improved performances, permitting their use in small-size compact gamma cameras - probes
- Therefore, we propose to implement the novel Hamamatsu monolithic MPPC arrays now in the single gamma probes
- CsI(Tl), CsI(Na), or GSO seem to be good scintillation sensor choices (with GAGG as the potential next option)
- Crucial novel aspect for the prostate application is the combination of the gamma sensor with the US sensor in one hybrid package
- Preferred US sensor will be the tissue-differentiating variant, using techniques such as elastography

The key still remaining, not only technical, issues related to the implementation of this technique are listed below:

- Assembly of arrays of monolithic MPPC modules
- Active temperature control and gain correction feedback
- Effective demonstrated control of the organ (prostate) position
- Dual modality compact probe implementation with US
- Image and information fusion from gamma and US
- **Need for prostate-specific imaging agents labeled with single gamma emitters as companions to the improved gamma/US imaging**

In summary, the main remaining challenge in our opinion (in the case of the prostate and the same applies to the case of the Hybrid probe) is the coupling of this high performance gamma probe with the high sensitivity and specificity gamma imaging agent for prostate cancer. Despite many years of application, the ProstaScint, which is FDA approved for prostate imaging, did not show enough evidence for high affinity for the prostate cancer. And only a combination of a high performance imaging instrument and prostate cancer specific imaging agent will enable efficient detection of early stages of prostate cancer.

However, this type of hand-held probe could find also other applications in assisting with biopsy and surgery, and lymphoscintigraphy of other cancers, such as melanoma, breast, head and neck (thyroid), etc, where the presently used imaging agents (for example Tc99m-Sestamibi in the case of breast cancer) do perform well. A relevant development was recently reported on a gamma probe based on a pixellated (0.6mm x 0.6mm x 6mm) YSO scintillator array coupled to a Hamamatsu 16ch MPPC array model S11064-050P [15].

V. ACKNOWLEDGEMENTS

We thank Dr Mohamad Salkini, MD, Director of Robotics & Minimally Invasive Surgery and Director of Urologic Simulation at the Department of Surgery at WVU for his continuous unwavering support of the prostate imaging projects. We thank our colleagues at the Center for Advanced Imaging of the Department of Radiology, WVU, Dr Ray Raylman and Peter Martone, for their encouragement and assistance with the project. Dr Sam Mukdadi from the College of Engineering and Mineral Resources at WVU provided us with the invaluable concepts how to incorporate the US sensor into our probes. Dr Ahmed Sayed from the College of Engineering and Mineral Resources at WVU we thank for assistance with the US probe tests. We finally thank very much Tom Bailey and Earl Hergert from Hamamatsu for providing us promptly with the samples of the new monolithic MPPC arrays, when they became available.

The study was supported in part by the U.S. Army Medical Research and Materiel Command prostate grant, award W81XWH-09-1-0420.

VI. REFERENCES

- [1] Hybridyne Imaging Technologies, Toronto, Ontario, Canada, <http://www.hybridyneimagingtechnologies.com>
- [2] Y. Cui, T. Lall, B. Tsui, J. Yu, G. Mahler, A. Bolotnikov, P. Vaska, G. De Geronimo, P. O'Connor, G. Meinken, J. Joyal, M. Pomper, S. Cho, K. Weisman, Y. Seo, J. Babich, N. LaFrance, and R.B. James, Compact CdZnTe-based gamma camera for prostate cancer imaging, BNL-96182-2011-CP, Presented at the 2011 IEEE Nuclear Science Symposium and Medical Imaging Conference (2011 NSS/MIC), Valencia, Spain, October 23-29, 2011.
- [3] Ascension Technology Corporation, Milton, Vermont, <http://www.ascension-tech.com/>.
- [4] GoMeasure3D, Amherst, VA, <http://www.gomeasure3d.com/MicroscribeG.html>
- [5] AiT Instruments, Newport News, VA, www.ait-instruments.com
- [6] Mikro Systems, Charlottesville, VA, <http://www.mikrosystems.com/applications/computed-tomography>
- [7] Proffitt, J.; Hammond, W.; Majewski, S.; Popov, V.; Raylman, R.R.; Weisenberger, A.G.; Wojcik, R. A flexible high-rate USB2 data acquisition system for PET and SPECT imaging. 2005 IEEE Nuclear Science Symposium Conference Record, Puerto Rico, October 23-29, 2005, pp. 2971-2975.
- [8] Proffitt, J., Hammond, W., Majewski, S.; Popov, V., Raylman, R.R., Weisenberger, A.G. Implementation of a High-Rate USB Data Acquisition System for PET and SPECT Imaging, 2006 IEEE Nuclear Science Symposium Conference Record, San Diego, California, October 29 – November 1, 2006, pp. 3063 - 3067.
- [9] Sparrow Corporation, Port Orange, FL, <http://www.sparrowcorp.com/>
- [10] J. E. McKisson, W. Hammond, J. Proffitt, and A.G. Weisenberger, A Java Distributed Acquisition System for PET and SPECT Imaging, 2007 IEEE Nuclear Science Symposium Conference Record, pp. 3591-3593.
- [11] Hilger Crystals, Margate Kent CT9 4JL, England.
- [12] Hitachi Chemical Co., LTD, 10080 North Wolfe Rd., Suite SW3-200, Cupertino, CA 95014.
- [13] Model CIRS 066 from Supertech, Elkhart, IN, <http://www.supertechx-ray.com/a6590-r.htm>
- [14] Furukawa Co., Ltd., Tsukuba-city, Ibaraki, Japan, <http://www.furukawakk.co.jp/e/business/others/>
- [15] S. Yamamoto, H. Watabe, Y. Kanai, M. Imaizumi, T. Watabe, E. Shimosegawa, J. Hatazawa, Development of a High Resolution Si-PM-Based Gamma Camera System, presented at the 2011 IEEE MIC conference, October 23-29, 2011, held in Valencia, Spain.



Silicon detectors for combined MR–PET and MR–SPECT imaging

A. Studen^{a,*}, K. Brzezinski^d, E. Chesi^b, V. Cindro^a, N.H. Clinthorne^c, E. Cochran^b, B. Grošičar^a,
M. Grkovski^a, K. Honscheid^b, H. Kagan^b, C. Lacasta^d, G. Llosa^d, M. Mikuž^{a,e},
V. Stankova^d, P. Weilhammer^b, D. Žontar^a

^a Jožef Stefan Institute, Ljubljana, Slovenia

^b The Ohio State University, Columbus, OH, USA

^c The University of Michigan, Ann Arbor, MI, USA

^d IFIC/CSIC-UVeG, Valencia, Spain

^e The University of Ljubljana, Ljubljana, Slovenia

ARTICLE INFO

Keywords:

PET

Silicon detectors

SPECT

ABSTRACT

Silicon based devices can extend PET–MR and SPECT–MR imaging to applications, where their advantages in performance outweigh benefits of high statistical counts.

Silicon is in many ways an excellent detector material with numerous advantages, among others: excellent energy and spatial resolution, mature processing technology, large signal to noise ratio, relatively low price, availability, versatility and malleability.

The signal in silicon is also immune to effects of magnetic field at the level normally used in MR devices. Tests in fields up to 7 T were performed in a study to determine effects of magnetic field on positron range in a silicon PET device. The curvature of positron tracks in direction perpendicular to the field's orientation shortens the distance between emission and annihilation point of the positron. The effect can be fully appreciated for a rotation of the sample for a fixed field direction, compressing range in all dimensions. A popular Ga-68 source was used showing a factor of 2 improvement in image noise compared to zero field operation. There was also a little increase in noise as the reconstructed resolution varied between 2.5 and 1.5 mm.

A speculative applications can be recognized in both emission modalities, SPECT and PET.

Compton camera is a subspecies of SPECT, where a silicon based scatter as a MR compatible part could inserted into the MR bore and the secondary detector could operate in less constrained environment away from the magnet. Introducing a Compton camera also relaxes requirements of the radiotracers used, extending the range of conceivable photon energies beyond 140.5 keV of the Tc-99m.

In PET, one could exploit the compressed sub-millimeter range of positrons in the magnetic field. To exploit the advantage, detectors with spatial resolution commensurate to the effect must be used with silicon being an excellent candidate. Measurements performed outside of the MR achieving spatial resolution below 1 mm are reported.

© 2012 Elsevier B.V. All rights reserved.

1. Introduction

High-resistivity silicon sensors as direct detectors of radiation offer a number of advantages in detection of radiation in nuclear medicine, among others:

- An excellent spatial resolution, with demonstrated resolution of 1 μm [1] achieved with double sided strip detectors. The requirements are not nearly as harsh in nuclear medicine, where resolutions around 1 mm seem optimal.

- An excellent energy resolution of 1–2 keV FWHM in the range of signals between 59.5 and 511 keV [2].
- Mature processing and design technology, offering relatively cheap, highly configurable, sturdy and compact detectors.

Their most serious drawbacks are:

- A relatively low stopping power, with attenuation coefficient varying between 0.02 and 0.03 mm^{-1} in the range of photon energies (140.5–511 keV) encountered in tracking of principal radionuclides. The low stopping power can be compensated by stacking of multiple sensors and proper multiplexing of the readout channels.
- Relatively poor timing performance related to long collection times. The problem can be circumvented with proper operating

* Corresponding author. Tel.: +386 1 477 3162.
E-mail address: andrej.studen@ijs.si (A. Studen).

conditions, higher reverse bias applied over the sensor to speed up the charge collection, and modified sensor geometry, using interconnected thinner sensors to shorten the required drifting length. Both approaches combined yield devices that could be operated to activities of 50–100 MBq in and around the field of view [3] matching requirements posed by most applications in clinical imaging.

Nevertheless, silicon detectors could be used in targeted applications where one could exploit their advantages while compensating for their drawbacks. Two specific arrangements are presented, a Compton camera with silicon detectors [4] and a dual PET ring [5] with inner detector composed of silicon sensors.

Silicon detectors can be operated in magnetic fields without performance degradation [6], especially if the electric field in the device is parallel to the external magnetic field. For other relative orientations, the severe Lorentz angle [7] for electrons (55° for 8 T field) is partially compensated by signal of the holes where deflection is much smaller (14° at 8 T), pad geometry with a pad side slightly larger than the sensor thickness, and offline correction techniques. A silicon based device was built to study effects of magnetic field on imaging properties, more specifically the fact that the range of positrons is reduced in the direction perpendicular to the direction of the field due to circular motion of the positrons. A brief summary of the study will be presented.

2. Compton camera

Compton camera is a principle that can profit from usage of silicon detector. In a Compton camera, emitters of single photons are tracked based on Compton kinematics. Usually, the camera is composed of two detectors: a scatterer where initial photons interact through Compton scattering, generating Compton electrons to be analyzed by the sensor, and an absorber to capture the scattered photon. Impact positions in both sensors yield the scattered photon track, and the energy E_e of the Compton electron is related to the scattering angle θ through Compton kinematics

$$\sin^2 \frac{\theta}{2} = \frac{E_e}{E_\gamma - E_e} \frac{m_e c^2}{E_\gamma}, \quad (1)$$

where E_γ is the initial energy of the photon, m_e is the electron mass and c the velocity of light in vacuum. At low energies, the principal component of the spatial resolution of the source position will come from limited angular resolution of the Compton collimation due to limited energy resolution of the sensor, ΔE_e .

$$\Delta\theta \propto \frac{\Delta E_e}{E_\gamma^2}, \quad (2)$$

with rapid improvement with growing E_γ .

The principle was tested with a prototype that combined a silicon pad detectors with a cell size of $1.4 \times 1.4 \times 1 \text{ mm}^3$ as a scatterer coupled to low-noise readout electronics with a plain gamma camera with collimators removed and a resolution of 5–6 mm FWHM as an absorber [4]. The distance between the source and the scatterer was approximately 10 cm while the absorber was a further 20 cm away. Point sources of nuclides used in nuclear medicine (^{99m}Tc , ^{131}I , ^{22}Na) were placed on a rotary table and rotated in front of a slit collimator that compressed the imaging field to a single slice that contained the 1 mm thick silicon sensor. Images were reconstructed using a filtered back-projection algorithm. The resolutions obtained are shown in Fig. 1 and compared to simulations.

At low energy, the Doppler broadening has a significant impact on the resolution. Modeling of the broadening has only recently been introduced to modeling software package EGS5 [8]. In the reference, the authors allow for certain discrepancies in treatment

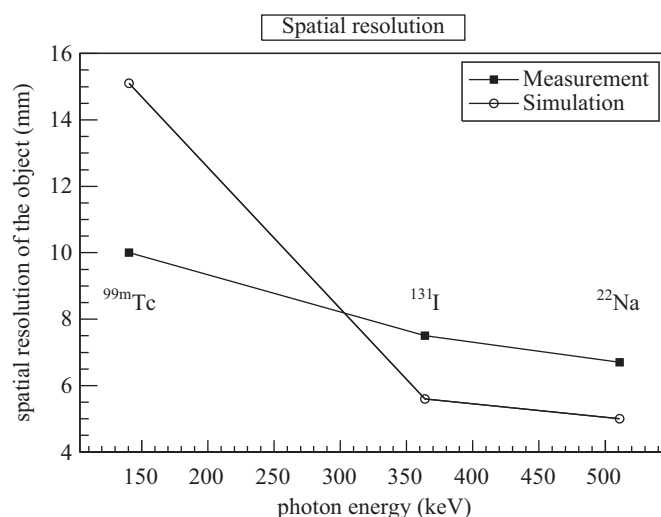


Fig. 1. Spatial resolution of the reconstructed point source measured with a Compton camera prototype. Horizontal axis indicates the energy of the photons used in reconstruction for source indicated next to the measurement points. Vertical axis shows the reconstructed resolution. Curves for measurement and simulation are shown.

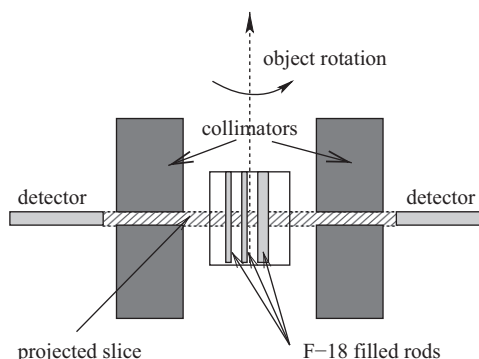


Fig. 2. Geometry of silicon detectors and collimators used in dual ring prototype and in the device to measure the positron range in a magnetic field. The magnetic field, if present, was parallel to the axis of rotation of the object.

of momentum distribution of the bound electrons: firstly atomic rather than crystalline distributions are used and secondly, approximation rather than tabulated values were used in their estimation. Although observable in Fig. 1, the effect was not further explored as the obtained results outline the predicted improvement in performance with growing E_γ .

A similar device could be used in magnetic fields allowing only the MR compatible part, the scatterer, to be inserted into the MR bore, while the absorber could be placed into a more relaxed environment further away from the magnet.

3. Dual ring PET

In a dual ring PET [5,9] a silicon ring is used as insert to a standard PET detector ring. Events when one or both photons interact in the silicon detector exhibit excellent spatial resolution, contributing to improved image quality when combined with data obtained from the standard scanner. Calculations show that only a small fraction of events with a high spatial resolution are required making silicon a possible choice of the inner ring detector material.

A demonstrator of the dual ring geometry was constructed at the University of Michigan [5]. Concentrating only on the inner ring, detectors are placed as indicated in Fig. 2, with two 1 mm thick silicon detectors placed behind a slit collimator that compresses the

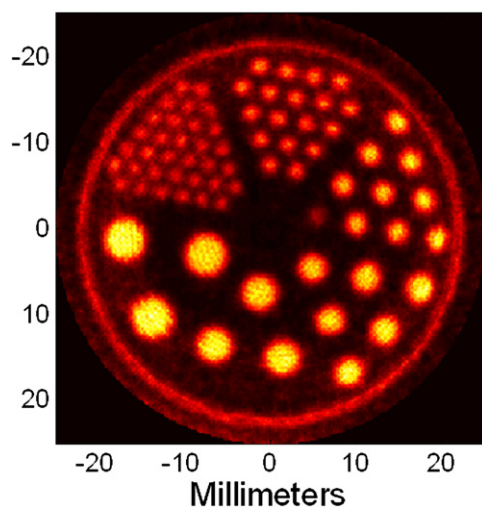


Fig. 3. Reconstruction of a single slit of a Derenzo rod phantom filled with ^{18}F -FDG, with hole diameters ranging from 1.2 to 4.8 mm as measured in the setup indicated in Fig. 2. A total of 8.6 million events contributed to the image.

imaging field to a single, 1 mm thick slice through the imaging object, which is rotated for a full angular view. The imaging object is a Derenzo rod phantom with rod diameters ranging between 1.2 and 4.8 mm, filled with ^{18}F -FDG with peak activity of 185 MBq. Multiple 5 h sessions were performed to accumulate 8.7 million counts used in MLEM reconstruction shown in Fig. 3, indicative of a full ring performance. Resolution well below 1.2 mm can be recognized from the images.

Data was also collected in the volumetric PET mode, where the collimator was removed and the detectors were positioned perpendicular to the predominant direction of the annihilation photons. The same resolution was achieved when point sources of ^{22}Na were imaged.

4. PET ring in a magnetic field

A similar arrangement as in Fig. 2 was placed in a 7 T MR magnet at the Ohio State University [6]. There was no degradation in performance of the sensors. The device was used to monitor changes in the range of positrons in a magnetic field. A ^{68}Ga source with maximum positron energy of 1.899 MeV was imaged both in and outside of the magnet. The resolution changed between from 2.3 to 1.6 mm FWHM when a magnetic field with a strength of 7 T was applied, allowing a separation of a pair of sources placed 3.6 mm apart in the magnetic field, which were inseparable in the 0 T field.

The compressed positron range also shows an adverse effect on artifacts stemming from annihilations of positrons emitted by sources located off the plane of the selected object slice. Without the field, the off-plane sources contribute a relatively flat background which is indistinguishable from noise. In the field, the annihilations are sharply concentrated around the projection of the source on the selected slice, giving sharp artifacts in the reconstructed image. To remove the artifacts, the object must be imaged in multiple field orientations, posing additional requirements on a device to exploit the compressed range of the positrons in a magnetic field.

5. Conclusion

Benefits of silicon detectors can be exploited in targeted applications in nuclear medicine. Operation of silicon detectors is not perturbed by a presence of a magnetic field, which makes them feasible for targeted MR-SPECT or MR-PET applications as well. The high spatial resolution of silicon detectors is sufficient to monitor changes in positron range in magnetic field. To exploit the smaller positron range, the object must be rotated within the field during imaging.

Acknowledgments

The work presented was co-funded by the NIH Grants R01 EB430-35 and R01 EB430-37, the US Army Congressionally Directed Medical Research Program under Grant W81XWH-09-1-0413, and EURATOM FP7 collaborative project MADEIRA.

References

- [1] J. Straver, et al., *Nuclear Instruments and Methods in Physics Research A* 348 (2–3) (1994) 485.
- [2] A. Studen, et al., *Nuclear Instruments and Methods in Physics Research A* 501 (2003) 273.
- [3] A. Studen, et al., *Nuclear Instruments and Methods in Physics Research A* 648 (S1) (2011) S255.
- [4] E. Cochran, et al., Performance of electronically collimated SPECT imaging system in the energy range from 140 keV to 511 keV, in: *IEEE NSS Conference Record* 4618–21.
- [5] N.H. Clinthorne, et al., Silicon as an unconventional detector in positron emission tomography, *Nuclear Instruments and Methods in Physics Research A*, <http://dx.doi.org/10.1016/j.nima.2012.05.026>, in press.
- [6] D. Burdette, et al., *Nuclear Instruments and Methods in Physics Research A* 609 (2–3) (2009) 263.
- [7] V. Bartsch, et al., *Nuclear Instruments and Methods in Physics Research A* 497 (2–3) (2003) 389.
- [8] H. Hirayama, et al., The EGS5 code system, SLAC-R-730, 2010.
- [9] N.H. Clinthorne, et al., Very High Resolution Animal PET, Presented at 47th Society of Nuclear Medicine Annual Meeting, St Louis, MO, June 2000.

Construction and Testing of a Prototype High Resolution, Silicon Photomultiplier-Based, Tandem Positron Emission Tomography System

Alexander V. Stolin, Stan Majewski, Gangadhar Jaliparthi and Raymond R. Raylman, *Member, IEEE*

Abstract— While the performance of most current commercially available PET scanners is sufficient for many standard clinical applications, some specific tasks likely require specialized imaging systems. The goal of this project is to explore the capabilities and limitations of a small, high-resolution prototype system for obtaining PET images. The scanner consists of a tandem of detectors. One is a small detector consisting of a 20x20 array of 0.7x0.7x3mm³ (pitch 0.8mm) LYSO elements. The scintillator array is coupled to an array of silicon photomultipliers. The second detector is a 96x72 array of 2x2x15mm³ (pitch=2.1mm) LYSO elements coupled to PSPMTs. Separation between the two devices is 180 mm. The detectors are operated in coincidence with each other. Image reconstruction is performed using a limited angle Maximum Likelihood Expectation Maximization (MLEM) algorithm. Spatial resolution and field-of-view vary as a function of distance from the small detector. Evaluation of the device included measurements of spatial resolution and detection sensitivity as a function of distance. The transaxial radial and tangential spatial resolution of the system ranged from 0.6mm to 0.9mm FWHM; axial resolution ranged from 2.7mm to 4.6mm FWHM. Detection sensitivity ranged from 0.05 to 0.28%. The tandem system permitted differentiation of the smallest (1mm diameter) rods in a mini-hot rod phantom. In summary, evaluation of the basic imaging characteristics of a tandem, high resolution PET system revealed very good results for in-plane spatial resolution and detection sensitivity. Axial spatial resolution is diminished by the utilization of limited angle data acquisition and reconstruction. These results indicate that the tandem PET imager system can be potentially employed in applications where high-resolution images over a small region are required.

Index Terms—PET Instrumentation, Nuclear Medicine Imaging

I. INTRODUCTION

DRIVEN by clinical and research needs, PET scanners are pressed to identify ever smaller areas of radiotracer accumulation (perhaps as small as one millimeter or less in diameter). To meet these demands, very-high resolution PET scanners are under development. For example, PET scanners with reported spatial resolution approaching 1mm FWHM have been developed for small animal use [1-3] and 4mm for human use [4]. These advances have been achieved, for the most part, by the reduction of detector element size. For animal imaging applications, the continued reduction in detector element size to achieve higher resolution is not particularly onerous or expensive given the size of the systems. For human scanners, however, continued reduction in detector element size will have significant impact on cost and complexity, since these systems are considerably larger than small animal scanners.

To address the important issue of increased spatial resolution for the next generation of special-purpose PET scanners, a new technique utilizing separate detectors has been proposed [5-8]. In this method, a small, high-resolution detector is combined with a, large, lower-resolution detector, often a standard PET scanner. By forming coincidences between the high-resolution detector and the lower-resolution system, high-resolution images (approaching the resolution of the high-resolution detector) can be created over a small region. The spatial resolution of a tandem PET is a function of position and is given by[6]:

$$R_{sys} \approx \sqrt{R_{src}^2 + \left[0.0088 \cdot \frac{d_1 \cdot d_2}{d_1 + d_2} \right]^2 + \left[\frac{d_2 \cdot w_2 + d_1 \cdot w_2 + |d_2 \cdot w_1 - d_1 \cdot w_2|}{2 \cdot (d_1 + d_2)} \right]^2}. \quad (1)$$

Where R_{sys} is the system resolution, R_{src} is the effective source dimension that includes positron range effects, d_1 is the distance from the high-resolution detector to the object, d_2 is the distance from the lower-resolution detector to the object, w_1 is the width of the high-resolution detector elements and w_2 is the width of the lower-resolution detector elements. This equation shows that resolution is spatially dependant. The closer the object is to the high-resolution detector (small d_1), the closer the resolution of the system gets to the size of a detector element (w_1). Thus, a tandem detector system is best

Manuscript received April 12, 2012. This work was supported in part by the United States National Institutes of Health (Grants R01 EB007349 and R01 CA094196)

R.R. Raylman is the corresponding author (rraylman@wvu.edu).

All of the authors are with the Center for Advanced Imaging in the Department of Radiology at West Virginia University, Morgantown WV USA.

applied to situations where the small, high-resolution detector can be placed very close to the object to be imaged. For example, the high resolution detector could be used in conjunction with a clinical PET scanner to enhance its resolution for localized imaging applications; or a standalone system comprised of both the high and lower-resolution detector could be created. In either case the aim is to produce a high-resolution system for localized imaging. The goal of this investigation was to construct a compact tandem PET imager and assess the potential imaging capabilities and limitations of this method.

II. METHODS

A. High-Resolution Detector

The compact, $16 \times 16 \text{ mm}^2$, high-resolution component of our system consists of a 20×20 array of $0.7 \times 0.7 \times 3 \text{ mm}^3$ LYSO detector elements (pitch 0.8mm) (Proteus, Inc., Chagrin Falls, OH). Each detector element is optically isolated from its neighbors with enhanced specular reflective (ESR) film. The scintillator array was coupled to a 4×4 array of $3 \times 3 \text{ mm}^2$ MPPC silicon photomultipliers (Hamamatsu Photonics, Inc., Hamamatsu City, Japan) through a 2.9mm-thick piece of ultraviolet-transmissive acrylic. This light guide thickness was found to be best for spreading light amongst multiple SiPM elements, facilitating calculation of the photon interaction point in the scintillator array. The goal was to make the detector as compact as possible for potential incorporation in an endorectal probe. The array of MPPCs was controlled via a custom sixteen-channel electronics module (AiT Instruments, Newport News, VA). These electronics provide power to the MPPCs, route each of the sixteen channels of the MPPC array to an ADC module, as well as sum the output channels to create an ADC trigger signal. The high-resolution detector is shown in Figure 1. The individual analog signals from the control electronics are digitized with a custom FPGA-based ADC (AiT Instruments) processed and stored. Identification of the interaction point in the scintillator array is accomplished via center-of-mass calculation of the digitized signals and pre-measured crystal and energy lookup tables. This method facilitates accurate and rapid determination of photon interaction points in the detector.

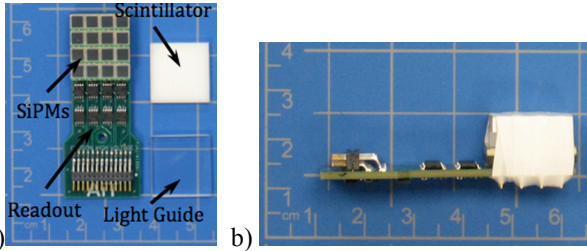


Fig. 1. Pictures of the high-resolution detector. A) Constituent parts of the detector and b) the assembled detector (the light-tight enclosure normally covering the device has been removed).

B. Lower-Resolution Detector

The lower-resolution detector consists of a 96×72 array of $2 \times 2 \times 15 \text{ mm}^3$ LYSO detector elements ($20 \times 15 \text{ cm}^2$). The

scintillator array is coupled to a 4×3 array of Hamamatsu H8500 PSPMTs [9]. The PSPMTs are readout by custom resistive readout electronics [10]. The analog signals from the readout are digitized by a specially designed FPGA-based ADC unit (AiT Instruments), then processed and stored on the data acquisition control computer. Identification of the interaction point in the scintillator array is accomplished via center-of-mass calculation of the digitized signals and pre-measured position and energy tables.

C. Tandem PET System

The lower resolution detector was mounted on a support frame, while the small high-resolution detector was not fixed to a hard point and could be moved to any location. For best imaging performance, however, it was placed on a horizontal table located in a support frame with its center aligned with the center of the lower-resolution detector. A schematic drawing and picture of the system are shown in Figure 2. The two detectors were 180mm apart. The high-resolution probe was used with a single large area detector panel instead of a commercial PET scanner for several reasons. First, we currently do not have the capability to modify our PET/CT systems for use with an external probe. Secondly, we are seeking to explore the development of a compact, cost-effective and portable standalone imaging system.

It is important to note that the rectangular field of view (FOV) of the system is a function of distance from the object to the high-resolution detector. The size of the FOV is given by:

$$FOV(d_1) = D_1 + d_1 \left(\frac{D_2 - D_1}{L} \right). \quad (2)$$

Where, $FOV(d_1)$ is the length of the FOV along the axis of choice (x- or y-axes), D_1 is the spatial extent of the high-resolution detector along the x- or y-dimension, D_2 is the spatial extent of lower-resolution detector, d_1 is the distance from the high-resolution detector and L is a constant (the sum of d_1 and d_2). Figure 3 shows a plot of FOV for our system. The FOV is a linear function of d_1 (it increases with increasing). The ratio of the difference between the detector sizes to the detector separation is the slope of the line and the size of the high-resolution detector is the y-intercept. Note that the FOV in the x-direction is slightly larger than in the y-direction in our system due to the fact that the lower-resolution detector is slightly longer in the x-dimension (20cm) than the y-dimension (15cm).

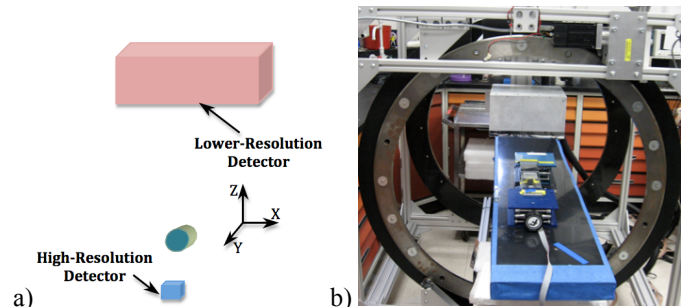


Fig. 2. The tandem PET system: a) schematic drawing and b) picture of the apparatus used for measurements.

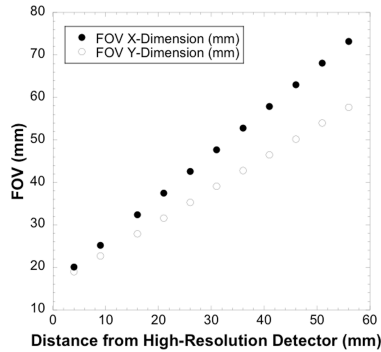


Fig. 3. Field-of-view of the tandem system as a function of distance from the high-resolution detector calculated from Equation 2.

The analog sum signals from the high and lower-resolution detectors are fed into a constant fraction discriminator. Pulses from the discriminator are routed to a coincidence module whose output is used to initiate analog-to-digital conversions in the FPGA-based ADCs connected to the high and lower-resolution detectors. Data are stored on a computer in list mode format. Images were created using a limited-angle Maximum Likelihood Expectation Maximization (MLEM) reconstruction algorithm and displayed using software written using the Interactive Data Language (IDL).

D. System Testing

To explore the imaging envelope of the tandem imager, basic parameters (spatial resolution and detection sensitivity) were measured as a function of object position. A small, point-like source of ^{18}F (0.1mm diameter) was aligned with the center of the detectors and positioned at several distances from the surface of the small probe (4mm to 56mm). For each source position, the position of the source was identified and profiles drawn in the plane horizontal to the detector face (x-y plane) and perpendicular to the detector face (x-z plane). The FWHMs of each profile were then calculated and plotted as a function of distance from the high-resolution detector. In addition to spatial resolution, the efficiency of the system was measured by placing a small disk (0.22mm diameter) containing a known amount of ^{22}Na was placed in the same positions as the point source used to assess spatial resolution. The number of detected events at each position was compared to the amount of photons emitted by the source.

Some of the potential benefits of the high spatial resolution possessed by this scanner were demonstrated by imaging a specially constructed hot-rod phantom. This phantom consists of four sectors with 1, 1.5, 2 and 2.5 mm-diameter cylinders. In each sector, the centers of the cylinders are separated by twice their diameter. The cylinders were filled with a solution containing ^{18}F . The phantom was imaged for five minutes in the tandem scanner (cylinders aligned with the z-axis). In addition, two pairs of gelatin spheres (3mm and 5mm diameter) were embedded in a 60x60x30mm³ block of gelatin. The gelatin contained 0.16μCi/ml of ^{18}F -Fluorodeoxyglucose (FDG), representative

of FDG uptake in adipose tissue [11]. The FDG concentration in one pair of spheres was 40 times the concentration in the gelatin block. The other pair contained 20 times the concentration in the gelatin block. The phantom was imaged in the tandem system for ten minutes.

III. RESULTS

Figure 4 shows an image of the point source used to measure spatial resolution. The image in Figure 4(a) is a transaxial view (x-y plane), while Figure 4(b) is an axial view (x-z plane). Figure 5 shows intensity profiles drawn through the images of the point source shown in Figure 4. The plots in Figure 6 show the results of the measurement of spatial resolution as a function of distance from the high-resolution detector. Detection sensitivity of the system as a function of distance from the high-resolution detector is shown in Figure 7. The very good spatial resolution of the system is demonstrated in the images of the hot rod phantom shown in Figure 8. The image of the phantom acquired with the tandem system demonstrates that all of the rods are discernable, even the very small 1mm-diameter rods. Finally, Figure 9 shows images of the phantom emulating positron-emitting, radiotracer-avid lesions in adipose-like tissue. All of the spheres are visually discernable from background. The intensity profiles shown in Figure 10 illustrate, in a more quantitative fashion, the contrast between the spheres and background. Specifically, the measured signal-to-background ratios are: 2.4:1 (3mm diameter, 20:1 FDG target-to-background ratio), 5:1 (5mm diameter 20:1 FDG target-to-background ratio), 3.2:1 (3mm diameter, 40:1 FDG target-to-background ratio) and 8:1 (5mm diameter, 40:1 FDG target-to-background ratio).

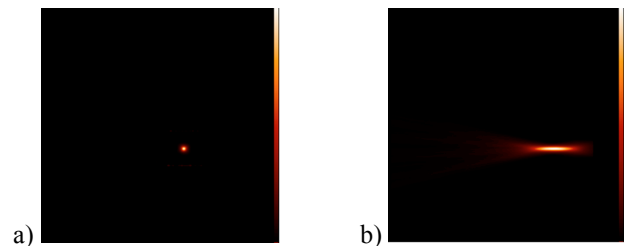


Fig. 4. Images of the point source phantom: (a) Image of the point source in the x-y plane and b) in the x-z plane.

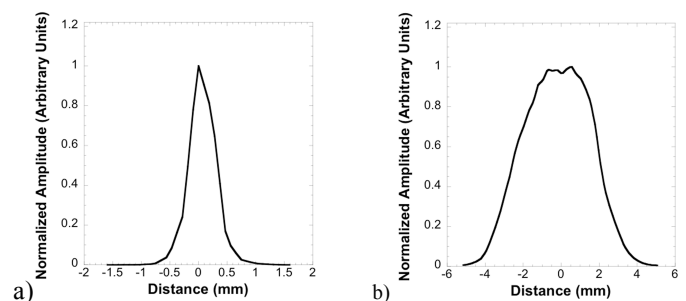


Fig. 5. Profiles drawn on image of a point source: (a) profile in the x-y plane and b) profile in the x-z plane.

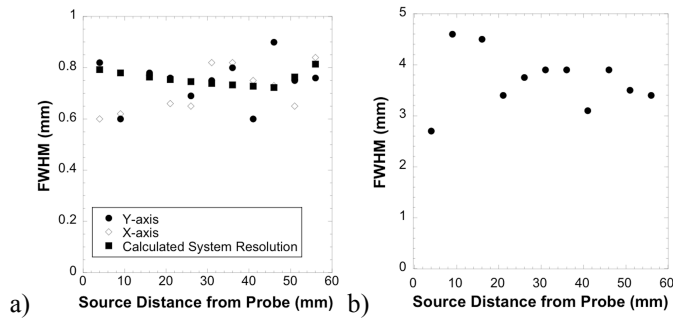


Fig. 6. Spatial resolution measurement.: (a) Resolution in the x and y directions in addition to resolution calculated with Equation 1 and (b) resolution in the z direction.

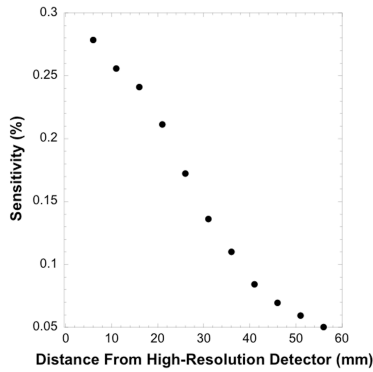


Fig. 7 Results from the detection sensitivity measurements.

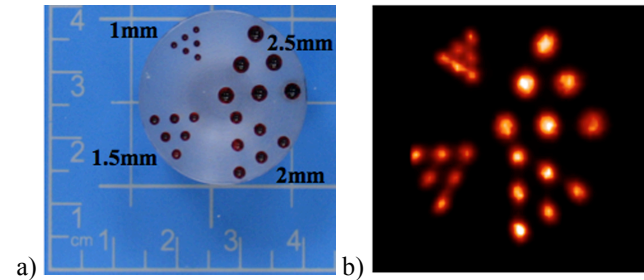


Fig. 8. Images of the hot rod phantom the x-y plane: (a) Picture of the phantom, each group of rods is labeled with their diameters and (b) image of the hot rod phantom from the tandem scanner.

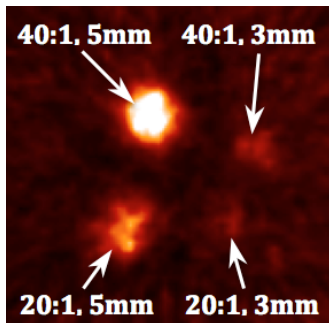


Fig. 9. Image of the phantom acquired with the tandem PET scanner. The size and target-to-background radiotracer concentrations for each sphere are shown.

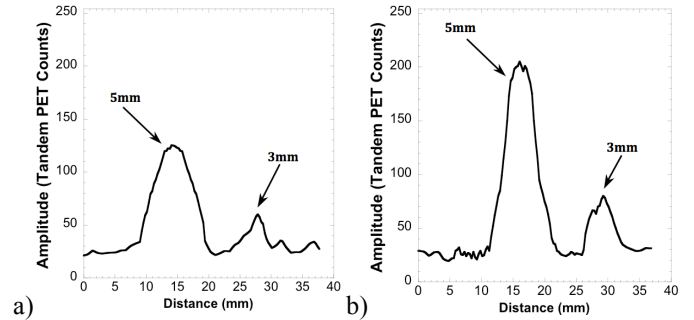


Fig. 10. Intensity profiles from the image shown in Figure 9: (a) profile drawn through the bottom row of spheres (20:1 target to background ratio) and (b) profile drawn through the top row of spheres (40:1 ratio).

IV. DISCUSSION

The imaging community strives continually to improve the spatial resolution of PET scanners. One potential approach is the use of a tandem detector system consisting of one detector with very small detector elements (high-resolution) and another larger area detector with larger detector elements (lower-resolution). This solution can potentially be used to create a system with very high spatial resolution without significantly increasing expense, since the total amount of scintillator and electronics is relatively small compared to most high-resolution ring scanners. The small size of the high-resolution detector is a very important attribute, making for potentially unique applications of the system. The major limiting factor is that the object must be placed very close to the high-resolution detector.

To assess the potential effectiveness of using the tandem detector scheme for high resolution PET imaging, we constructed and tested a prototype system. Initial evaluation of the imaging parameters showed some promising aspects of the scheme, while also illustrating some potential limitations. Specifically, the image shown in Figure 4(a), along with the intensity profile of Figure 5(a), illustrates the capabilities of the system to image a point source in the transaxial (x-y) plane. The image in Figure 4(b), along with the profile shown in Figure 5(b), shows the level of blurring in the axial dimension (z-axis), which limits the capabilities of the system to accurately localize a focal area of radiotracer uptake along this axis. The plot in Figure 6(a) shows that the transaxial (x-y plane) spatial resolution has relatively little dependence on distance from the high-resolution detector over the range of distances tested (~ 5 cm). Spatial resolution in this plane ranges from 0.6mm to 0.9mm FWHM. These results agree relatively well with the predicted values calculated using Equation 1. Variations in the individual values of measured spatial resolution (Figure 6) are produced by statistical noise in the data and difficulties in identifying the precise position of the point sources in the z-axis direction. This effect is due to blurring in the z-axis caused by incomplete angular sampling of the object.

The results shown in Figure 7 demonstrate that, for a small disk source, the detection sensitivity of the tandem system is spatially dependant. As a source is moved away from the high-resolution detector, the solid angle subtended by

this detector is reduced, while the solid angle subtended by the larger, lower-resolution detector increases, but at a much lower rate. Indeed, at a given distance, determined by the sizes of the detectors and their separation, sensitivity transitions from being high-resolution detector dominated to low-resolution detector dominated. From the results shown in Figure 7, this transition occurs at ~ 25 mm from the high-resolution detector where there is an inflection point in the curve. For a more distributed source, detection sensitivity would likely be somewhat more uniform as a function distance than for a point source. The magnitude of the detection sensitivity for this system is relatively small due to the very thin scintillator (3mm) utilized in the high-resolution detector. In this version of the detector, sensitivity was sacrificed for creation of a compact detector. Detection efficiency can be improved by making the high-resolution detector thicker or larger.

While quantitative test results provide good metrics with which to assess the potential capabilities of the system, the images of Figures 8, 9 and 10 illustrate the quality of images created by the scanner. Specifically, the image of the hot rod phantom in Figure 8 illustrates the ability of the system to differentiate 1mm-diameter cylinders separated by 2mm center-to-center. These very good results demonstrate the potential of this specialized scanner. A perhaps more tangible illustration of the imaging potential of the system is shown in the simple simulation of positron-emitting, radiotracer-avid lesions in adipose tissue. The high resolution of the tandem system reduces the effects of the partial volume effect, thus improving the contrast of small objects in background activity (Figure 9 and 10). The differences of the measured contrast ratios from the actual ratios is due mostly to the spreading of the counts from the spheres and overlaying areas of radiotracer-containing gelatin among numerous image planes. This spreading of counts is caused by the required use of limited angle tomography methods. This effect diminishes some of the gains in count recovery produced by reducing the partial volume effect with very good resolution.

Evaluation of the prototype tandem PET scanner produced promising results and revealed some potentially important limitations of this concept. Specifically, the scanner produces very good two-dimensional images, with significant blurring in the third dimension. Therefore, accurate three-dimensional localization of an area of tracer accumulation and of quantification of radiotracer concentration within the area is challenging. Furthermore, resolution of the tandem scanner is position dependent. To achieve maximum resolution and detection sensitivity, the object must be relatively close to the high-resolution detector. Unfortunately, FOV is smallest at these positions. Additionally, as demonstrated by the plots in Figure 3, the field-of-view of the system is strongly influenced by the size of the detectors and upon distance from the high-resolution detector. Angular sampling of the FOV is somewhat limited, necessitating the use of limited angle reconstruction methods, which produces smearing of counts in the z-dimension. Consequently, detection of small objects can be hindered, as demonstrated by the imaging of the small

spheres in a block of gelatin. Large target-to-background radiotracer ratios (at least 20:1) were necessary to detect the smallest spheres. Hence, these types of systems have a limited number of well-defined potential applications. Specifically, applications that allow the high-resolution detector to get very close to the object of interest and, ideally, that have minimal radiotracer-avid tissue overlaying the target imaging area.

In spite of the limitations identified in this investigation, a tandem PET system potentially has some important applications. For example, the very compact nature of the scanner's high-resolution element lends itself well to incorporation into an endorectal probe appropriate for imaging of the prostate. Clearly, some advances in radiotracer development are necessary to make this application an effective diagnostic procedure. Another potential application is the construction of a compact small animal imaging system, where the animal could be placed close to the high-resolution detector. Finally, tandem systems can be used similar to the way optical magnifying glasses are used. Specifically, they could be employed as specialized devices to magnify the spatial distribution of radiotracer uptake in a localized region that can be placed close to the high-resolution component of the scanner.

V. CONCLUSION

In conclusion, we have constructed a unique, high resolution PET system. Testing of the system revealed some limitations in its capabilities (relatively low detection sensitivity and small FOV), but also demonstrated its potential utility in specialized applications. Work is underway to address some of these deficiencies, and perhaps expand the choice of potential applications by increasing the detection sensitivity and FOV of system.

REFERENCES

- [1] R. Prasad, O. Ratib O and H. Zaidi, "NEMA NU-04-based performance characteristics of the LabPET-8 small animal PET scanner," *Phys. Med. Biol.*, vol. 56, pp. 6649-6664, 2011.
- [2] E.P Visser, J.A. Disselhorst, M.G.J.T.B. van Lier, P. Laverman, G.M. de Jong, E. W.J. Oyen and O.C. Boerman, "Characterization and optimization of image quality as a function of reconstruction algorithms and parameter settings in a Siemens Inveon small-animal PET scanner using the NEMA NU 4-2008 standards," *Nucl. Instr. Meth. Phys. Res. Sect. A*, vol. 629, pp. 357-367, 2011.
- [3] M. Cañadas, M. Embid, E. Lage, M. Desco, J.J. Vaquero and J.M. Pe'rez, "NEMA NU 4-2008 Performance measurements of two commercial small-animal PET scanners: ClearPET and rPET-1," *IEEE Trans. Nucl. Sci.*, vol. 58, pp. 58-65, 2011.
- [4] M.W. Jakoby, Y. Bercier, M. Conti, M.E. Casey, B. Bendriem and D.W. Townsend, "Physical and clinical performance of the mCT time-of-flight PET/CT scanner," *Phys. Med. Biol.* Vol 56, pp. 2375-2389, 2011.
- [5] M. Janeczek, H. Wu and Y-C Tai, "High resolution insert for clinical whole body PET scanners: design and optimization," *IEEE Nucl. Sci. Sympos. Conf. Rec.*, vol. 6, pp. 3849-3852, 2004.
- [6] Y-C Tai, W. Heyu, D. Pal and J.A. O'Sullivan, "Virtual-pinhole PET," *J. Nucl. Med.*, vol. 49, pp. 471-479, 2008.
- [7] A.J. Mathews, S. Komarov, M. Kume, W. Heyu, J.A. O'Sullivan and Y-C Tai, "Investigation of breast cancer detectability using PET insert with whole-body and zoom-in imaging capability," *8th IEEE Int. Sympos. Biomed. Imag. From Nano to Macro* pp. 1784-1787, 2011.
- [8] J. Qi, Y. Yang, J. Zhou, Y. Wu and S.R. Cherry, "Experimental assessment of resolution improvement of a zoom-in PET," *Phys. Med. Biol.*, vol. 56, pp. N165-N174, 2011.

- [9] R.R. Raylman, S. Majewski, M.F.Smith, J. Proffitt, W. Hammond, A. Srinivasan, J. McKission, V. Popov, A.G. Weisenberger, C.O Judy, B. Kross, S. Ramasubramanian, L.E. Banta, P.E. Kinahan and K. Champley, "The positron emission mammography/tomography breast imaging and biopsy system (PEM/PET): design, construction and phantom-based measurements," *Phys. Med. Biol.*, vol. 53, pp.637-653, 2008.
- [10] V. Popov, S. Majewski and A.G. Weisenberger AG, "Readout electronics for multianode photomultiplier tubes with pad matrix anode layout," *IEEE Nucl. Sci. Sympos. Conf. Rec.*, vol. 3, pp. 2156-2159, 2004.
- [11] C.D. Ramos, Y.E. Erdi, M. Goene, E. Reidel, H.W. Yeung, H.A. MacApinlac, R. Chisin and S.M. Larsen, "FDG-PET standardized uptake in normal anatomical structures using iterative reconstruction segmented attenuation correction and filtered back-projection," *Eur. J. Nucl. Med.*, vol. 39, pp. 1002-1006, 2001.